Abstract

Title of Dissertation: DESIGN OF AN OVERMODED KA-BAND SHEET-BEAM COUPLED-CAVITY TRAVELING-WAVE TUBE AMPLIFIER

Paul Benjamin Larsen, Doctor of Philosophy, 2011

Dissertation directed by: Professor Thomas M. Antonsen, Jr.
Department of Electrical Engineering

This thesis develops a qualified design for a sheet-beam coupled-cavity slow-wave structure for use in a high-power millimeter wave traveling wave tube amplifier. The main advance realized in the design is the roughly ten-fold increase in power gained by utilizing a sheet, rather than cylindrical, beam while at the same time employing mode-suppression techniques to suppress competing modes that are introduced by the sheet geometry. This design addresses considerations relevant to high-power tubes in general, as well as points specific to the design of a sheet-beam structure.

The coupled-cavity structure is designed with the following general characteristics: center frequency of 35 GHz with greater than a 10% bandwidth, and capabilities of 5 kW pulsed output power. The device operating parameters are as follows: a moderate gain of 18 dB, and an experimentally demonstrated sheet electron beam with 3.5 A, 19.5 kV, and 0.3 mm x 4.0 mm beam cross-section. The final design goal has been to limit the interaction length as much as possible to reduce magnet weight and complications.

A final design structure is proposed, which produces in excess of 5 kW peak power in simulation with safeguards from instabilities. The structure geometry is based on a novel design for a sheet-beam coupled-cavity slow-wave structure that has been characterized through various analyses, simulations, and experiments. This thesis outlines and details the various techniques used to probe the structure and thus form a full characterization of the structure and proposed amplifier device.

The concept espoused by much of this work is to adapt the analyses from cylindrical beam devices for the sheet-beam geometry. Then we make comparisons between the new sheet-beam structure and conventional devices. From these comparisons we draw conclusions on the operation of sheet-beam amplifiers and make design choices accordingly. The final design is validated with fully three-dimensional particle simulations and predicts stable amplification across the range of operation.

DESIGN OF AN OVERMODED KA-BAND SHEET-BEAM COUPLED-CAVITY TRAVELING-WAVE TUBE AMPLIFIER

by

Paul Benjamin Larsen

Dissertation submitted to the Faculty of the Graduate School of the
University of Maryland, College Park in partial fulfillment
of the requirements for the degree of
Doctor of Philosophy
2011

Advisory Committee:

Professor Thomas M. Antonsen, Jr, Chair
Dr. David K. Abe
Professor Victor L. Granatstein
Professor Adil B. Hassam
Professor Howard M. Milchberg

Acknowledgements

I would like to thank the following people for their assistance throughout my research at the University of Maryland and the Naval Research Laboratory. I would start by gratefully acknowledging the guidance of Professor Antonsen through all research and academic matters. I would also acknowledge the guidance of Dr. Abe at the NRL. Without these two men, this thesis would not be possible, and my training as an engineer would be incomplete.

Furthermore, I would like to thank everyone in the NRL Vacuum Electronics Branch for their collective patience, guidance, understanding, and endless assistance. Thank you: David Abe, Spence Albright, Nelson Blankenship, Jeff Calame, David Chernin, Igor Chernyavskiy, Simon Cooke, Morag Garven, Jeremy Hanna, Kevin Jensen, Colin Joye, Baruch Levush, Jim McDonald, Bob Myers, Yolanda Neal, Khanh Nguyen, Carolyn Parker, John Pasour, Dean Pershing, Jonathon Shaw, George Stantchev, Alexander Vlasov, Frank Wood, and Joan Yater.

Profound thanks go to Lars Ludeking, John Petillo, Alex Burke, John DeFord, and Ben Held for assistance with their respective simulation tools.

I also gratefully acknowledge Jim Legarra and Ed Wright for insightful technical discussions. Their wisdom and advice have helped surmount several serious obstacles in this project.

This work was supported by the U.S. Office of Naval Research and was conducted through the Student Temporary Employment Program (STEP) at the NRL.

Table of Contents

List of Figures

List of Tables

Chapter 1: Introduction

Traveling wave tube (TWT) amplifiers (TWTAs) are microwave power amplifiers that convert the energy of a DC electron beam into an amplified microwave signal. These amplifiers are used for many applications from communications, radar, and microwave testing in commercial, military, medical, and academic applications that require high-frequency and high-power sources [1]. Modern microwave and millimeter wave applications are continuously pushing the limits of amplifier power, bandwidth, and operating frequency – for example, in communications applications this supports increasing demands for faster data rates, multiple channels, and link closure under all types of weather conditions.

Traveling wave tube amplifiers are a type of microwave vacuum electronic device in which the electron beam continuously interacts with a traveling electromagnetic wave supported by a slow-wave structure to create a broadband frequency response. A slow-wave structure (SWS) is a periodic guiding structure that supports the transmission of electromagnetic power such that the velocity of power propagation is much smaller than the speed of light. The two most common types of SWS in microwave and millimeter wave TWTAs are helix and coupled-cavity structures. Helix amplifiers provide very broadband frequency response, but at higher power and frequencies they face many issues of thermal management related to the delicate helix support rod configuration [2]. Coupled-cavity structures have been shown to strike a good balance between high power and bandwidth.

In order to increase the microwave power produced by the amplifier we must either increase the power of the DC electron beam, or increase the efficiency of the extraction of that beam power. Further increases in the efficiency of power extraction in round-beam devices are limited by space charge effects that de-bunch the beam. There is an implied limit to the beam voltage due to the increase in power-supply size and hazards with increased voltage – a reasonably achievable voltage limit for a compact system is 20 kV. Increased current in cylindrical beams exacerbates the space-charge de-bunching effects, and becomes increasingly difficult for increasing frequencies at a fixed voltage. To circumvent these limitations, devices based on spatially distributed electron beams are now under consideration [3]. An electron beam with a rectangular cross section (“sheet beam”), which increases the beam power by distributing the beam current over an increased area, is one such topology.

In this thesis, we develop a qualified design for a sheet-beam coupled-cavity slow-wave structure for use in a high-power millimeter wave TWTA. The main advance realized in the design is the roughly ten-fold increase in power gained by utilizing a sheet, rather than cylindrical, beam while at the same time employing mode-suppression techniques to suppress competing modes that are introduced by the sheet geometry. The original contributions of the research presented in this thesis are as follows:

- Simulated and experimental characterization of a sheet-beam coupled-cavity slow-wave structure for use in a sheet-beam TWTA.
- Development of a broadband waveguide coupler for well-matched power transfer through the proposed sheet-beam structure.
- Comparisons of simulated gain estimates for the sheet-beam structure.
- Development of stability analyses to account for the multiplicity of modes that might interact with the electron beam within the sheet-beam structure.
- Modification of slow-wave structure parameters and application of mode-suppression techniques to achieve increased power and suppress competing modes.

In this thesis, we develop and analyze a sheet beam coupled-cavity slow-wave structure capable of moderate bandwidth and moderate gain and with an increase in power from a compact Ka-band TWT. The present chapter provides an outline of the state of the art in TWTAs and current research in the development of high-power millimeter wave amplifiers, as well as an outline of the proposed device. Chapter 2 investigates the sheet-beam slow-wave structure and the various simulation and experimental methods used to probe the structure and the effects of geometric variations or errors. Chapter 3 outlines several gain analyses developed for sheet-beam devices and provides comparisons of the results. Chapter 4 discusses the methods of analyzing undesired interactions of the sheet electron beam with the structure, and methods of suppressing these interactions and mitigating deleterious instabilities. Chapter 5 provides the final design and the results of various supporting simulations.

1a) State of the Art Coupled-Cavity Devices

Coupled-cavity devices consist of a slow-wave structure of periodic electromagnetic cavities that are each coupled to adjacent cavities via some coupling mechanism, and an electron beam that propagates down a beam tunnel axially through the stack of cavities, interacting with the

electromagnetic fields in the cavities at discrete gaps in the beam tunnel [4] [5]. The cavities and coupling mechanism are tuned to provide a moderately broadband frequency response and strong interaction with the electron beam. Conventionally, the electron beam is cylindrical with a round beam-tunnel, although the structure can be a complicated three-dimensional geometry. Coupled-cavity devices are generally able to handle the thermal requirements of high-power operation because their solid metal construction allows for good thermal conduction and somewhat less delicate assemblies (compared to helix devices, for example).

For example, the current state-of-the-art in round beam coupled-cavity TWT performance in Ka-band is about 500 W over 500 MHz instantaneous bandwidth with 40 dB gain [6]. Other recent publications have presented coupled cavity TWTs at 30 GHz, 500 W CW, 2 GHz bandwidth (CPI) and at 35 GHz, 1 kW peak, 500 W CW, 3 GHz bandwidth [7]. A plot of compiled data of current state of the art peak power broadband Ka-band amplifiers (both helix and coupled-cavity tubes) is provided in Figure 1.1. The listed output powers are shown in dashed lines for helix and coupled-cavity tubes (from lowest to highest: L-3 Communications' millimeter wave power module [8], Thales helix TWTA [9], L-3 Communications' helix TWTAs [10] [11], and CPI's coupled-cavity TWTA [6]). The blue curve at the top represents data that are the results of particle simulations of the proposed coupled-cavity structure (presented in Chapter 5), which represents a roughly ten-fold increase in power over the listed powers of cylindrical devices.

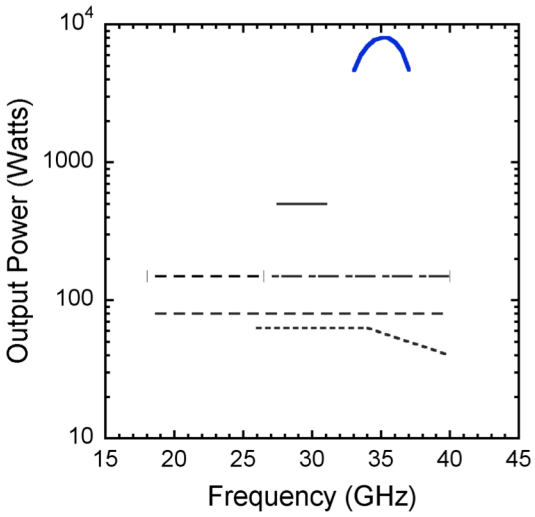

Figure 1.1: Attainable peak power from current state of the art helix and coupled-cavity tubes in Ka-band – rated output power (dashed lines), and proposed sheet-beam simulations (solid blue line).

The current state of the art devices have met a limit of the achievable output power. We have already seen that the total microwave power is limited by the product of the beam current and beam voltage. Since our desire is to keep the voltage reasonably low, the total beam current must scale in proportion to the total microwave power. However, the current density is at the limit of modern focusing and cathode technology. Thermionic cathode electron guns used in

these devices can produce a current density limited by the lifetime of the cathode (the common M-type cathode can achieve 5-15 A/cm^2 with long lifetime [12]), and the area convergence of the beam is limited by design complications even in round-beam guns. Furthermore, the magnetic focusing of an increased current density is increasingly difficult, especially for periodic magnetic focusing at low voltages. Combining these difficulties, there is currently a reasonable limit to the transportable current density of some several hundreds of amperes per square centimeter without overly loading the cathode and shortening the expected lifetime of the amplifier. Furthermore, the electron beam diameter is set by the frequency operating point, where the frequency determines the effectual radius of the beam tunnel. For a cylindrical-beam device this leads to decreasing beam currents and available power at increasing frequencies. In Ka-Band at the upper voltage limit of 20 kV, the most current you could reasonably expect in a cylindrical beam might be 1 A with a current density of roughly 500 A/cm^2, implying a 500 μm diameter, which are all reasonable numbers for a high-power coupled-cavity device such as that described in [6].

1b) Spatially-Distributed Electron Beam Technology

To overcome the power limitations of a conventional round-beam structure several different spatially-distributed electron beam technologies have been studied that allow increased current for a fixed voltage. Spatially-distributed beams can be realized by multiple, parallel round beams or by a transversely-stretched beam, where one of the transverse dimensions is stretched into either a rectangular (or elliptical) cross-section beam. Each of these technologies requires a specific interaction structure adapted to the required beam tunnel, providing maximal and uniform interaction. Some of these structures operate in the lowest mode (fundamental mode), while others operate in a higher-order mode – all of these structures have complications in dispersion and fields which must be addressed.

Spatially-distributed electron beam devices have a number of advantages, including [1]:

- Lower voltages are possible at a given output power due to the increased total beam current – low voltage operation is critical for compact sources and their accompanying power-supplies.

- The increased beam current to voltage ratio (increased beam impedance) results in a wider bandwidth, because the beam-wave interaction is stronger across the full bandwidth of the structure (see the discussion in the chapters on gain and stability).
- Higher efficiency results from using lower perveance beamlets due to decreased space-charge de-bunching in the beam.
- The increased transverse dimensions required for both the beam-tunnel(s) and the slow-wave structure suggest that a larger surface area interacts with both the beam and RF currents and possibly allows for more favorable distributions of both the beam and circuit losses.
- Reduced magnetic focusing field required with lower current density and therefore reduced weight.

Multiple electron beams have been investigated in several different configurations, and in both klystron and traveling-wave amplifiers [13]. Multiple beam klystrons have been manufactured in Russia [14], France [15], the People's Republic of China [16], and the USA [17]. Multiple beams have been studied in traveling-wave amplifiers in a similar, klystron-like configuration with parallel beams interacting with one structure [18] (Figure 1.2). This configuration of parallel beams interacting with a single structure is similar to the sheet-beam case, but can also use a higher-order mode field distribution in order to locate the field maxima near the individual beams (for example in Figure 1.2a, if the azimuthal order were three, then each outer beam-tunnel could be at a field maximum, although the central beam-tunnel would necessarily be at a null in that example). There are serious complications with multiple-beam devices in traveling-wave structures at millimeter-wave frequencies that are discussed subsequently in the sheet-beam advantages.

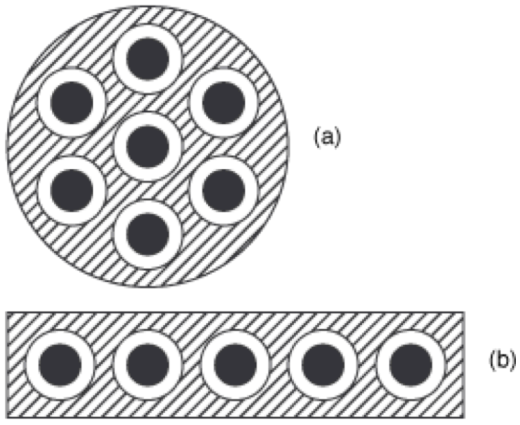

Figure 1.2: Two different configurations of multiple cylindrical beams passing through multiple separate beam tunnels. These beams generally interact with a single structure. (a) A clustered set of beams. (b) A linear array of beams.

Multiple beams have also been configured as parallel beams interacting with multiple, power-combined structures [19], and as series structures powered by parallel beams [20]

(Figure 1.3). However, with power-combined parallel structures there are concerns of the effectiveness of the broadband match of the power-combining input and output sections. The series structure configuration does not increase the effective beam-power inherently because the final section only sees the final beam, but it does promise increased efficiency of extracting power from the electron beams due to improved bunching of the beams.

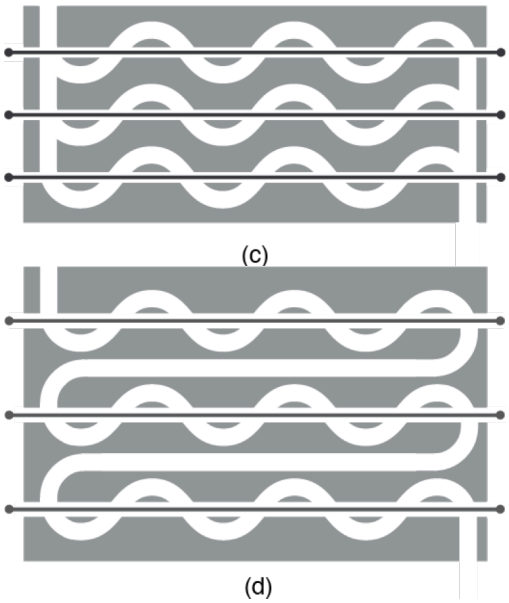

Figure 1.3: Two different configurations of parallel cylindrical beams passing through multiple separate structures. (c) Power splitting/ combining design. (d) Series design.

Hollow electron beams are a form of sheet-beam that has been curved into a hollow circle allowing increased current to be transported close to the walls of the interaction structure. Hollow beams have been utilized in klystron amplifiers to produce high-perveance, high-efficiency, high-power devices [21] [22]. However, since the fundamental mode of a traveling-wave structure has an increased backward-wave interaction for larger beam radius, an alternative mode or geometry must be utilized for an amplifying traveling-wave structure, and this configuration has not been pursued for TWT amplifiers. Hollow beams are used in backward-wave oscillators to increase their beam-wave interaction [2].

Sheet beam technology is an alternative distributed beam concept that has been discussed by various groups, but not until recently has it been seriously investigated. A sheet electron beam is an electron beam that is elongated along one transverse dimension creating a rectangular (or elliptical, or otherwise elongated) current density distribution (Figure 1.4). As a comparison to a conventional round-beam structure, we see that the beam-tunnel

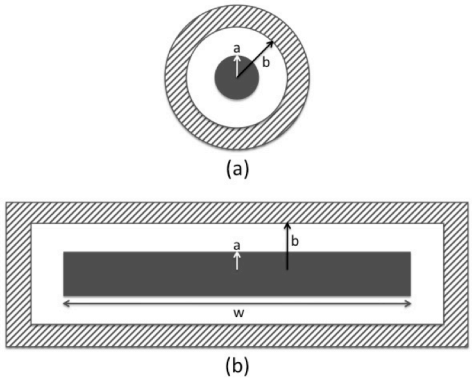

Figure 1.4: Sheet beam pictured as a distributed cylindrical beam with roughly equivalent radii/heights. (a) Cylindrical beam within a cylindrical beam-tunnel. (b) Rectangular sheet beam within a rectangular beam-tunnel.

radius, b, is restricted in size (inversely to the frequency) in order to keep the beam-wave interaction large; but in the sheet-beam case, the beam-tunnel height is only restricted in one dimension, while the other dimension can be elongated many times. The electron beam height, a, is usually restricted to some fraction of the beam-tunnel height to minimize interception and interaction with undesired modes, and with a reasonably achievable current density (due to modern limits in cathode and focusing technology), the total transportable current is limited at each frequency range of interest. The width of the sheet-beam, w, is often expressed as an N times increase of the total beam height (*i.e.* w = N*2a).

The main advantage of the sheet beam technology over single-beam technology is the increased beam current allowed with comparable current density, generated by the elongated beam dimension. Two possible advantages of sheet beams over multiple beams are: 1) reduced multiplicity of electron gun components, and 2) a more compact total cross-section of the beam area suggests that the transverse dimension of the structure can remain smaller and the mode-density will be minimal. These reasons are compounded by the manufacturing capabilities (and expenses) available at millimeter wave frequencies, and were a determining factor in choosing a sheet-beam configuration over multiple beams.

Inevitably, several complications arise from the elongated structure geometry required to support the sheet electron beam. The first complication due to an elongated structure with an elongated beam tunnel is in creating a uniform electric field with which the electron beam may interact. The second complication due to an elongated structure is the increased mode-density of the structure created by the elongated dimensions on the structure and beam tunnel. The third complication that has been an obstacle for operation of sheet-beam devices is the excitation of a transverse mode that is inherent to an elongated beam tunnel [23]. Further discouraging the use of sheet beams has been the problem of the diocotron instability, which leads to beam break-up and interception. Recently, there have been several technical advances in the creation and focusing of sheet electron beams [24] [25] [26] [27], which makes sheet-beam amplifier technology attainable. Finally, without modern 3-D modeling tools and the concurrent computational advances that make them possible on a design time-scale, the analysis of the three-dimensional beam-wave interactions would not be possible.

Sheet beams have also been discussed for use with grating structures [28] and orotrons [29]. These structures have elongated geometries that are appropriate for sheet electron beams, and

are especially interesting at high frequencies where the 2D structure geometries are amenable to lithographic construction techniques. However, these structures are not interesting for broadband applications, as they generally have poor bandwidth.

1c) Current Research and Challenges

Due to current technological advances in sheet-beam generation and transport, as well as three-dimensional simulation capabilities, sheet-beam technology is being investigated concurrently by several different groups. These research projects address various challenges and implications of sheet-beam technology in various microwave vacuum electronic devices with different beam, power, and frequency parameters. The following groups have worked on sheet-beam devices in some fashion as described.

SLAC – W-band Sheet-Beam Klystron: The group of scientists and engineers at the Stanford Linear Accelerator Center (SLAC) has developed, over the course of many years, a sheet-beam klystron amplifier at W-band (94 GHz) with narrow-bandwidth and 100 kW peak power, 2 kW average power (simulated results) [30] [31] [32] [33] [34]. The SLAC group is the most fully documented design of a sheet-beam device and has many similar goals and obstacles as those presented within this thesis, however, there are two main difference between the SLAC klystron and the present research: first, their device is a narrowband klystron, while this thesis investigates a broadband coupled-cavity device, and, second, their W-band klystron has a beam-voltage of 74 kV, while we utilize a modest 20 kV that is favorable for modulator cost/availability, and x-ray shielding. The SLAC device has been developed up to the point of experimentally testing a periodically permanent magnet focused sheet beam, and separately testing the RF-response of the klystron cavities at W-band. There has been an experimental test with an X-band sheet-beam klystron reported in [35].

LANL – W-band Grating Amplifier: A group of scientists and engineers at the Los Alamos National Laboratory (LANL) has developed a sheet-beam, and grating structure also at W-band (94 GHz) with moderate bandwidth response and possibly 480 kW of peak power (according to simulation) [36] [37] [38] [39] [40] [41]. The LANL group has documented their beam formation and transport results, which they have thoroughly simulated and experimented (although using non-conventional beam-shaping techniques in a bulky experiment chamber and a large 110 kV beam voltage). The grating structure has been developed to varying degrees in design and

experiment, with an intermediate design being most recently tested with a cylindrical beam exhibiting nominal gain, but also self-excited oscillations.

NRL – W-band Extended Interaction Klystron, Multiple-Beam Klystron, Transverse TWT Amplifiers: The entire team of scientists and engineers at the Naval Research Laboratory's (NRL) Vacuum Electronics Branch is interested in distributed beam vacuum electronic devices and their advantages [42]. The three mentioned topics are particularly interesting and relevant to sheet-beam development. The W-band Sheet-Beam Extended Interaction Klystron (WSBEIK) is a narrowband, high-power device that has been developed to the point of experimentally demonstrating beam-transmission and testing the RF response of the WSBEIK cavities [43] [44]. The WSBEIK device is very similar in stature to the device investigated in this thesis, as we intend to reuse the electron-gun and collector design in the present work. The Multiple-Beam Klystron (MBK) device is a moderate-bandwidth high-power amplifier at S-band (3.2GHz) [17] [45] [46] [47] [48] [49] [50]. This amplifier was the first distributed-beam amplifier built to completion starting from NRL designs, and the highly-documented development addressed many technical obstacles to distributed beam formation, transport, and interaction. Finally, Transverse TWT Amplifiers are being studied as an alternative technique of interacting and extracting RF power from an electron-beam (instead of the standard longitudinal interaction) [51] [52] [53] [54]. Transverse interactions were initially studied in cylindrical beams, but the elongated beam-tunnel shape of the sheet-beam structure allows for the adjustment of the dispersion in strongly transverse modes while also allowing for increased current as in longitudinal structures.

UC-Davis – Sheet Beam Offset Grating Structure: The researchers at the University of California – Davis (UCD) are investigating a broadband sheet-beam structure that is comprised of opposing grating structures with offset-alignment (teeth from one grating align with the gaps of the opposite grating and the electron beam is transported between the two gratings) [55] [56] [57] [58] [59] [60]. This configuration has an advantage of combining the lowest transverse and longitudinal modes due to the offset gratings (the fields in the fundamental mode are directed predominantly diagonally from tooth to tooth), yet the fields are very complicated in this simple geometry and not at all uniform in the wide dimension. Further, because this is a simple grating geometry the primary goal is to manufacture with lithographic techniques and operate at terahertz frequencies (220 GHz). This group is similarly developing a sheet-beam gun and

transport section, and also has developed a moderate bandwidth coupler. There have been scaled experiments on the novel RF structure, but there have been no beam experiments.

MIT – Elliptical Beam: A group from the Massachusetts Institute of Technology has been working on elliptical-beam guns and beam transport for various size beams (dimension and current density) [61] [62] [63] [64] [65]. There have been several experiments with successful focusing of a moderate-density electron-beam at reasonable voltages. There is no vacuum electronic amplifier associated with this research, yet their elliptical beam is similar in construction to a TWTA sheet-beam.

Several other groups have investigated distributed beam structures and the design of a corresponding amplifier. In addition to numerous examples of multiple-beam klystrons [13], there have been a couple efforts at sheet-beam klystron design [66] [67] [68] [69] [70] [71] [72] from S- to W-band. In the sub-millimeter range of traveling-wave structures, there have been efforts to micro-fabricate circuits that power combine through a splitter/combiner [19] [73]. Also traveling-wave structures have been implemented with multiple-beam coupled-cavity circuits [13] [18] – this is most pertinent because it has similar goals as the present research, but has only been applied at lower frequencies.

1d) Proposed Sheet Beam Device Design Concept

The proposed device is a sheet-beam coupled-cavity traveling-wave tube amplifier with increased current and, therefore, increased RF power capabilities. The center frequency of the operating band has been selected in the upper part of the Ka-Band at 35 GHz. This represents a region of the power-frequency parameter-space that can benefit from the advantages of a sheet-geometry, yet is feasible to manufacture using conventional milling technology. The goal of the project is to achieve 5 kW RF output power across a reasonable coupled-cavity bandwidth ($\Delta f/f_0$ ~ 20%). The gain of the device can be constrained modestly to simplify the design and reduce the risk of undesired oscillations. The design parameters are listed in Table 1-I for reference.

Design Frequency	35 GHz
Design Output Power	5 kW
Design Bandwidth	~7 GHz

Table 1-I: Overview design parameters for use in proposed device.

The structure we investigate for these purposes is a three-slot, doubly periodic, staggered-ladder coupled-cavity slow-wave structure developed

at the U.S. Naval Research Laboratory [74], [75]. A generic design for one cell of the structure is shown in Figure 1.5. It consists of two rectangular half cavities separated by a septum with a beam tunnel and three coupling slots. The adjacent cells are rotated 180° around the beam tunnel axis (which is the same as being mirrored the long way) so that the beam tunnel stays in the same position and Slot 2 of the next cell is on the right side of the beam tunnel (looking down along the direction of electron travel). For the remainder of the thesis, the *z*-axis is in the direction of propagation (the axial direction), the *x*-axis is in the wide dimension of the structure (horizontal), and the *y*-axis is in the short dimension of the structure (vertical).

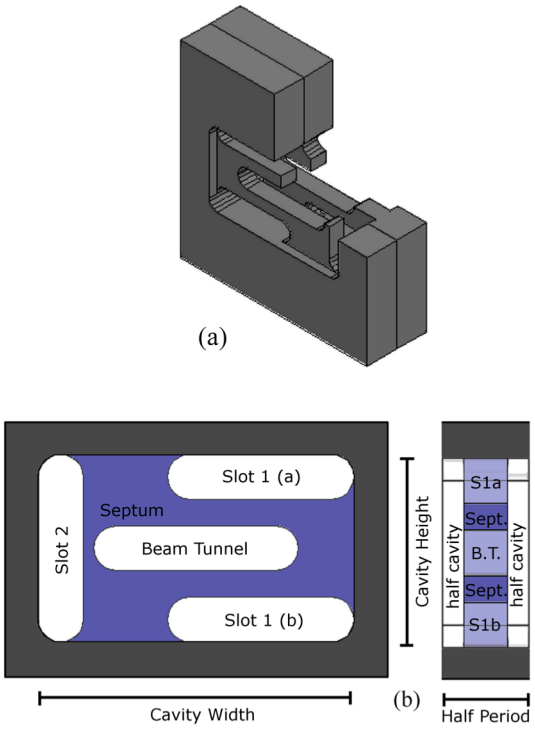

Figure 1.5: (a) Cut-away, isometric view of a 3D model of a full-period (created by stacking two, rotated unit cells). (b) Generic design for one cell (half-period) of the three-slot SWS.

Throughout the rest of this document there will be several designs based off this generic configuration. These will be discussed to present the various trials and modifications utilized in order to address the pertinent issue at hand and to realize the best structure. The specific structure under discussion will be introduced and referred to by number so that the various results can be matched to the exact structure measurements.

A key enabling technology for this sheet-beam device is the recent development of a thermionic sheet-beam electron gun with permanent magnet focusing, as described in [25]. These beam source and transport sections have been experimentally tested with 98% transmission over a distance of 1.9 cm [26]. Although originally designed for use in a W-band extended interaction klystron (EIK), the same beam can be used in a Ka-band traveling-wave device. Table 1-II summarizes the sheet beam

Beam Current	3.5 amps
Beam Voltage	19.5 kV
Beam Width	4 mm
Beam Height	0.3 mm

Table 1-II: Electron beam parameters for use in proposed structure.

parameters.

The total DC beam power for this device is 68 kW, so for a circuit efficiency of 7.5% there would be more than 5 kW of RF power output – this would represent an order of magnitude increase over the state of the art at Ka-band, and this peak power output is the main goal of the experiment. The sheet-beam itself creates this power increase, as conventional traveling-wave circuits can have efficiencies between 10-15%. With further enhancements the efficiency could be increased in the sheet-beam device as well. The total bandwidth for the driven structure is desired to be as large as possible. The slow-wave structure geometry is adjusted for optimal bandwidth and interaction strength while maintaining stability – based on the design and simulations described in Chapter 5, the predicted 3-dB bandwidth is 6.5 GHz (*i.e.* 18.6%), which is commensurate with medium-power conventional coupled-cavity structures.

The proposed design consists of a roughly 5 cm length of slow-wave structure with waveguide couplers on each end and has 18 dB of gain as predicted by 3D particle-in-cell simulations. There are several techniques implemented to mitigate instabilities, and numerous simulations to confirm the stability of the structure under experimental drive conditions. The remainder of this thesis will outline and detail the various techniques used to probe the structure and thus form a full characterization of the structure and proposed device.

Chapter 2: Sheet-Beam Slow-Wave Structure Characterization

The slow-wave structure utilized in the design of the sheet beam device is a novel structure with complicated modes, and needs to be fully characterized before it can successfully be integrated with an electron beam. This structure was introduced in Section 1d, and pictured there in Figure 1.5. The structure will be thoroughly characterized here for the purpose of understanding the geometric dependence of the first several modes in order to achieve the desired frequency and interaction characteristics detailed in Chapter 1.

In this chapter we investigate a test structure with frequency centered at 30 GHz (not the final device requirements) through simulation and experiment. The effects of varying parameters are investigated for the dual purposes of achieving the required design and for studying the sensitivity of the device to manufacturing errors. We discuss the issue of creating a well-matched broadband waveguide coupler in order to transmit RF power through the slow-wave structure circuit. Finally, we examine realistic fabrication tolerances and their implications.

2a) Slow-Wave Structure Analysis and Dispersion

In order to characterize the response of the structure we use numerical three-dimensional finite-element electromagnetic simulations of the slow-wave structure geometry, obtaining frequency and field data for a given slow-wave structure. The numerical simulation of the electromagnetic fields of non-resonant, traveling-wave electromagnetic structures has been accomplished for many structures both past and present [76] [77] [78] [79] [80] [75]. The present structure has several symmetries that can be employed, and are investigated in detail in Appendix II.

3D electromagnetic simulations of a single structure period were performed for a wide variety of parameters. These simulations were performed using a commercial eigenmode solver with periodic boundaries (master/slave boundaries) for phase advances between 0 and 180 degrees. We used both Ansoft's HFSS [81] and AWR Corp.'s Analyst [82] to perform the eigenmode simulations and found good agreement between the two codes.

An example of the simulated dispersive characteristics of a structure with parameters listed in Table 2-I are presented in Figure 2.1, where frequency is plotted versus phase advance per cell. The structure with parameters in Table 2-I was intended as a test structure and will be the

structure studied in depth in this chapter: however, it does not meet the requirements of the proposed design. Please note that this structure is centered around 30 GHz, and with a synchronous beam voltage close to 13.5 kV. The interception of the beam line with the symmetric mode near 3π/2 indicates operation in the first forward space harmonic as in the staggered-slot coupled-cavity slow-wave structure of [4].

SWS Parameter	[in]	[mm]
period	0.0625	1.588
slot 1 & 2 width	0.035	0.889
slot 1 length	0.154	3.912
slot 2 length	0.151	3.835
cavity width	0.272	6.909
cavity height	0.151	3.835
beam tunnel		
width	0.182	4.623
height	0.0375	0.953

Table 2-I: Parameters for the simulated slow-wave structure.

The first thing to notice in the dispersion diagram is the presence of several modes within the frequency range of interest (in a conventional coupled-cavity structure there are only two modes – a cavity mode and a slot mode). The solid, bold curves have nearly the conventional field structures of the cavity and slot modes (with some interaction near the stopband gap at ~1.75π). We refer to these as "symmetric" modes due to the approximate symmetry of the axial electric field in the short-transverse dimension, centered within the beam tunnel. One main difference of this three-slot coupled-cavity structure from a conventional one- or two-slot structure is that here the slot mode and cavity mode couple in such a way as to form an avoided crossing (*i.e.* these are nonorthogonal modes and the two modes mix, forming a band gap) [83]. The thin, gray curves represent an unconventional mode supported by the wide beam tunnel with an electric field that is predominantly transverse (in the short dimension) to the axis of the structure. We refer to these as "antisymmetric" modes due to the antisymmetric nature of the axial electric field in the short-transverse dimension, centered within the beam tunnel. As an

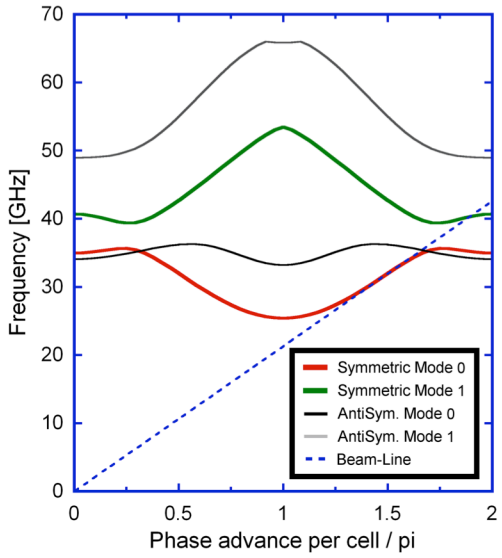

Figure 2.1: Dispersion diagram (frequency vs. phase) with respect to one cavity-period.

example, a beam line at 13.3 kV is drawn in the diagram that intersects the lowest symmetric mode near 1.5π. As seen in Figure 2.1, there is a backward wave intersection with the antisymmetric mode as well as intersections with the first and second symmetric modes near band edges at 1.75π and 2π, respectively. These intersections could lead to parasitic oscillations and will be discussed in Sections 2c, and more fully in Chapter 4.

To conceptualize the dispersive behavior of the structure we can determine the resonance frequencies associated with different parts of the structure using simple analytical models similar to those of Curnow [84]; Carter and Shunkang [85]; and Christie, Kumar, and Balakrishnan [86]. Using the dimensions in Table 2-I and the dispersion diagram of Figure 2.1, we find that the resonance for Slot 1 is approximately $f_{s1} \approx c/\left(2L_{slot1}\right) = 38.3\text{GHz}$, and the resonance for the Slot 2 is $f_{s2} \approx c/\left(2L_{slot2}\right) = 39.1\text{GHz}$. The cavity resonance is $f_{cav} \approx 40.8\text{GHz}$ as evaluated from a simple HFSS eigenmode simulation of a single cavity where the coupling slots are terminated with conducting shorts. The resonance for the beam tunnel is $f_{BT} \approx c/\left(2L_{BT}\right) = 32.4\text{GHz}$. These resonances can be seen to correspond to the following points on the dispersion curve. The resonant frequency of the cavity lies at the 2π point of the second symmetric mode. The lowest slot resonance lies somewhere near the 2π point of the first symmetric mode. The two different slot frequencies are related to the band gap at the avoided crossing (near 1.75π). The slot dimensions (height and length) can be tuned to eliminate the band gap near 1.75π. The beam-tunnel resonance affects the frequency range of the first antisymmetric mode.

2b) Effects of Structure Parameters on Dispersion

Effect of varying beam-tunnel height to width ratio: In our basic structure design, the nominal beam-tunnel width to height ratio is 4.8:1. To study the effect on the frequency behavior of the structure, we reduced the tunnel width to height ratios to 4.0:1, 3.0:1, and 2.0:1. For each ratio, the dispersion curves for the two lowest-order symmetric modes and first antisymmetric mode are plotted in Figure 2.2. In Table 2-II, we compare analytical results, similar to those calculated earlier, to the simulated results (the grayed columns in the table). The first column of data is the analytical resonance frequency for the beam tunnel determined by the length, which is compared to the 2π-point frequency of the antisymmetric mode in the second column. The third column contains data representing the first resonant frequency of a simple eigenmode

simulation of one cavity where the slots are terminated in conducting shorts (the cavity mode), which is compared with the 2π frequency of the cavity mode in the fourth column. The fifth column is the second resonant frequency of the same simple eigenmode cavity simulation, which is compared with the π frequency of the second symmetric mode in the sixth column.

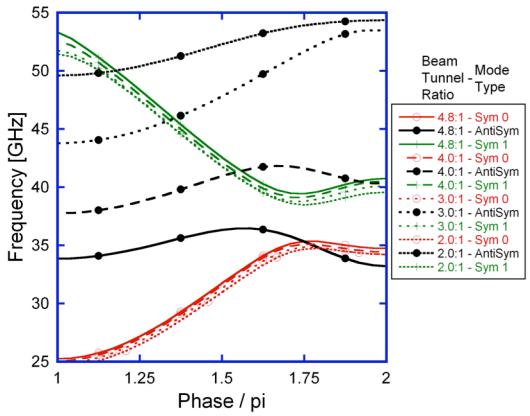

Figure 2.2: Dispersion plots for varying beam-tunnel width. The red, open-circle and green, crossed curves represent the first two symmetric modes, and the black, filled-circle curves represent the antisymmetric mode. The dash of the lines corresponds to the beam-tunnel ratio as indicated.

As seen in the last four columns of Table 2-II, the resonant frequencies of the symmetric modes change by only a modest amount (at most 3% at the 2π cavity frequency). In contrast, the antisymmetric mode frequencies (column two in Table 2-II) increase by 64%. Returning to the beam-tunnel resonance calculation, we find that the resonance frequency varies inversely to the length, with values reported in Table 2-II. These resonance frequency values correlate well with the 2π-frequency of the antisymmetric curve over much of the range of the beam-tunnel ratios without any attempt at accounting for fringing fields. It is evident that in the nominal case the antisymmetric mode has a low frequency, comparable to that of the symmetric mode, due to the wide beam tunnel, and it will be present in the design of any sheet-beam SWS. It is also clear that small adjustments of the beam-tunnel width (when possible) can control the interaction with the antisymmetric mode without greatly disturbing the symmetric mode.

Beam Tunnel Ratio	f_{BT} **analytical** [GHz]	$f_{2\pi\text{-antisym.}}$ **simulation** [GHz]	f_{cav} **cav.-simul.** [GHz]	$f_{2\pi\text{-cav-sym.}}$ **simulation** [GHz]	f_{cav} **cav.-simul.** [GHz]	$f_{\pi\text{-sym.}}$ **simulation** [GHz]
4.8:1	32.45	33.22	40.61	40.77	53.32	53.28
4.0:1	38.94	40.28	40.41	40.54	52.52	52.50
3.0:1	51.91	53.46	40.00	40.11	51.66	51.73
2.0:1	77.87	54.35	39.47	39.56	51.23	51.42

Table 2-II: The effects on resonance frequencies of changing beam-tunnel width. The data in the grayed cells are taken from the dispersion plots in Figure 2.2.

Effect of varying cavity height to width ratios: The next set of simulations is intended to approach the familiar limit of a conventional round beam coupled-cavity SWS. While keeping the beam tunnel aspect ratio a constant 1:1 (i.e., a round beam tunnel), we varied the cavity width to height ratios by 1.8:1, 1.5:1 and 1.25:1, while simultaneously decreasing the length of Slot 1 (see Figure 1.5). The results are provided in Figure 2.3 and Table 2-III. The columns in this table compare the analytic slot resonance frequency with the simulated 2π slot-mode frequency (columns 3 and 4, respectively), and the fundamental (f_{cav}) cavity mode with the simulated 2π cavity-mode frequency (columns 5 and 6, respectively).

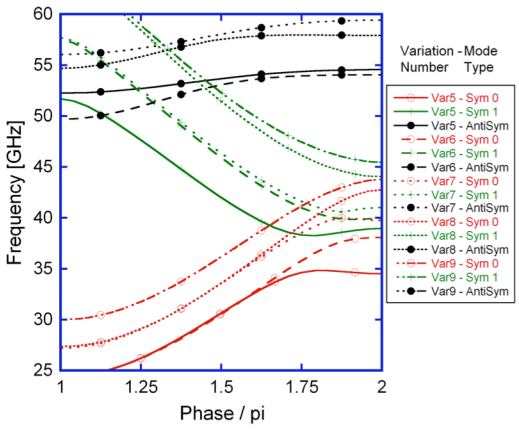

Figure 2.3: Dispersion plots for varying cavity width and normalized slot length – see Table 2-III for variation details. The dash of the line corresponds to the variation number as indicated.

Looking at the fundamental mode (modes marked with open-circles in Figure 2.3), we notice that as the cavity width decreases the dispersion curve loses its unconventional band-edge at ~1.8π and has positive group velocity up to 2π. The unconventional band-edge shape reappears as the slot length is further reduced in variation 7 (it appears at a slightly larger phase ~1.88π). It can be inferred that the cavity mode and slot mode resonance (frequencies at 2π phase advance) are switching the curve with which they are associated. This is made evident in field profiles (not pictured), where the cavity mode and slot mode have distinct field profiles, although there is mode mixing near the avoided crossing.

Variation #	**Cavity Ratio**	**Normalized Slot Length**	f_{slot1} **analytic** [GHz]	$f_{2\pi\text{-}slot}$ **simulation** [GHz]	f_{cav} **cav.-simul.** [GHz]	$f_{2\pi\text{-}cav}$ **simulation** [GHz]
5	1.8	1.0	38.32	34.52	38.76	38.96
6	1.5	1.0	38.32	39.06	39.76	39.96
7	1.5	0.855	44.81	39.74	40.79	41.02
8	1.25	0.855	44.81	44.04	42.49	42.75
9	1.25	0.732	52.35	45.46	43.49	43.76

Table 2-III: The effects on resonance frequencies of changing cavity width and slot length. The data in the grayed cells are found in the dispersion plots in Figure 2.3.

2c) Field Profiles and Impedances

In general, the field profiles can be broken into the same two categories as the dispersive characteristics: symmetric and antisymmetric. The symmetric modes have an electric field component along the axis of the structure, and the axial electric field is symmetric with respect to the short transverse dimension. The antisymmetric modes have a predominantly transverse field along the axis, and the axial electric field is antisymmetric (switches direction) with respect to the short transverse dimension.

The symmetric field is plotted on the cavity midplane in Figure 2.4 a,b for the same set of parameters from Table 2-I, and for a phase advance near 1.5π for the fundamental mode (lowest frequency mode). The characteristics of this mode (besides those already discussed), are very much like a cavity mode with the electric field concentrating between the opposite walls around the beam tunnel. Furthermore, the field within the beam tunnel is reasonably uniform across the wide dimension, and it varies much like the hyperbolic cosine in the short dimension. Finally, because there are no ferrules and the beam tunnel is elongated there is leakage of the fields through the beam tunnel (where the fields diminish in intensity, but do not disappear completely), although the fields mostly couple through the slots.

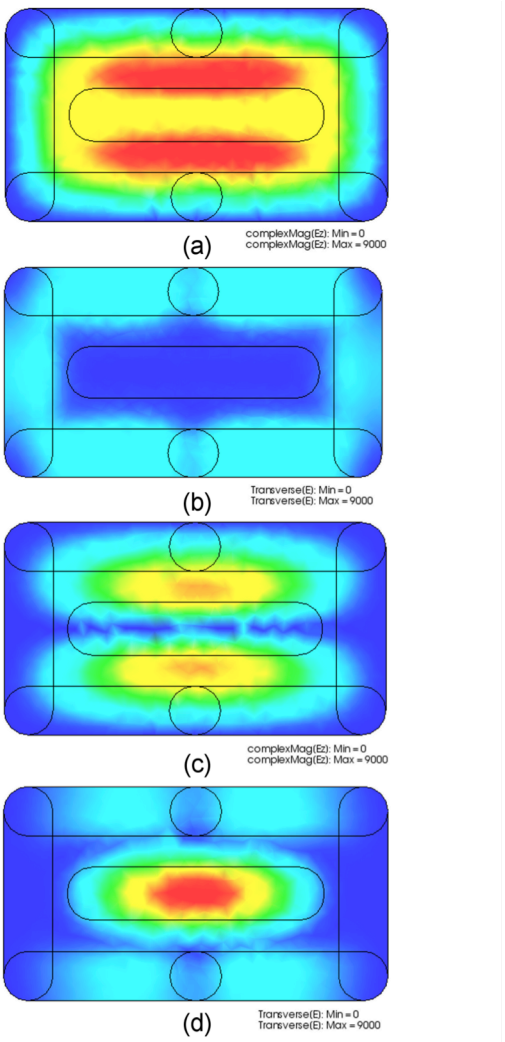

Figure 2.4: Field components (complex magnitude) for symmetric mode – longitudinal (a), transverse (b) and antisymmetric mode – longitudinal (c), transverse (d). The fields are plotted at the midplane of the cavity at a phase advance of 1.46π (symmetric) and 1.58π (antisymmetric).

The antisymmetric field is plotted on the cavity midplane in Figure 2.4 c,d for the same set of parameters and for a phase advance near 1.5π. The characteristics of this mode are that the fields are transverse and localized within the beam tunnel. The transverse fields are roughly

uniform in the short transverse dimension within the beam tunnel and have peak intensity near the center of the long transverse dimension (varying as the half-wavelength of a cosine function, as if the beam tunnel were a waveguide). In addition to the transverse fields in the beam tunnel there is a small longitudinal component that varies much like the hyperbolic sine in the short dimension (zero intensity on axis), and is similarly non-uniform in the wide dimension.

When one looks at the real and imaginary parts of the field (as opposed to just the complex magnitude, which is plotted in Figure 2.4), for some structural parameters the field appears with a phase shift across the long dimension of the structure. Specifically, for the case under study, for increasing phase advance (near 2π) in the fundamental mode, the real field is a maximum at one end of the beam tunnel, whereas the imaginary field is maximum at the other end of the beam tunnel. This will effectively cause a small tilt to the beam bunching, but will not significantly affect the gain. The biggest effect that the phase variation will have is on coupling into the structure, and this will be accounted for when designing the optimal coupler for the given structure.

The interaction impedance of a slow-wave structure is a measure of the electric field affecting an electron beam in the beam tunnel per unit power flowing through the structure. There are several definitions of interaction impedance and we will consider two of them. Both of these impedances are determined using the simulated field solutions and both are a function of phase advance.

First, we find what is commonly called the Pierce Impedance [5]. This is defined as:

$$Z_{Pierce} = \left|E_{z0}\right|^2 \Big/ \left(2k_z{}^2 P\right), \tag{2.1}$$

where k_z is the axial propagation constant (defined by the relation $\phi = k_z L$, with ϕ as the phase advance across one period and L as the length of one period), P is the total power flowing through the structure, and E_{z0} is the spatial Fourier component of the axial electric field corresponding to the axial propagation constant for the first spatial harmonic as:

$$E_{z0} = \int_0^L E_z e^{ik_z z} dz \Big/ L \quad \text{[14].} \tag{2.2}$$

The integration is generally accomplished on the axis of the structure as the integral over one period, but the impedance is often averaged over the surface area of the beam.

We provide some representative Pierce impedance data using simulated data for a device with parameters as in Table 2-I. The results of a calculation of Pierce impedance on-axis for the fundamental mode are presented in Figure 2.5 as a function of phase. The magnitude of this impedance is somewhat lower than in a round-beam slow-wave structure, but the increased current afforded by the sheet beam topology more than compensates for this. Notice that there is a singularity in the plot where the group velocity equals zero (refer to Figure 2.1). The solid line portion refers to the positive dispersion section of the curve, and the dashed line refers to the negative dispersion section. The behavior at the band edge is a cause of some concern and will be discussed in Chapter 4.

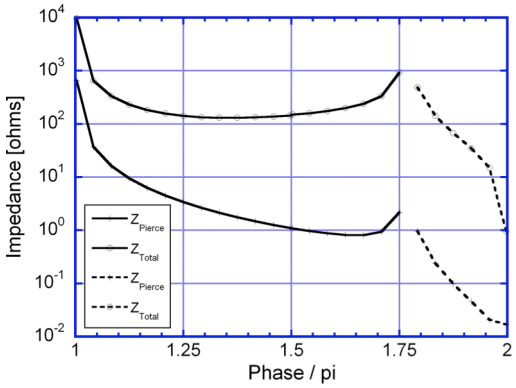

Figure 2.5: Z_{Pierce} and Z_{Total} vs. phase for the fundamental mode evaluated on axis (Z_{Pierce}), and evaluated at the beam-tunnel height, at the center of the long edge (Z_{Total}). The solid lines represent sections of positive dispersion, wheras the dashed lines represent sections of negative dispersion. The band edge appears near 1.75π.

The axial electric field of the fundamental mode varies as might be expected within the beam tunnel, with good uniformity in the wide dimension and like a hyperbolic cosine in the short dimension. We consider a sheet beam with a rectangular cross-sectional area that is 0.48 mm tall (50% tunnel height) by 4 mm wide (87% tunnel width), and centered in the beam tunnel, and consider a phase advance of 1.5π. The variation of E_{z0} across the wide dimension is less than five percent of the average. The variation of Z_{Pierce} across the short dimension is smooth with a minimum at the center, such that the value at the edge is 23% larger than the minimum, and a smooth symmetry exists about the midplane (hyperbolic cosine-like). Averaging Z_{Pierce} over the cross-sectional area produces a value of 1.230 Ω (we will use this value in the chapter on gain analysis).

Next, we find what is called the Total Impedance [4], [87], [88], which is defined as:

$$Z_{Total} = V^2 / (2P), \tag{2.3}$$

where

$$V = \left| \int_{-g/2}^{+g/2} E_z dz \right|, \tag{2.4}$$

g is the length of the cavity gap, and *P* is, again, the total power flow through the structure. This integration is generally accomplished at the beam-tunnel radius, which, in the case of a sheet-beam structure would be the half-height (in the short direction) of the beam tunnel (*i.e.* the voltage is meant to be a quasi-static representation of a potential difference between the opposing faces of the cavity). Data evaluated from simulation results is presented in Figure 2.5, along with the Pierce Impedance. Notice again that the singularity at 1.75π occurs when the group velocity is zero.

2d) Slow-Wave Structure Experimental Results

An experimental Ka-band slow-wave structure was built using conventional computer numerical controlled (CNC) milling techniques. The structure was made of copper, with some of the coupling waveguides made of aluminum. The dimensions of this test structure are the same as in Table 2-I. All measurements were performed with an Agilent E8364B network analyzer calibrated with WR28 waveguide connectors (covering a frequency range of 26.5-40.0 GHz).

The experimental results presented here fall under two categories: 1) reflection of a shorted structure, and 2) perturbation of the structure. The reflection measurements produce quantitative experimental data representing the structure's dispersion. The perturbation measurements provide a qualitative measure of the field at the perturber's location, and are quantitatively compared with simulations, experimentally confirming the field profile of the simulation.

The first experiment is a one-port reflection measurement to determine the dispersive properties of the structure. It is well-known that a structure of *N* periods will set up *N* resonances in the fundamental mode with evenly spaced phase between π/N and π (or π+π/N and 2π, as the structure is reciprocal and periodic) [4], [89]. The structure is stacked with 10 cavities, a solid conducting sheet is connected at the midplane of the 11th cavity, and a conducting sheet with a specially shaped coupling iris is placed at the midplane of the first

cavity. The shape of the coupling iris and the orientation of the exciting waveguide determine which mode is excited in the SWS.

For the symmetric mode, the coupling iris is a slot in the vertical direction that is made identical to the end slot in the structure, and the waveguide is oriented so that the electric field is symmetric across the length of the iris and therefore will be symmetric across the height of the SWS (see Figure 2.6 for a schematic of the physical setup). A second set of end-pieces was used that changed the placement of the conducting sheets from the midplane of the cavity to the midplane of the slots, which increased the number of cavities from 10 to 11, and changed the effective terminations from open-circuits to short-circuits. The results are plotted in Figure 2.7, where the experimental data are compared with the simulated dispersive characteristics with good agreement. Notice that a few points are missing at the low end due to the waveguide calibration starting at 26.5 GHz, and a point was unresolvable at the high end of the short-circuited case.

For the antisymmetric mode, the same procedure is used, but the coupling iris is adjusted to admit an antisymmetric electric field. Specifically, the coupling iris is a slot in the horizontal direction that is made identical to the beam tunnel in the structure. In this

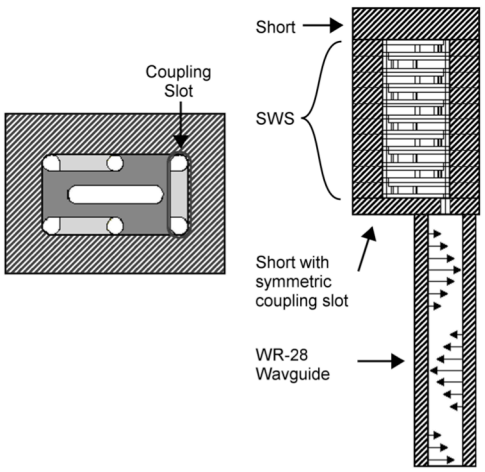

Figure 2.6: Resonance measurement setup. Notice that the waveguide is oriented to fit over the coupling slot, which is milled to the same size as Slot 2.

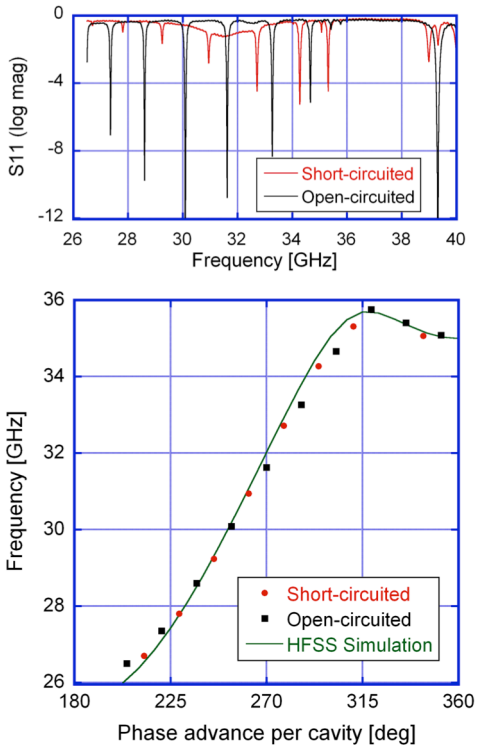

Figure 2.7: Resonance measurement results - frequency response and the corresponding frequency vs. phase diagram for the symmetric mode.

case, the waveguide is oriented so the electric field is pointed from the top of the beam tunnel to the bottom, which is the natural orientation of the antisymmetric mode. The experimental data in Figure 2.8 indicates that the resonances are closely spaced in the frequency range of the antisymmetric pass-band. Due to the severely overlapping nature of the frequency vs. phase relationship, and the compact range of frequencies, it is impractical to try to map these resonance frequencies into a dispersion relation, but it sufficiently confirms the frequency response at this point.

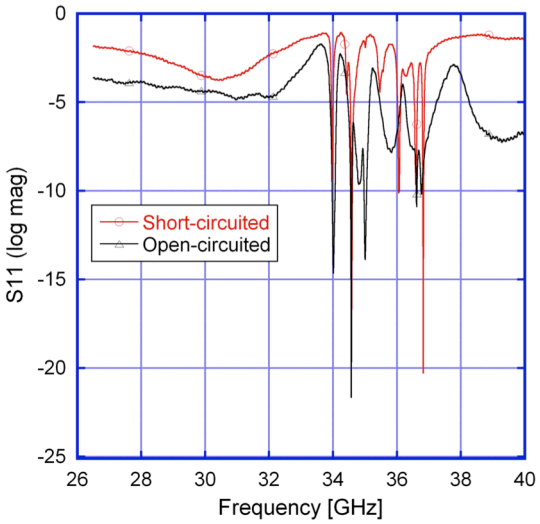

Figure 2.8: Resonance measurement - antisymmetric mode.

The second experiment is intended to probe the electric field within the structure. This is another one-port reflection measurement with a nearly identical setup to the first experiment, but the solid conducting sheet in the 11th cavity is replaced by a sheet with an iris shaped like the beam tunnel, in which the probe can be inserted. The probe is a 0.5 mm diameter, quartz rod that extends the entire axial length of the structure and is experimentally positioned using a two-axis stage controlled by micrometers. All measurable frequency resonances are monitored as the horizontal position of the perturbing rod is varied from one end of the beam tunnel to the other end. The data is then represented as the frequency shift from the un-perturbed resonances and the results are reported in Figure 2.9 and Table 2-IV. The important points that are drawn from these data are 1) the field is relatively flat across the length of the beam tunnel (no nulls are present), and 2) the frequency deviation is small, as would be expected for a longitudinal perturbation of a mostly longitudinal field.

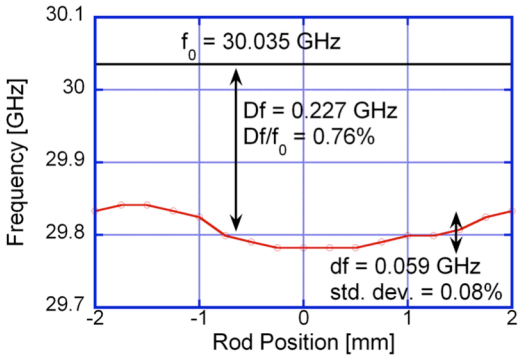

Figure 2.9: Perturbed resonance frequency vs. rod position - symmetric mode.

Resonance #	Phase [deg]	f_0 [GHz]	average f [GHz]	Df [GHz]	Df/f_0 %	df [GHz]	std. dev./f_0 %
3	220.91	27.386	27.195	0.191	0.70	0.034	0.04
4	237.27	28.567	28.364	0.203	0.71	0.051	0.05
5	253.64	30.035	29.808	0.227	0.76	0.059	0.08
6	270	31.655	31.399	0.257	0.81	0.059	0.07
7	286.36	33.242	32.964	0.277	0.83	0.076	0.08
8	302.73	34.743	34.410	0.334	0.96	0.110	0.09
10	335.45	35.738	35.553	0.185	0.52	0.127	0.12
11	351.82	35.503	35.317	0.186	0.52	0.059	0.05

Table 2-IV: Perturbation measurement data. Data for each resonance number are obtained from plots such as Figure 2.9.

HFSS driven-frequency simulations confirm the results of this perturbation experiment. The averaged Df/f_0 are compared (simulation vs. experiment) for each resonance frequency in Figure 2.10 – these values, although not identical, are good indicators that the simulation and experiment are both producing results as expected, and any discrepancies are likely due to cumulative, small-scale manufacturing errors. We thus have confidence to use the simulated field results to compute any field-derived structure characteristic (interaction impedance, *etc.*), as this requires no analytical approximations (only the finite element approximation), eliminates experimental error, and does not entail manufacturing of parts for testing.

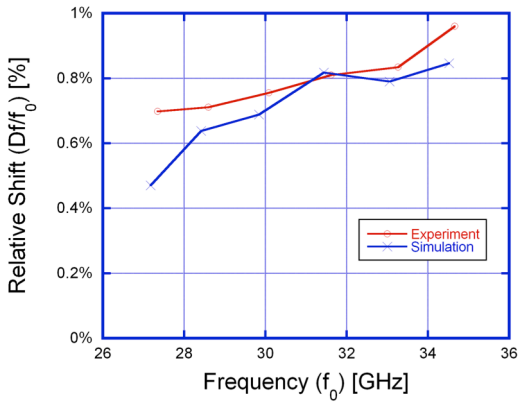

Figure 2.10: Relative shift in frequency vs. unperturbed frequency - symmetric mode pertubation experiment.

The same sort of perturbation experiment can be repeated for the antisymmetric mode, where the coupling iris and the waveguide are oriented to excite a transverse field within the structure. The results of this analysis are shown in Figure 2.11 and Table 2-V. The important points of these results are the following: 1) The field varies in magnitude and peaks towards the center of the beam tunnel with nulls at the edges. 2)

Resonance #	f_0 [GHz]	f_{min} [GHz]	Df_{max} [GHz]	Df_{max}/f_0 %
1	33.980	32.474	1.506	4.43
2	34.628	34.234	0.394	1.14
3	34.952	34.473	0.479	1.37
4	35.486	33.874	1.612	4.54
5	36.236	35.005	1.231	3.40
6	36.560	35.655	0.905	2.48

Table 2-V: Results of perturbation experiment - antisymmetric mode.

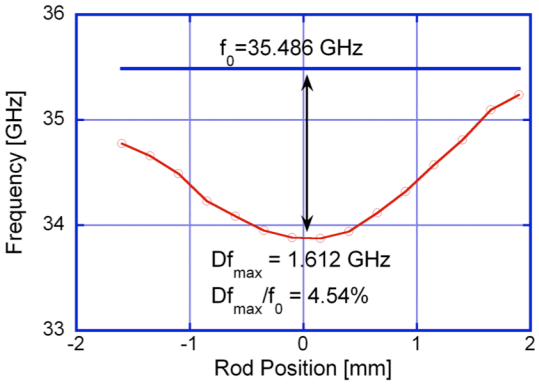

Figure 2.11: Perturbed resonance frequency vs. rod position – antisymmetric mode.

The magnitude of the frequency shift is large (about five times larger shift than the symmetric mode), as might be expected for a longitudinal perturber in a transverse field. 3) Probing the resonance frequencies makes it easier to distinguish the individual frequencies (which are still rather dense in frequency-space), but does not completely solve the problem of which resonance belongs to which phase advance (the overlapping frequency problem).

2e) Waveguide Couplers and RF Transmission

A matched coupler is necessary to eliminate gain ripple and instabilities as is necessary in conventional coupled-cavity tubes. The electromagnetic power that drives the structure is coupled in starting from a standard Ka-band rectangular waveguide (size WR-28). The coupler is designed to yield a good electrical match over the full frequency range of interaction, and yet be simple, robust, and compact [90].

A coupler was developed for the experimental slow-wave structure using a waveguide transformer into the short-edge of the input cavity (symmetrically exciting the field across the edge slot). Much use was made of the optimization facilities in the Analyst EM simulation tool with moderate success. A return loss of better than -15 dB over 6 GHz was realized in a transmission measurement on the network analyzer.

Subsequent to the development of this experimental waveguide coupler, an extensive design study has been performed on the matching capabilities of a waveguide transformer into a given sheet-beam SWS. The design process for the transformer can be labor intensive; however, several techniques may be employed to limit the size of the problem and minimize the time

required to achieve a successful broadband match. We briefly discuss the theory of matching a finite length of SWS via waveguide couplers and then share simulation results of a successful broadband match.

We start with simulations of a short, finite, uniform section of SWS with symmetric waveguide couplers on input and output cavities. The geometry is illustrated for an example in Figure 2.12, where the dashed black line represents the plane of symmetry created by using symmetric couplers. This simple configuration is used to match the couplers even if the final geometry is more complicated (due to severs, increased length, or changing cavity parameters) because it isolates the input or output junction, and reduces the model complexity. Through the simple conceptual analysis of this system we can understand the matched response and simplify the simulation requirements.

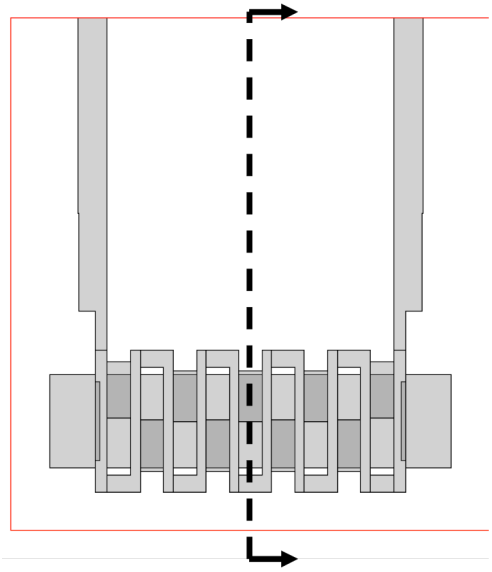

Figure 2.12: Back to back symmetric waveguide couplers attached to a short section of SWS.

The system represented in the geometry of Figure 2.12 has a uniform, periodic section surrounded by two input transmission lines with characteristic impedance Z_0. If we treat the SWS as a uniform transmission line of length L, and characteristic impedance Z_1, then within the passband of the SWS the overall system can be conceptualized as a weakly reflecting mirror cavity of inner length L and reflection coefficient $\Gamma_1 = \frac{Z_1 - Z_0}{Z_1 + Z_0}$ at each identical junction. It should be mentioned that the length L is an effective length that might practically change with frequency, but to first order will be assumed constant. With this model in place the total reflection experienced at the input can be expressed as the following:

$$\Gamma_{in} = \frac{\Gamma_1 {T_1}^2 \exp(-j2\beta L)}{1 - {\Gamma_1}^2 \exp(-j2\beta L)} + \Gamma_1 \tag{2.5}$$

$$\approx \Gamma_1[1 + exp(-j2\beta L)] \tag{2.6}$$

The approximation expression suggests that for a given length of structure the input response will oscillate in frequency between a reflection value of zero and a value twice that of the single junction. Simulated results for a simulated matched-SWS are pictured in Figure 2.13 – the local maxima are marked and connected, indicating twice the response of a single junction (in black), and the hypothetical response of a single junction (in grey) as the 6dB-reduced translation of the maxima.

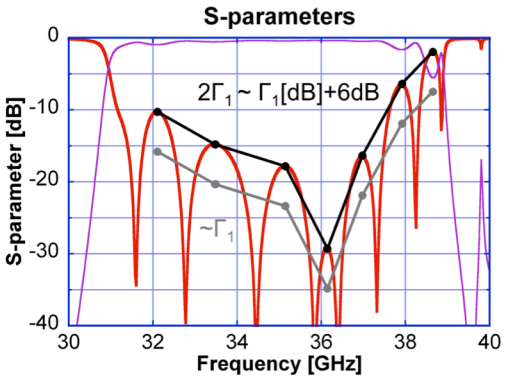

Figure 2.13: Simulation results for an example matched-SWS.

The crux of this argument is that this simple, back-to-back configuration provides the necessary information about the single junction reflection parameter, and it does so with as few structure periods as possible. To investigate the effect of the number of structure periods (changing the length *L*), we provide the results of a series of simulations and compare the S-parameter response. The plots provided in Figure 2.14 represent the return loss (S_{11} in log magnitude) for four different lengths of periodic SWS, but identical input/output couplers. The point of the comparison is that even though the results are different for each specific number of cavities, there are similar behaviors. The passband behavior of the SWS is exhibited in each plot, with a more sharply defined cutoff exhibited for more cavities. As the number of cavities is increased, we see an increasing number of maxima across the passband, but the exact locations are not easily predicted outside of simulation. Finally, the overall shape of the envelope of the maxima is consistent – we compare maxima from a complete set of simulations with number of cavities varying from four to twenty in Figure 2.15. The plot confirms that the overall envelope shape of the reflection seen at the input waveguide is dependent only on the reflection at the input/output junctions – it also suggests that we can use only a few cavities to determine the response necessary within the bandwidth of the fundamental cavity passband, however the resolution of the curve is improved with increased number of cavities.

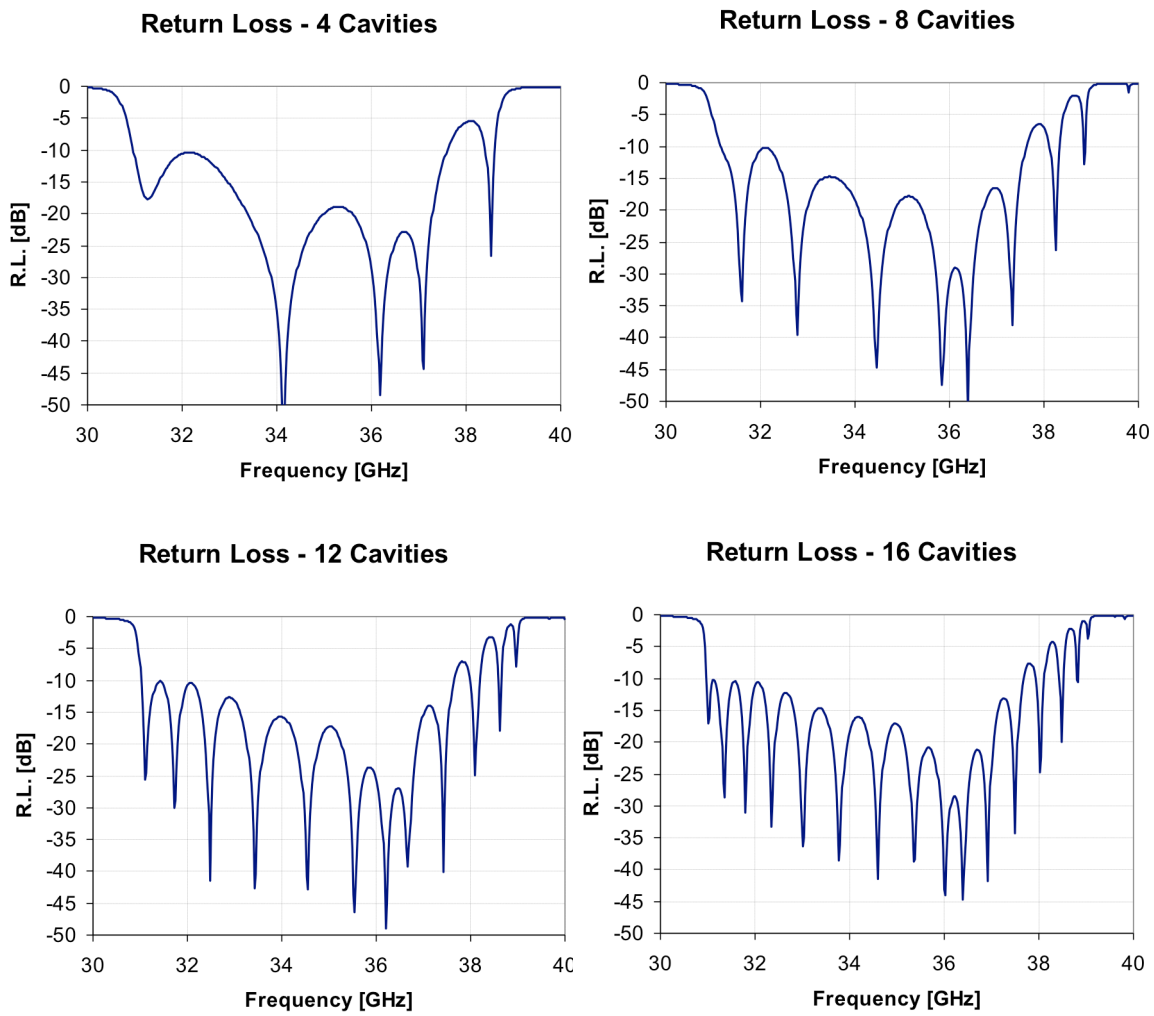

Figure 2.14: Simulation results for an example matched-SWS with varying numbers of cavities as noted.

The match into the input cavity is created by adjusting length of the coupling slot between the input cavity and the remainder of the SWS, and also by adding a capacitive post around the beam-tunnel (see Figure 2.16). We use a single input cavity to transition from the waveguide transformer to the desired slow-wave structure parameters in order to minimize structure length and complexity in this experiment (as opposed to multiple input cavity transitions

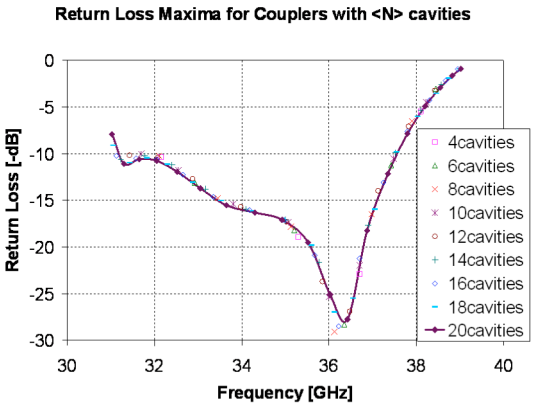

Figure 2.15: Maxima for a set of matching simulations including those in Figure 2.14.

used in some broadband matches). Adjusting the coupling slot length is equivalent to the filter concept of adjusting the input coupling of the filter to create a match; more precisely, the adjusted input coupling in conjunction with the additional waveguide steps create a broadband matching network through a precise sequence of mismatches. The capacitive post is created within the input cavity by extruding a region around the beam-tunnel (within the center of the cavity) in order to provide additional sensitive tuning of the match (*i.e.* directly tuned cavity capacitance), and also assists in the conversion of the fields from a waveguide TE mode into the desired SWS mode (*cf.* Figure 2.4).

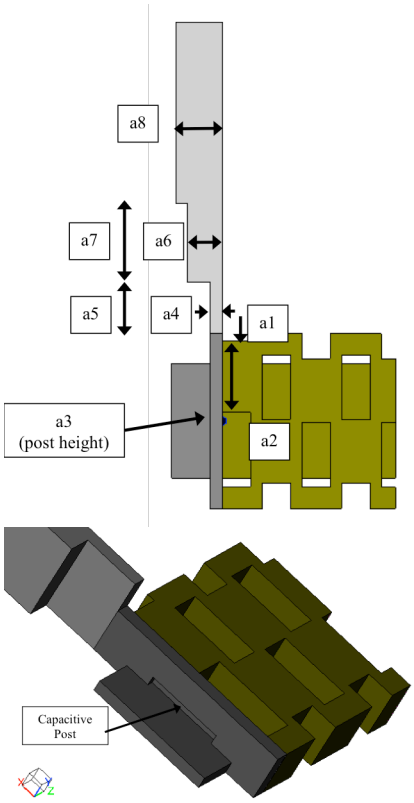

Figure 2.16: Geometry used in optimization simulations with optimization parameters labeled.

We set up a numerical optimization problem using a three-dimensional finite element method (FEM) simulation using parameterized geometry variables for the input cavity and waveguide transition. The geometry utilized in these FEM simulations is presented in Figure 2.16. The simulation utilizes a symmetry boundary that bisects the waveguide and the structure, and it also employs a unique symmetry-like boundary at the midplane of the slots (pictured on the right of Figure 2.16) – both symmetries allowing a reduced solution domain and faster solution times. The labeled dimensions represent the parameterized variables that are allowed for variation in the numerical optimization procedure.

One rule-of-thumb for a numerical optimization with computationally intensive function evaluation is to limit the number of optimization parameters, and this is achieved in several ways through this simulation. First, we see that using this back to back symmetric configuration avoids a possible duplicity of optimization parameters, as the geometry is mirrored onto the opposite waveguide coupler, and only one set of parameters requires changing. Second, we start with the waveguide at some intermediate height that may require further waveguide

transitioning to achieve the full, standard waveguide height – this reduces the number of optimization parameters, eliminates any requirements of achieving the full waveguide height in the geometry, and it again reduces the simulation domain (the final match from intermediate height waveguide to standard waveguide height is a trivial waveguide impedance match). Third, we eliminate parameters that do not have as much effect on the simulation results. The final set of parameters is required to make a good broadband match, and represents those necessary parameters of a waveguide match and a matching system within the first cavity.

The numerical optimization is coupled directly with the FEM simulation solver (*e.g.* Analyst), so that the optimization parameters within the geometry are updated according to the numerical optimization algorithm, and a user specified metric function is minimized through the software. The metric function that we specify looks for the largest return loss magnitude across a frequency band of interest and returns a scaled version of that number, *i.e.* $Metric\ Function = 20 + \max\{S_{11}(33-37\mathrm{GHz})\}[\mathrm{dB}]$. The main points of this computationally intensive numerical optimization are the following. First, it requires the simultaneous optimization of both the waveguide transition and the input junction, because a mismatch at either part would produce a sub-optimal response. Second, the metric function depends on the frequency spacing of the maxima (occurring at discrete points across the bandwidth), therefore a longer length may be required to obtain the maxima correctly across the solution bandwidth. And, although a long optimization can become stuck due to local minima, computer issues, or otherwise, after a completed optimization, there is generally a successful broadband match.

Three final, suggested points for the FEM optimization are as follows. First, if operating in the higher frequency portion of a given waveguide band, prior to starting the optimization, find a reduced waveguide width that has a cutoff frequency closer to the operating band of the SWS and start at that intermediate width in order to better match the dispersive and impedance characteristics of the waveguide and SWS. Second, whatever the method of frequency sweep employed in the FEM simulation, use a limited frequency band even if the full region of interest is much larger – the speedup is often significant, and the frequency response of the maxima is slowly varying by nature, so the match will likely continue outside of the optimized frequency range. Third, find a method of intelligently applying the mesh in such a way to obtain a single-pass solution that does not require adaptive or iterative meshing, yet retains reasonable

solution fidelity, for example, apply a resolved mesh in the input cavity and around the capacitive post.

Once the FEM optimization has produced a reasonable match across the bandwidth, we can refine the broadband match by re-optimizing the waveguide couplers with a cascaded scattering-matrix program and further numerical optimization. The structure's scattering matrix data from input cavity to output cavity is exported from the FEM software along with input terminal characteristics to create a frequency-dependent table for cascading waveguide matrices. We use a commercially available scattering-matrix code such as CASCADE [91] to manipulate and optimize the waveguide couplers through direct variation of the lengths and heights of the sequence of waveguide steps. This technique has been applied to optimize the bandwidth, match the waveguide height and width to standard waveguide sizes, and to minimize the total length of the waveguide coupler. The results of a standard optimization and subsequent comparison to a final FEM simulation are provided in Figure 2.17.

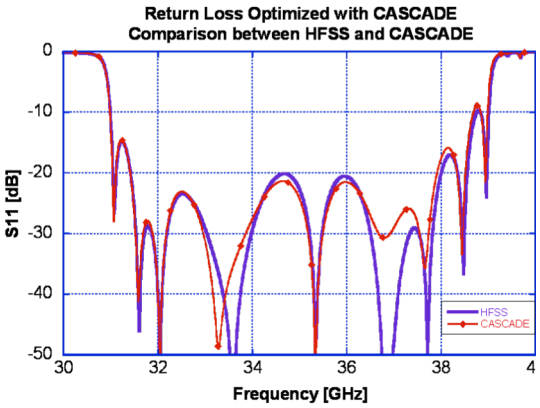

Figure 2.17: Optimized return loss over the frequency band of interest – comparison between FEM simulation and scattering matrix cascading.

If further complications in the structure need to be addressed, such as severs, or transitioning cavity sections with different cavity parameters, then the input junction and/or output junction can be optimized in the above manner and kept fixed. Then the optimization process can be applied to the sever or transition of interest with appropriately designated optimization parameters at the junction of interest.

2f) Slow-Wave Structure Geometry and Fabrication

At Ka-band frequencies, the slow-wave structure can be manufactured using conventional computer numerical controlled (CNC) milling techniques. The analysis of the inherent manufacturing errors due to prescribed machining tolerances, fixture implementation, braze processing, welding, tuning, and even thermal effects of the structure influence the electromagnetic design in order that sensitivities of the structure might be diminished or distributed as possible. Further, the complementary sensitivity analysis of the geometric

dependence of the structure response depends on our knowledge of these realistic limitations of the geometry's accuracy.

The geometry pictured in Figure 1.5 can be manufactured from a set of uniform solid rectangular plates of copper. These identically machined plates are then stacked and aligned with alignment pins – the stack can be either held together by mechanical means or by brazing the plates together to form a vacuum-tight circuit assembly. Manufacturing tolerances on the order of 0.0005" (12.7 μm) are achievable using state of the art milling techniques. The geometry, manufacturing, and tolerancing are considered in the analysis of the structure in the next section, and then, of course, in the design of the final experiment.

There are a couple complications that arise in the manufacturing and alignment of the structure that are unique to the sheet-beam geometry. The main complications lie in the dimension and alignment of the beam-tunnel height – all other parameter sensitivities and alignment criticalities are similar to a single-beam, round-beam SWS. The height of the beam-tunnel most directly impacts the strength of coupling between the electron beam and the various modes supported by the SWS (similarly to a round beam device) – if the total height is too large the coupling is weak and gain is reduced, however if the total height is too small the coupling is increased for all modes and an unintended instability may arise. Additionally, the beam-tunnel alignment must be critically controlled to suppress mode coupling and excitation, and also to prevent beam interception. The alignment is controlled first at the machining-tolerance stage, and then at the fixture alignment stage. In conventional structures, the alignment is usually accomplished by registering the stack of individually milled pieces at the outer edges, but often primarily aligned along the beam-tunnel with a precision mandrel [92]. In the sheet-beam structure, the beam-tunnel is too small and elongated to use an alignment mandrel that would meet both qualifications of providing increased alignment sensitivity and not becoming stuck within the beam-tunnel during the braze process. We plan on using a precision fixture to align the stack of individually milled pieces with fixture pins registering the outer edges of the plates, and using precision-ground gauge-pins to check the beam-tunnel height clearance before and after the braze process.

The braze process itself is well-understood, where a combination of temperature and pressure will cause an alloy to melt, seamlessly connect larger pieces of metal, and upon cooling, form one large metal structure. Brazing is an appropriate technology for microwave vacuum

electronic devices, as it creates superb electrical and thermal connections, is vacuum compatible (when using the right materials and correct brazing environment), and creates a vacuum seal that allows the outer walls of the coupled-cavity SWS to act as the boundary between the high-vacuum necessary for a high-quality electron beam and air outside of the SWS (a "vacuum-jacket" or "vacuum-sleeve"). When brazing is necessary at other junctions (such as the waveguide coupler), another braze alloy material with a lower melting temperature must be used to maintain the integrity of the first braze. For example, when brazing copper pieces a good choice of braze material is a gold/copper alloy, and the first braze step might use an alloy of 35% Au / 65% Cu, while the second braze step might use an allow of 30% Au / 70% Cu with a lower melting point.

The connection of the brazed SWS assembly to the gun and collector assemblies can be accomplished in many ways, often using some precision alignment pins and a weld flange on adjacent assemblies. The alignment of these assemblies is critical for beam-transport in a sheet-beam device, but is achievable, as demonstrated [26] [93]. Further, since we plan on reusing gun and collector assemblies from previously developed tests, the mating will be designed to match those already in use.

2g) Sensitivity Analysis

As mentioned in the previous section, the complement to the analysis of manufacturing tolerances is the analysis of the sensitivity of the electromagnetic properties of the structure to small changes in the structure. Sensitivity analysis has been important for all microwave devices, but is considered particularly important for millimeter-wave devices and also sheet-beam structures. Millimeter-waves represent a challenge because the manufacturing tolerances become a substantial fraction of the geometry scale as the frequency increases. Because sheet-beam structures are novel constructs with complicated fields, they must be analyzed carefully in this manner. In this section we study various SWS geometry perturbations and the associated sensitivity of the electromagnetic response.

In the definition of the geometry model for the eigenmode simulations, we use seven parameters (*cf.* Table 2-I, where the slot 2 length is the same as the cavity height) which we vary systematically to either side of the nominal. In one study, reported below, the results were obtained at 1° and 179° (corresponding to the two ends of the dispersion plots) for each of the

lowest three modes. The data in Figure 2.18 are an example of the results for a variation of the structure period (equal axial cavity and slot extents) where the period variable is varied from 3.135 mm to 3.215 mm (±1.3% variation) – the units of the y-axis are all in GHz. For each frequency measured, and for each variable varied, we obtain a sensitivity parameter, δ = d[length]/df * 100MHz (*i.e.* the change needed to shift the frequency by 100 MHz), which provides a measure of the possible amount of insensitivity for the specific parameter when constrained to a 100 MHz specification. The slope is obtained by doing a linear-least-squares line-fit on the five data points in each set. A larger number means that there is less sensitivity.

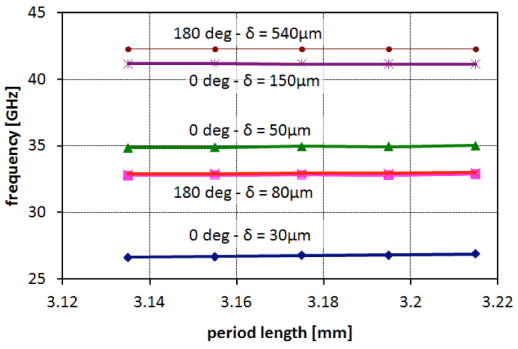

Figure 2.18: Variation in frequency of six resonant modes vs. period length.

The sensitivity parameters for all seven variables are presented in Table 2-VI. For comparison, the 0.0005" value listed as a reasonable value of accuracy in conventional milling techniques is equal to a δ_{limit} = 12.7 μm. Clearly, the sensitive variables are the coupling slot lengths and the cavity height (which also affects coupling between cavities). We feel confident that structures we manufacture will match the cold-simulated behavior of the slow-wave structures that we design, further confirmed by the successful cold-test experiment detailed above.

Measurement	Mode 0	Mode 1&2	Mode 3	Mode 4	Mode 5
period	30	80	50	-150	540
slot 1 & 2 width	-39	-75	420	-40	52
slot 1 length	-13	-15	-39	-43	-140
cavity width	82	240	-36	-300	-41
cavity height	-21	-23	-27	-12	-15
beam tunnel					
width	430	650	230	600	213
height	54	43	500	29	233

Table 2-VI: Sensitivity parameters (μm/100MHz) for each of the simulated SWS parameters.

We also investigate the sensitivity of the RF couplers using nominal parameters around those for the semi-optimized coupler case above. Since the goal of the coupler is to match the waveguide input to a given structure, we investigate the sensitivity of the parameters in a similar manner as above, with a fixed SWS we vary individual parameters of the couplers to find how sensitive the coupler is to a specific variable. The geometry of the couplers with slow-wave structure is illustrated in Figure 2.19, with the variable parameters labeled. It is more difficult to establish a single-value parameter for this broadband response, as reasonable variations have more complicated response than might be implied by linear variation of the metric function used in optimization. For example, the return loss magnitude across the full bandwidth is displayed in Figure 2.20 for variation in the height of the capacitive post in the input cavity. The variation in the post-height is ±0.0005", while the nominal height of the post is 0.011", for a ±4.5% variation. Through qualitative comparison of these variations, we find that the most sensitive parameters for the wellness of coupling are this capacitive post height, and the length of the first coupling slot. These are the important parameters for conventional coupled-cavity matching sections, so we continue to expect similar performance with the sheet-beam configuration. As a final test of the sensitivity of the coupler design, we allowed all the labeled parameters in Figure 2.19 to vary randomly with uniform probability distribution over the range ±0.0005" and compared the resulting return loss to the nominal case. The results of this comparison are found in Figure 2.21, where it is seen that although a noticeable change occurs in the return loss, the change is 12-15 dB down, which is a respectable coupling even if below our goals.

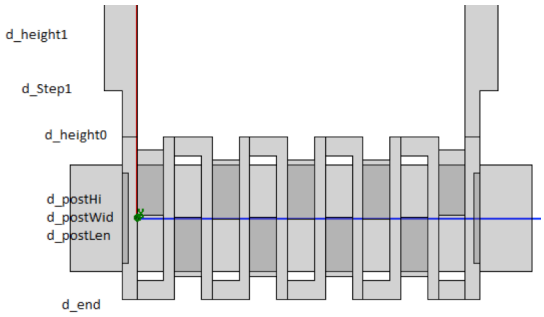

Figure 2.19: Geometry of coupler and dimensions used to study sensitivity.

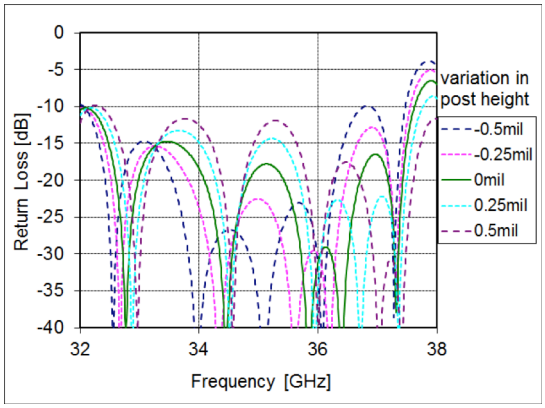

Figure 2.20: Example results of a variation of the post height for coupler sensitivity analysis.

Several other investigations of sensitivity will arise through the various topics in this thesis. We investigate the coupling between longitudinal mode and transverse mode by coupler and random misalignments in the elongated beam tunnels, and their effect on the stability and excitation of transverse modes. We also investigate gain interaction and sensitivity to period length, beam-tunnel height and offset, and beam dimensions, beam voltage, and beam current. This will be reported later once the methodology to estimate gain has been established.

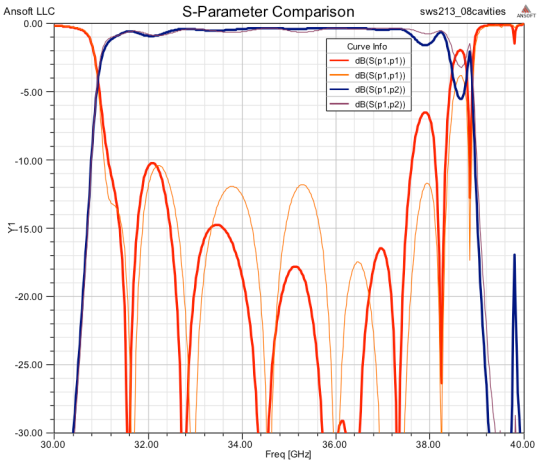

Figure 2.21: Return loss across entire frequency band – nominal case and randomly varied case.

Chapter 3: Sheet-Beam Gain Analysis

The amplifier operation of a coupled-cavity structure using a sheet electron beam can be described analogously to conventional traveling wave structures. We have already characterized the dispersion and fields of the structure, and found that the electric field is mostly uniform over the cross-section of the beam for the lowest symmetric mode. For the majority of the following analyses we will assume that field of the fundamental operating mode is uniform and that the beam is of uniform rectangular cross-section. We postulate that this is a good assumption due to the relative uniformity of the field and beam, and this assumption is confirmed through simulations that take into account the exact electric fields of the structure and realistic electron beam distributions.

The interaction of the beam with the electromagnetic fields of the structure will be separated into the study of the symmetric and antisymmetric modes. It is assumed that in this device only the symmetric mode is excited at the input cavity by a well-matched coupler and that any sever does an equally good job at absorbing the symmetric and antisymmetric modes – this is a beginning to our justification for ignoring the antisymmetric mode in this chapter, and we will treat the antisymmetric mode as an instability to be discussed in Chapter 4.

The amplifier gain is estimated using several different methods to investigate various effects and assumptions in the operation of a sheet-beam coupled-cavity amplifier. Many various analyses have been developed and documented in the literature for round-beam devices [4] [5] [94]. We have adopted several of these analyses to a sheet-beam configuration as detailed in the text. The following analyses have been used directly in this work to estimate the gain and stability of a given design, and through the course of explaining the analyses we will highlight necessary assumptions or approximations and useful design rules. First we investigate an analytical, small-signal theory developed for TWTAs and discuss the effects of the sheet-geometry. Then we use two simulation tools to predict performance over a range of frequencies and drive powers and to provide comparison to the analytic theory. Finally, we validate these models with fully 3D particle simulations with very few simulation assumptions. In this chapter, we do not use the parameters of the proposed device, but explore the properties of the structure through several variations of geometry – the simulated results of the proposed device are included in Chapter 5.

3a) Sheet-Beam Pierce Analysis

A sheet electron beam traveling axially through a coupled-cavity structure operates analogously to conventional round-beam traveling wave structures. The beam interacts almost continuously over the length of the structure, and the velocity modulation impressed upon the beam is in synchronism with the impression of the bunched current on the slow-wave structure (SWS). This continuous, synchronous interaction produces a convective, growing wave, which leads to the amplified signal.

We start by assuming that an RF modulated signal exists in the structure with sufficiently small amplitude such that the electron beam energy is not strongly perturbed by it (alternatively, the bunched AC-current in the beam must be much smaller than the total DC-current). This condition assumes that the device is operating stably, and that there is a very small input microwave signal within the passband of the amplifier. Then the resulting signal at the output of the device will be a linearly amplified copy of the input signal. Due to this linearity, and to further simplify the analysis, we will assume a signal of a single frequency within the band of interest such that the electric field, magnetic field, and current densities all contain an oscillating component $e^{-i\omega t}$.

Pierce found a differential form for the interaction of a one-dimensional electron beam with a slow-wave transmission line model [5] [2]. He developed an expression for the beam influence on the circuit fields and the circuit field influence on the beam, and on combining the two expressions, he developed a relation for the propagation and growth of an electromagnetic wave interacting with the electron beam. The equivalent analysis for the small-signal gain of a sheet-beam structure is, by the nature of the 1D approximation, the same as that of a round-beam structure – the only difference entering when including factors for the average interaction and factors to account for space-charge debunching effects in the beam, as derived in Appendix I.

Assuming that the fields are predominantly in the axial direction (which is appropriate for symmetric modes in the sheet-beam structure), we may start by finding the gain per cavity of the fundamental mode. Using the beam averaged Pierce Impedance computed with Equation 2.1 in Section 2e, we estimate the linear, small-signal gain following [2]. The gain is calculated using the following simple formulas:

$$C_{Pierce}{}^{3} = \frac{Z_{Pierce} I_0}{4V_0} \tag{3.1}$$

$$N = \frac{k_z L}{2\pi} \tag{3.2}$$

$$G = -9.54 + 47.3 C_{Pierce} N \tag{3.3}$$

where I_o is the beam current, V_0 is the beam voltage, L is the length of the circuit, and k_z is the axial wavenumber corresponding to the frequency of interest. As an example, we use the SWS parameters of Table 2-I of the previous chapter, Z_{Pierce} = 1.230 Ω, V_0 = 13.3 kV, I_0 = 1 A, and L = 31.75 mm (20 cavities), and compute C_{Pierce} = 0.0285, N = 15 wavelengths, and G = 10.7 dB. We remark that the values in Table 2-I are yet un-optimized values for the structure and beam parameters, yet it is encouraging that we can obtain a modest (though respectable) gain from a short, uniform section of 20 cavities.

In Table 3-I we find a new set of parameters for a slow-wave structure that has a center frequency at 35 GHz, operates with an electron beam at 19.5 kV and 3.5 A of rectangular cross-section 4 mm x 0.3 mm (which are the desired beam parameters), and has a stronger beam-wave interaction. This structure represents one of the several test-structures with a rectangular ferrule (an extruded nose within the cavities, which creates a concentrated electric field near the beam-tunnel) surrounding the perimeter of the rectangular beam-tunnel – thus, a few extra parameters appear in the table. The additional variables introduced in Table 3-I represent the following: *septum thickness* is the axial thickness of the copper plot in which the slot and beam-tunnel holes are punched (34% of the period), *ferrule height* is the axial extent of each opposing nose (the remaining gap length is calculated to be 39.6% of the period length), and *ferrule thickness* is the transverse extent of the rectangular nose away from the rectangular

SWS Parameter	[in]	[mm]
period	0.068	1.727
slot 1 & 2 width	0.030	0.762
slot 1 length	0.133	3.378
slot 2 length	0.135	3.429
cavity width	0.245	6.223
cavity height	0.135	3.429
septum thickness	0.023	0.587
ferrule height	0.009	0.228
ferrule thickness	0.004	0.102
beam tunnel		
width	0.175	4.445
height	0.030	0.762

Table 3-I: Parameters for the simulated slow-wave structure.

beam-tunnel perimeter. The various test-structures including ferrules did not perform significantly better than similar structures without noses, so these were not retained in later iterations. We performed a full small-signal analysis of the structure in Table 3-I using the developed analysis and the following presents representative data of that analysis.

We solve the standard cubic Pierce equation allowing for space-charge reduction in a semi-infinite laminar-sheet geometry using a numerical solution for frequencies across the fundamental pass-band. The cubic equation solution provides the growing wavenumber, k_z, which is converted into gain per unit length. The total gain is calculated as:

$$G_{tot}[dB] = A_{launch} + G_{wavelength}\,[dB/wavelength] * N \qquad (3.4)$$

where A_{launch} is the launching loss, $G_{wavelength.}$ is the gain per length, and N is, again, the number of SWS wavelengths in the length of uniform structure under consideration. $G_{wavelength.}$ is computed as above for each frequency across the band, and A_{launch} is computed for each frequency using the analysis in [95]. The results are plotted in Figure 3.1 along with some simulation results to be subsequently discussed.

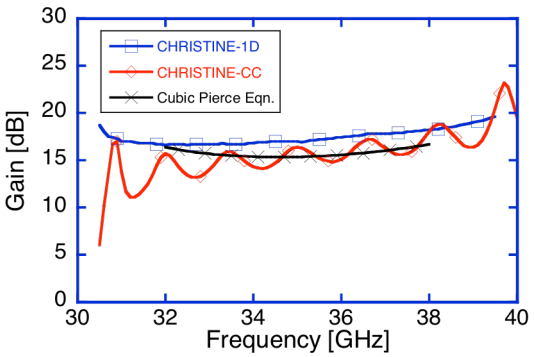

Figure 3.1: Small-signal gain plots for three different analyses: two simulations, and one analytical (computed numerically).

The analytical results in Figure 3.1 labeled *Cubic Pierce Eqn.*, represent the small-signal gain experienced by a sweep of single-frequency small-signal inputs acting on an axially uniform structure of 12 identical cavities (a total length of 2.06 cm). These results promise large gain per cavity and large bandwidth for this structure. However the high gain, large bandwidth, and increasing gain at the band-edges are all suggestive of oscillations at the π and 2π points (near 30GHz and 40GHz) which turn out to be the case, and will be discussed in detail later. There are further complications with the higher-order modes of this structure that are not predicted by the small-signal analytical theory of this structure, and these will be developed through alternate analyses and through 3-D particle simulations for which we will refer back to this structure for an example, and to these results for comparison. The final conclusion of this analysis is that the results are suggestive of small-signal gain and bandwidth,

and also suggest at possible instabilities in the fundamental mode, however further analysis is required.

3b) CHRISTINE-1D and CHRISTINE-CC Analysis

The previous analysis has several deficiencies that can be addressed by finding a numerical solution for the beam-wave interaction. The first deficiency appears in the need to represent finite and axially changing characteristics of realistic devices by axially varying the transmission line model in dispersion, impedance, and attenuation. This is not included in the above analysis, but is defined through the numerical simulation. Second, is the automatic inclusion of space-charge effects that reduce the gain of a real device. The third deficiency is in the small-signal nature of the above estimates, which does not allow for an estimate for the maximum, or saturated, output power.

The above limitations of the Pierce analytical model are met by performing numerical simulations. The simulations allow for axial variations in the structure parameters, include space-charge effects through numerical techniques, and are compatible with nonlinear large-signal drive powers. However, the 1-D numerical simulations retain limitations associated with the rigid disc electron beam approximation (*e.g.* no transverse beam expansion or contraction).

The traveling-wave tube parametric design code CHRISTINE-1D [94] was designed and validated for devices with cylindrical electron beams (helix structures [96] [97] [98], folded waveguide SWS's [99] [100], and others), and has been adapted for sheet-beam interactions. Because the beam-wave interaction is defined by a 1D axial expression, the only adaptations necessary for sheet-beam analysis are the beam-averaging calculation of the interaction impedance, and the space-charge reduction coefficients. An outline of the steps required for adjusting these coefficients is presented in Appendix I.

The input parameters for the simulation are the dispersion and impedance values obtained from the frequency-dependent electromagnetic simulations of the SWS geometry along with beam voltage, current, and the transverse cross-sections of the beam and beam-tunnel. Therefore, the gain simulations are not derived directly from the geometry, and require several assumptions based off analysis and experience. The first assumption of the CHRISTINE-1D code is that the interaction is continuous along the axial extent of the structure, whereas in a coupled-cavity structure the interaction has disjoint gaps with varying levels of field strength. A

periodic interaction structure may be analyzed as a continuous interaction by including a gap coupling coefficient as derived in Appendix I. The second assumption is that the interaction is 1D and uniform across the cross-section of the electron beam – we account for this 1D assumption by averaging the effect of the interaction over the cross-section of the beam. These are the same two assumptions made in the analytical small-signal gain expression above. These assumptions allow for fast calculation of the interaction from only the electromagnetic simulations of the SWS geometry. Besides these two assumptions, the rest of the analytical assumptions of an axially-infinite structure are not required – indeed only a short section of the structure is used, although the example discussed presently is periodic in the axial direction which produces the same effect as assuming a semi-infinite structure.

The results for the example case of the previous section are plotted in Figure 3.1, with the CHRISTINE-1D results labeled as such. The simulation provides results for any frequency within the interpolating range of the dispersion and impedance data that are provided to it. Although simulations with large input powers are allowed, the results in Figure 3.1 are for a case with small input power (P_{in} = 1 mW) in order to compare with the analytical results. The differences are most likely due to the actual launching loss experienced by the beam, where launching loss is the term used to suggest that power from the input signal is required to initiate the bunching action that convectively grows to produce the amplified signal.

The second simulation tool that we use to estimate traveling-wave tube gain in coupled-cavity structures is CHRISTINE-CC [101]. This code was also designed for cylindrical-beam devices, and compared against experiment [102], with nearly identical adaptations for sheet-beam devices. The two main differences with CHRISTINE-1D, are that the dispersion and impedance are formulated specifically for a coupled-cavity structure (allowing forward and backward coupling of cavities), and the fields are represented as separate cavity-fields of which the cumulative phased response interacts with the beam. The dispersion and impedance are evaluated as a function of frequency by implementing a circuit model appropriate to the response of a periodic unit cell of the cavity structure [84] [103] – this produces an inherent backward wave that exists on a real SWS. In contrast to CHRISTINE-1D, which assumes only a forward-wave interaction, CHRISTINE-CC requires an iterative solution to simultaneously find the beam behavior and field strength of each cavity. The beam-wave interaction still follows the 1D assumption, and

therefore the interaction is automatically averaged over the beam cross-section within the simulation code, keeping a standard 1D rigid-disc beam representation.

In CHRISTINE-CC the input parameters are defined in terms of a circuit model whose circuit element values are computed to provide a best fit match of the dispersion and impedance characteristics obtained from the electromagnetic simulations of the SWS. While the coupled-cavity simulation does not directly compute the fields within the 3D cavity geometry, the combination of the best fit circuit model for the dispersion and impedance, and the increased fidelity due to the disjoint cavity-field definition (see Appendix I for a discussion of gap fields and gap coupling coefficients) makes this an attractive alternative to the continuous interaction models used previously. Further information on the circuit model and the simulation code can be found in references [102] [103] [101]. The only additional points not found in the references are regarding the sheet-beam implementation, which are identical to those for the prior 1D simulation tool (*i.e.* the coefficients of the space-charge depression, and the beam-averaged field for the interaction calculation). The final point addressed in the most recent paper by Chernin, *et al.* [101] is that the CHRISTINE-CC and CHRISTINE-1D results should be similar for small values of C_{Pierce}.

The results for the identical example case of the previous section are plotted in Figure 3.1, with the CHRISTINE-CC results labeled as such. The value of equivalent $C_{Pierece}$ for this example varies across the band, but is ~0.07 at midband, which is moderately large (and is good for gain and bandwidth, although difficult for stability), but not unreasonably close to one so that most approximations hold very well. The ripples present in the CHRISTINE-CC case are due to the forward and backward waves supported by the structure and by mismatches at the input and output junctions (the ripple-frequency spacing is the inverse of the round-trip transit time for a signal from input to output back to the input), and this is a well-understood phenomenon [104] [105].

The comparison between the CHRISTINE-1D and CHRISTINE-CC results is a further comparison and validation of the analysis developed in the Appendix. CHRISTINE-1D assumes a continuous interaction with an interaction impedance given including all relevant coupling factors. In comparison, CHRISTINE-CC formulates the problems in terms of the actual field shapes and requires an impedance with no coupling factors where this impedance represents the actual voltage squared over power ratio for both the SWS gap and for the circuit model used in

simulations. The remainder of these simulations will utilize CHRISTINE-CC, as this shows what we believe to be the most realistic results from the various analyses and design codes (not including fully 3D particle codes).

As a fast design tool, these simulation codes are useful in studying parameter variations and their effect on the gain and response of the amplifier device. Through the course of the development of the sheet-beam coupled-cavity amplifier, we performed numerous variation studies in order to understand the behavior, optimize performance, and quantify the sensitivity of the device to perturbations. Some of these studies were performed in response to instabilities, in order to investigate behavior with varying beam parameters, to apply optimal techniques of instability suppression, or to weigh the relative merits of various strategies.

The most fundamental variation analyses to perform with CHRISTINE-CC are variation of drive power and frequency, obtaining device gain for all levels of input power and frequency. This analysis will demonstrate the maximum power (saturated power) attainable from the amplifier, the achievable power with a limited drive power, and the total device bandwidth at a given power level. For example, in Table 3-II we introduce another set of parameters for a slow-wave structure that has a center frequency at 35 GHz, operates with an electron beam at 19.5 kV and 3.5 A of rectangular cross-section 4 mm x 0.3 mm, and has a moderate beam-wave interaction. This structure does not utilize a rectangular ferrule (or nose) around the rectangular beam-tunnel – thus, no extra ferrule parameters appear in the table. The one additional variable introduced in Table 3-II, *slot 1 offset*, represents a transverse offset of the parallel coupling slots from the short cavity wall – this allows for additional flexibility in the adjustment of the dispersion and coupling between modes without unnecessarily reducing the bandwidth of the fundamental mode.

SWS Parameter	[in]	[mm]
period	0.066	1.676
slot 1 & 2 width	0.035	0.889
slot 1 length	0.105	2.667
slot 1 offset	0.042	1.067
cavity width	0.290	7.366
cavity height	0.145	3.683
septum thickness	0.047	1.190
beam tunnel		
width	0.190	4.826
height	0.035	0.889

Table 3-II: Parameters for the CHRISTINE-CC simulated SWS.

A full sweep of drive frequencies and powers was performed for a device with parameters as in Table 3-II and representative data are illustrated in Figure 3.2. These data represent normal

operation of the amplifier with fixed structure and beam parameters, and variable drive signal over a broad range of possible drive frequencies and powers. This plot is our first illustration of the large-signal response of a finite length of a TWTA with realistic beam parameters – note that for small drive powers the amplitude response is linear, while for large drive powers the amplitude reaches a maximum and decreases somewhat.

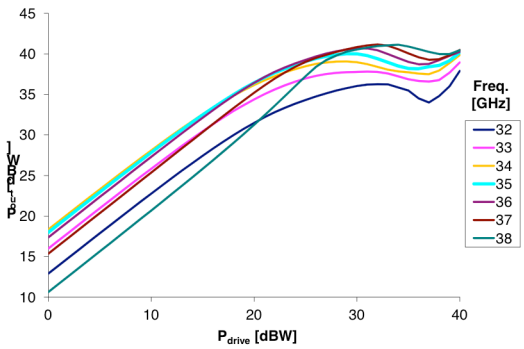

Figure 3.2: CHRISTINE-CC drive curves at varying frequencies. Device composed of 24 identical cavities with parameters in Table 3-II, V_{beam}=19.5 kV, and I_{beam}=3.5 A.

During efforts to suppress instabilities, and yet retain suitable amplifier performance, several cavity designs and device parameters were adjusted to find an optimal amplification. A set of cavity data was obtained from 3D FEM simulations, and the cavities were allowed to change axially in specific ways to suppress instability and increase interaction – specifically, the cavity-to-cavity spacing was allowed to vary in a simple way, and the total length was increased in order to obtain sufficient gain while maintaining bandwidth. The attenuation level was adjusted for stability, with axial variation in attenuation in order to reduce total loss and improve performance, and was thus simulated. In the investigation of band-edge oscillations, the beam voltage and beam current were varied in order to find stability margins at the band-edges. All of these points will be elaborated in the following chapter on stability analysis, but are fundamentally just variation analyses of a stable amplifier for the purpose of optimizing the device for increased gain and bandwidth.

In addition to the nominal variations used to probe the stable driven operation of a given device and the investigations of optimizing device parameters within the constraints of stability, there are several parameters for which we investigate their sensitivity due to manufacturing concerns or due to their being unique to the sheet-beam geometry. The first parameter of concern is the beam-tunnel height, which is a direct analog to the beam-tunnel radius in a round-beam CC-TWT. Because there is no ferrule (or nose) around the beam tunnels extruding into the cavities, the beam-tunnel height does not have a large effect on the cavity's frequency response or voltage at the beam tunnel, only the fields within the beam-tunnel cross-section [106] [107] (confirmed with HFSS simulations). The beam-tunnel height was varied manually within the

CHRISTINE-CC input file, and the Kosmahl-Branch analytical field expansion used to automatically calculate the interacting field for any beam-tunnel height – the results are plotted in Figure 3.3. As a comparison of the analytic gain approximations and field expansions we compare the effective change in impedance with beam-tunnel height. Looking at the gain at mid-band, using Eqn. 3.3 to find the Pierce gain coefficient, and then Eqn. 3.1 to find the effective impedance for each beam-tunnel height, we find that the sensitivity of the impedance to change in height is -6.66 Ω/mm – whereas, if we assume only that the beam-tunnel coupling factor varies as the hyperbolic-cosine, as in the theory presented in Appendix I, the sensitivity of the impedance is predicted as -4.29 Ω/mm (the negative sign signifies that the impedance decreases as the beam-tunnel height increases). Clearly, the beam-tunnel height has a direct impact on the space-charge reduction effects and other factors that moderately affect the gain calculation. Also, notice that for small enough beam-tunnel height the gain ripple increases uncontrollably and possibly unstable behavior occurs – this is confirmed with 3D particle simulations.

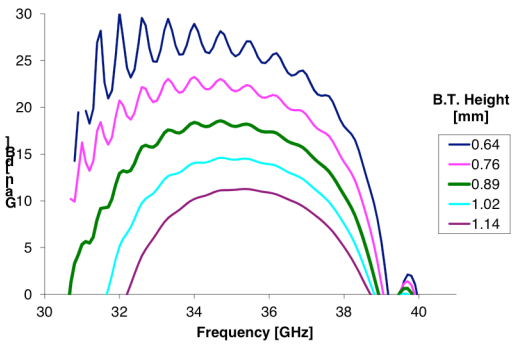

Figure 3.3: CHRISTINE-CC bandwidth curves at varying beam-tunnel heights. Device composed of 24 identical cavities with parameters in Table 3-II, V_{beam}=19.5 kV, and I_{beam}=3.5 A.

The variation of beam-height has similar results to the variation of beam-tunnel height, except with a positive relation and a reduced sensitivity. The initial beam has a beam-height to beam-tunnel height ratio of ~34%, and from a set of CHRISTINE-CC simulations, we find that the sensitivity of the effective impedance is 2.25 Ω/mm in beam-height variation. This is substantially different from the ballistic analysis prediction of 6.32 Ω/mm, due to space charge effects and otherwise. This sensitivity to beam-size (and, more generally, the beam density distribution) is important because the actual, thermal beam that will be used in the structure has somewhat indeterminate height, and the beam-height may change as the beam interacts with the slow-wave structure. Overall, the sensitivity of device gain and other characteristics seems acceptable due to variations in beam-height as demonstrated in these simulations and further 3D particle simulations.

The sensitivity to period length is of concern due to the manufacturing and alignment process. Specifically, the thickness of the braze material after the braze process is of concern. This parameter has several effects, with the possibility of significantly impacting the dispersion and impedance, and also affecting the general synchronism with the beam. In order to investigate both of these points we performed two sets of CHRISTINE-CC simulations: the first set of simulations only adjusted the period descriptor within the simulation input such that the periods were uniformly varied by ±0.001" from the nominal with the dispersion and impedance kept constant, and the second set of simulations used separate dispersion and impedance data computed from 3D electromagnetic simulations with uniformly varied periods (and cavity depth due to the usual placement of braze material). The results of these two sets of simulations are presented in Figure 3.4 for a device with SWS described in the final chapter, and a step in the SWS period (as described in the following chapter on stability). Clearly, the period length has an effect on the gain peak, the frequency tuning, and the bandwidth. However, the uniform variation of 0.001" still appears within reasonable operation, and this is a larger variation than we expect from manufacturing or brazing tolerances, which are expected individually to be within ±0.0002" (randomly distributed) of the nominal dimensions.

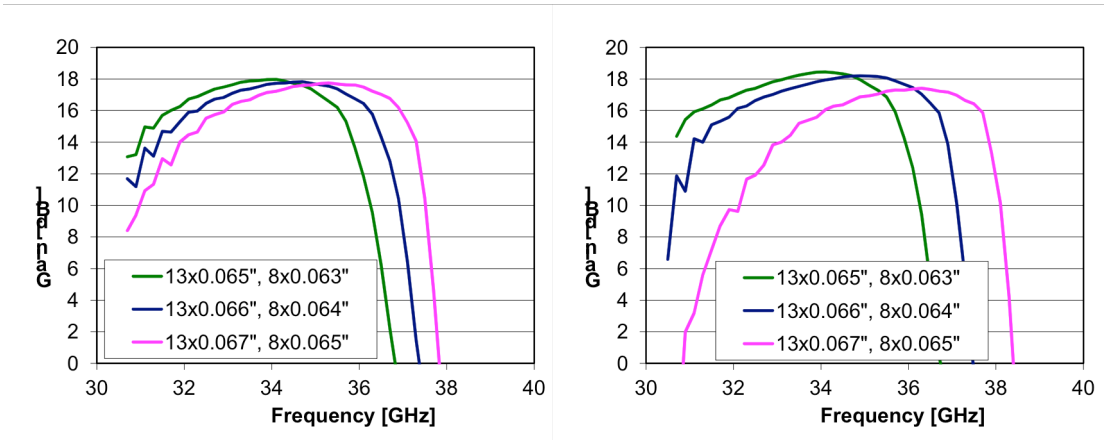

Figure 3.4: Gain vs. Frequency plots for a 21 cavity structure with a 200 W drive power – CHRISTINE-CC study of period length variation. a) Only the period variable is adjusted. b) Period and cavity depth are adjusted in 3D electromagnetic simulations, with SWS data defined separately in each CHRISTINE-CC simulation.

3c) MAGIC3D Simulations

In order to address the 3-dimensional nature of the coupled-cavity structure, beam, and their interaction, we utilize the fully 3D particle-in-cell (PIC) finite-difference electromagnetic solver

MAGIC3D [108] to simulate the amplifier characteristics under a variety of circumstances. These simulations confirm 1D gain estimates, exhibit oscillations when present, and provide field and particle data suggesting methods to improve interaction and avoid instabilities. Finally, a suite of simulations with small offset confirms the insensitivity of the structure to manufacturing tolerances, and also the overall stability of the structure to oscillations of various nature.

MAGIC3D is a user-configurable software tool [109], meaning the user can select and configure the solvers corresponding to the class of problem that the user is studying. There are fundamentally two connected solvers, the electromagnetic field solver and the particle-pusher algorithm. Because we require a full-wave solution, yet we have non-relativistic particles, we can use the default solvers with fine-tuning to increase performance. The default electromagnetic solver is a standard explicit finite-difference time-domain algorithm on a Cartesian grid [108], so the resolution of the simulation is limited by grid size, and the grid size limits the size of the time-step (due to the Courant stability condition), so a well-resolved geometry requires significant computational resources (mostly time, as memory bandwidth is a limiting factor on a good workstation computer). The default particle-pusher algorithm uses the Boris split time explicit scheme [108], which is appropriate for non-relativistic particles, and can be tuned for performance by increasing the number of electromagnetic time steps per particle step, so long as the particle does not traverse a Cartesian grid cell in one particle time step. These fundamental concerns and several specific details (port definition, particle definition, magnetic-field definition, input signal definition, *etc.*) were taken into consideration in the setup of the simulations to achieve optimal performance and fidelity.

Figure 3.5 shows the MAGIC3D model of a 14-cavity Ka-band sheet-beam CCTWT with two waveguide ports. This is a single section structure with no sever, and will be useful as a comparison to the uniform structure gain estimates in previous sections. Notice that due to the Cartesian grid used in the simulation, we use rectangular cavity geometries with squared corners. The geometry shows the input and output waveguide couplers connecting to input and output cavities and a uniform section of periodic coupled-cavities with a beam tunnel extending through the length of the structure. The visibly meshed objects are the conducting walls of the cavities and waveguides, and can be assigned any reasonable value of conductivity (or be perfectly conducting). The solution domain is the vacuum interior of the conducting objects,

and the ports defined on the open ends of waveguides and the opposing ends of the beam-tunnel.

PIC simulations have been used to investigate vacuum electronic devices of all types in many applications [110] [111]. Specifically, linear beam amplifiers have used 3D PIC simulations to study accurate gain calculations [112] [113] [114] [115] [67] [116], and stability to higher-order mode oscillations [117]. MAGIC3D is a commercial simulation tool that has been used in many of these studies. We use it here to study gain estimates, and in the subsequent chapter for stability analyses.

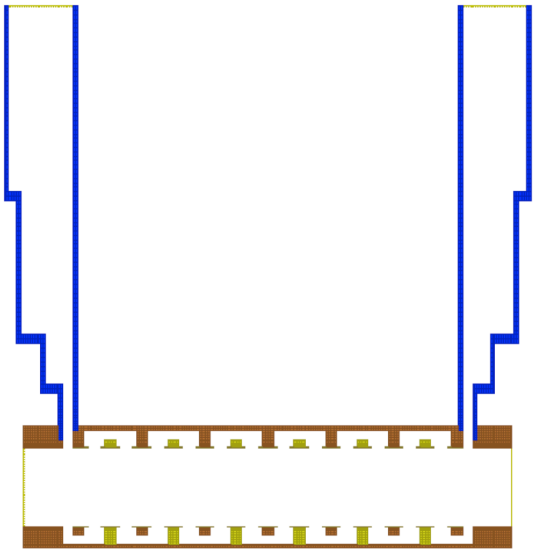

Figure 3.5: Geometry of sheet-beam SWS with waveguide inputs – cross-section along beam tunnel.

We begin the 3D simulations by looking at the electromagnetic response and transmission characteristics of the slow-wave structure with waveguide couplers as a comparison to previous 3D electromagnetic simulations with finite element software. We drive the simulations with a specified drive power, P_{drive}, and a specified drive frequency, f_{drive}, at the input port, where the initial fields are zero, and the input signal is ramped up over 15 RF cycles. The simulation runs for a few hundred cycles until a steady state is achieved at all ports. The magnitude of the reflection coefficient at the input port is calculated by observing the power at each port and solving for $|\Gamma_{in}|$ in the following:

$$P_{out} = P_{drive}(1 - |\Gamma_{in}|^2) \tag{3.5}$$

in linear units, or

$$P_{out}[\mathrm{dBm}] = P_{drive}[\mathrm{dBm}] + |\Gamma_{in}|[\mathrm{dB}] \tag{3.6}$$

in logarithmic units.

The RF return loss as a function of frequency for the structure is reported in Figure 3.6, in comparison with the simulation of an identical structure geometry in the finite element software, HFSS. The differences in the response can likely be attributed to the mesh resolution

in the MAGIC simulation and overall simulation accuracy in both simulations. This is a moderately well matched coupler design by the methodology of the preceding chapter, and the slow-wave structure is different from previous, so as to obtain a stable device. Specifically, this geometry will be discussed presently in our discussion of gain studies with a 3D PIC simulation, without yet discussing instabilities and oscillations.

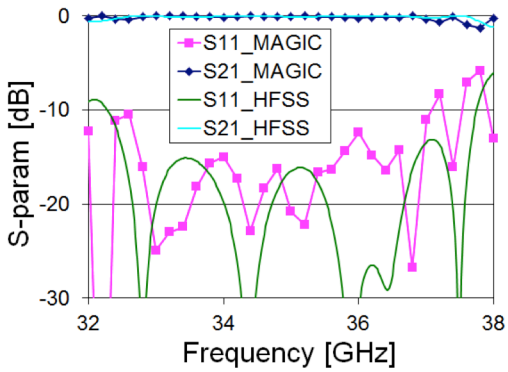

Figure 3.6: Simulated scattering-matrix parameters evaluated with MAGIC and HFSS.

For the following particle simulations we refer to the set of parameters from Table 3-II for a slow-wave structure that has a center frequency at 35 GHz, and operates with an electron beam at 19.5 kV and 3.5 A of rectangular cross-section 4 mm x 0.3 mm. This structure does not utilize a rectangular ferrule (or nose) around the rectangular beam-tunnel. We performed a full gain analysis of the structure in Table 3-II with a suite of simulation analyses, and the following presents representative data of that analysis. The simulated geometry with 18 cavities is illustrated in Figure 3.7 including a simulated sheet electron beam for reference.

Results of a set of simulations for a short 14-cavity section are presented in Figure 3.8, where the drive frequency was varied across the bandwidth of the device at constant drive power (P_{Drive} = 200 W = 53 dBm). The drive frequency is adjusted in the input-file for each separate simulation, and the results are obtained from the steady-state portion of the output-files. The RF power is calculated at both waveguide ports by integrating the instantaneous Poynting flux over the WG port surface area, therefore the input port power is a combination of the drive power and any reflected power from the structure. The gain is calculated as the ratio of the output power

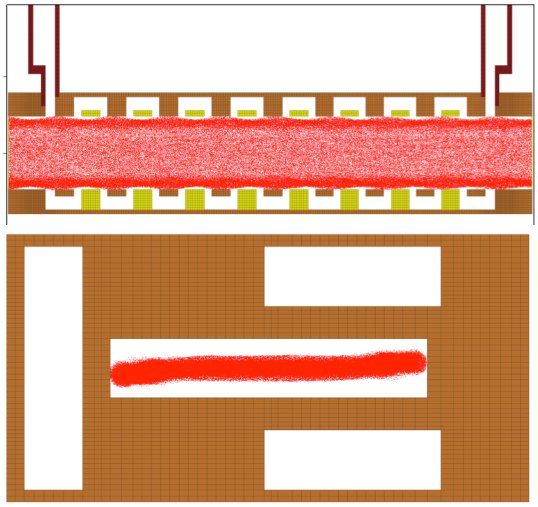

Figure 3.7: Geometry of sheet-beam SWS with waveguide inputs and electron beam traveling through the beam tunnel. a) cross-section along beam tunnel. b) cross-section through septum and coupling slots.

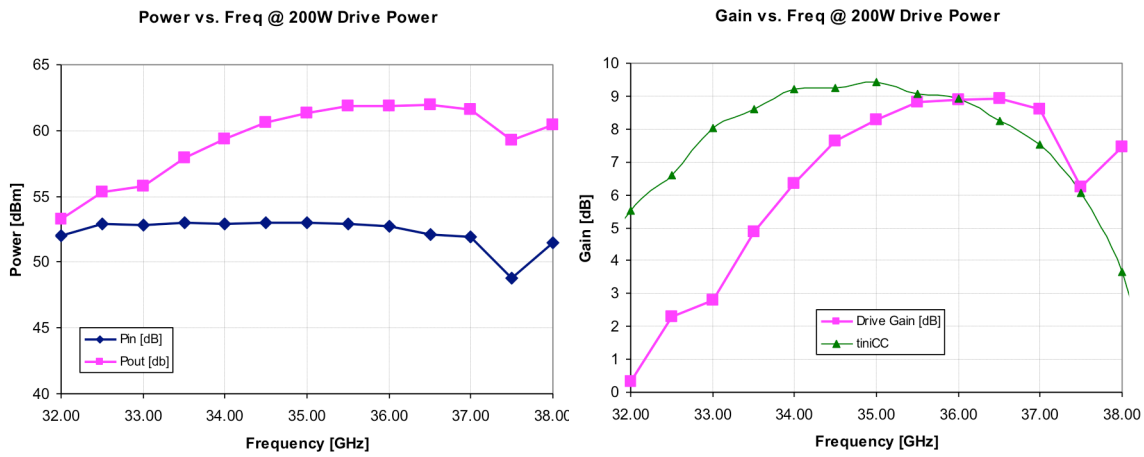

Figure 3.8: Bandwidth plots for a 14 cavity structure with a 200 W drive power. a) RF Power measured at each waveguide port vs. Frequency. b) RF Gain vs. Frequency – comparison between MAGIC and CHRISTINE-CC.

magnitude to the drive power. We see that for such a short section of slow-wave structure that there is little gain (only 9 dB at maximum). Also, the CHRISTINE-CC estimated gain is provided as a comparison. In this comparison the magnitude is similar, but the shape is off – this might suggest that the end effects are somehow affecting the simulation. Some later comparisons are much closer.

Further simulation results are presented in Figure 3.9, where the drive power was varied over a reasonable input range of the device at constant drive frequency (three drive frequencies are included in the plots). The drive power is adjusted in the input-file for each separate simulation, and the results are obtained from the steady-state portion of the output-files. The 200 W (53 dBm) drive power value is in the middle of the range and is in the mostly linear gain region – it is certainly not saturated with the nominal drive power.

In the preceding particle simulations, the electron beam that was used was a beam created through a standard uniform current density emission definition within MAGIC3D. This uniform current density definition produces a beam with velocity perpendicular to the emission surface with nominally 19.5 kV electron macro-particles (with a 2D space-charge depression algorithm applied on the input port) and a total current of 3.5 A uniformly distributed over the rectangular region of emission surface mesh. Hence, the nominally singular electron voltage and the singularly defined emission direction produces a fundamentally overly-simplistic electron beam in comparison to the thermal electron beam produced by a realistic thermionic cathode with a

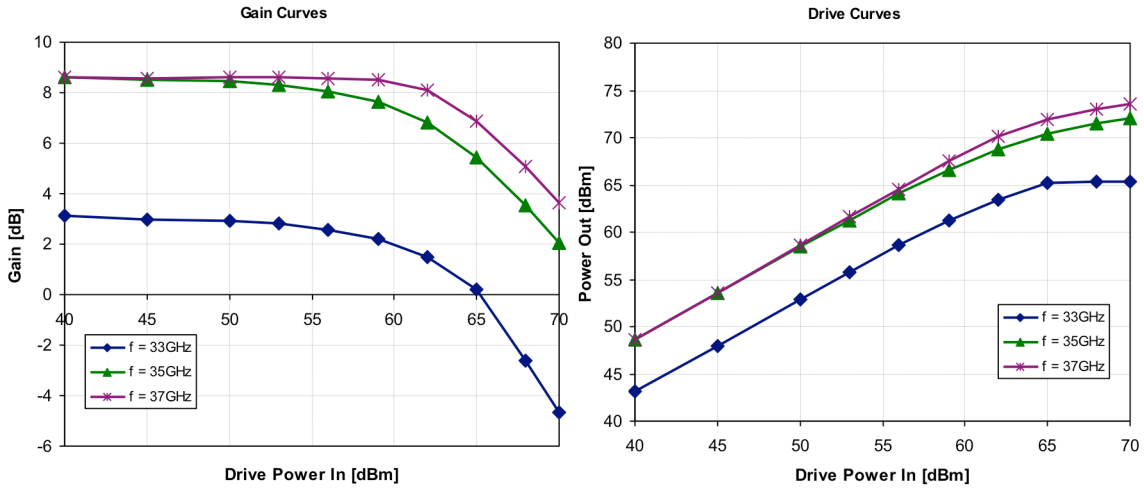

Figure 3.9: Drive curves for a 14 cavity structure. a) RF gain vs. drive power at different frequencies. b) RF output power vs. drive power at different frequencies.

thermal spread of electron energies and emission angles. To provide a more realistic numerical electron beam, we simulated the electron beam produced by the electron gun with a 3D electrostatic gun simulation using the MICHELLE software [118], and utilized thermal emission characteristics starting at the cathode. The MICHELLE thermal beam produces a beam with nominally 19.5 kV electrons and a total of 3.5 A current in the beam. The particle data is exported from MICHELLE into a data table that MAGIC3D can import and apply directly to the desired emission surface. When the uniform beam definition without thermal particles is used, we refer to this case as a *cold-beam* – whereas, when the electron beam has thermal velocity spreads appropriate for a beam originating from a thermionic cathode with appropriate focusing and compression, the beam is referred to as a *hot-beam*.

In comparison to the cold-beam results obtained above, in Figure 3.10 we present hot-beam results for the same device geometry as the cold-beam results above. The solid curves have identical geometry (in particular, the beam-tunnel height is the same 0.035" tall), while the dashed lines are results for a smaller beam-tunnel height (0.0325" tall) producing a stronger interaction. The gain and power vs. frequency plots are the same shape as above, but the solid curves are reduced gain – due only to the thermal velocity and nonuniform beam distribution. In order to compensate for the reduced interaction, we reduced the beam-tunnel height and compensated appropriately for the gain as seen in the results. The CHRISTINE-CC results are provided again as a comparison for the gain, and the same dissimilarity in shape persists.

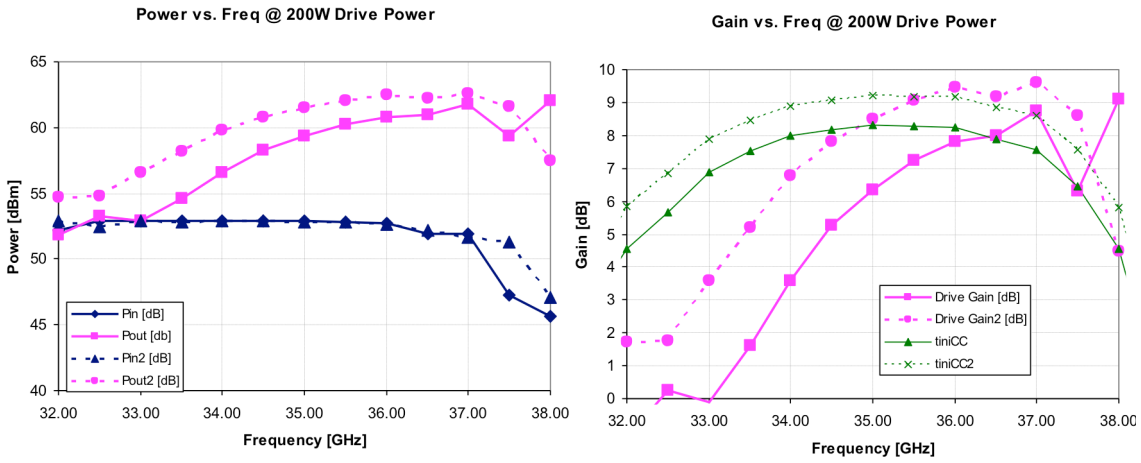

Figure 3.10: Bandwidth plots for a 14 cavity structure with a 200 W drive power and a hot-beam. a) RF power measured at each waveguide port vs. Frequency. b) RF gain vs. frequency – comparison between MAGIC and CHRISTINE-CC.

In Figure 3.11 we present a comparison of a drive-curve with the same geometry but different beams in order to investigate effects of particle sampling on the device characteristics. The plot shows a few points on the drive curve vs. drive power in order to establish consistent magnitude of the response. The highest curve on the plot represents the output power for the cold-beam case, while all four of the lower curves are various samplings of the thermal beam. Sampling is required for the thermal beams to keep the particle count reasonable, and a renormalization of the sampled particles produces the required current. The sampling varies from ~1-10%, yielding particle counts from ~27000-265000 in the input region for the hot-beams, compared to the cold-beam with ~65000 particles. Because the results are similar for the various samplings, we establish that any of these samplings is sufficient to correctly resolve the amplifier dynamics. For the remainder of the hot-beam tests we use an intermediate sampling of those tested here.

These 3D particle simulations have proven to be necessary for confirmation of gain estimates and for investigating instabilities, which is examined in the following chapter. Further examples of gain calculations are provided in the final chapter with the proposed device geometry.

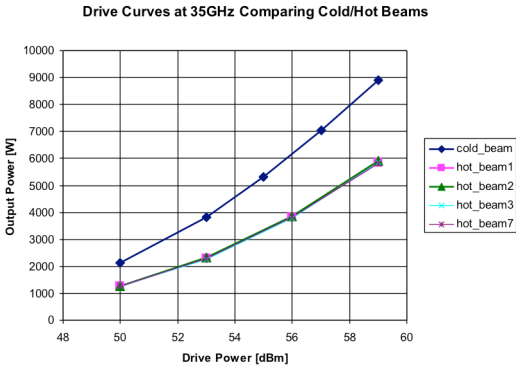

Figure 3.11: Comparison of various beam sampling and hot-beam vs. cold-beam results.

Chapter 4: Sheet-Beam Stability Analysis

Stability is an issue that must be addressed in all high-power and high-gain tubes, but is of particular concern in a sheet-beam structure where the mode density is increased and multiple modes can couple and interact causing undesired effects. Sheet-beam coupled-cavity slow-wave structures are inherently three-dimensional with complicated electric fields and overmoded dispersion. In order to analyze the stability of a sheet-beam SWS, we must account for the non-uniform fields and complex dispersion in order to estimate the interactions of the SWS modes with a realistic sheet electron beam. Throughout the design of the sheet-beam coupled-cavity amplifier, we account for several common sources of oscillations in conventional high-power coupled-cavity amplifiers as well as concerns raised due to the elongated sheet-beam structure.

Instabilities tend to occur at specific frequencies that can be traced to specific behavior of the dispersion diagram – specifically, oscillations will most likely occur at band edges, mode crossings, and at backward wave intersections of the beam-line with the dispersive modes. Instabilities may also be observed at resonances of the electron gun or collector cavity, due to back-streaming electrons, or a PPM cyclotron resonance – however, these instabilities are separate from the beam-structure interaction and will not be considered here. The fields and behaviors of the considered instabilities are all different, and will be catalogued through the course of this chapter. Once catalogued, we can discuss the causes of these instabilities and investigate techniques to mitigate their onset. In this chapter, we do not use the parameters of the proposed device, but explore the properties of the structure through several variations of geometry – the simulated results of the proposed device are presented in Chapter 5.

4a) Conventional High-Power Amplifier Instabilities

Instabilities have been documented as a cause of undesired behavior in many conventional single-beam, round-beam, high-power coupled-cavity amplifiers [4] [119] [120] [104] [121] [122] with similar analyses for other linear beam amplifiers (*e.g.* helix traveling wave tube [123], [124], [125], klystron amplifiers [126]), and gyro devices (*e.g.* gyroTWT [127], [128] [129] [130])). For traveling wave devices, the predominant mechanism for instabilities is regenerative oscillation, where the amplified signal experiences a feedback due to internal or external reflections, and the regeneratively amplified signal increases with each reflection until saturation is reached or

some other nonlinear mechanism takes over. These regenerative oscillations tend to be near the band-edges due to increased gain and high reflections at the passband edges. Instabilities are particularly troublesome for devices with broad bandwidth interaction and high-gain and/or high-power, because the band-edges experience a stronger interaction in all these cases.

The dispersion diagram pictured in Figure 4.1 represents an example dispersion curve of a conventional round-beam CC-SWS operating in the first harmonic. The electron beam is synchronous with the forward-wave of the fundamental mode over some region of phase between π and 2π. In a pillbox-like cavity this lowest, fundamental mode has fields that are similarly shaped to a pillbox TM_{010} mode, therefore called the "cavity mode". The next highest mode (separated in frequency by a stopband and with opposite group velocity) has somewhat similarly shaped fields but is affected more by the coupling slots, and is therefore called the "slot mode". The dispersion diagram is particularly useful for identifying points of intersection for the SWS modes and the electron beam-line (points of synchronicity where the electron beam interacts most strongly with the slow-wave structure). When the intersection is at a point of positive group velocity, the interaction is generally an amplification of a forward propagating wave, which would only have instability due to reflections and regenerative amplification. When the intersection is at a point of negative group velocity, the interaction is a backward-wave amplification, which can grow via a similar regenerative amplification under some circumstances, or can grow spontaneously when the interaction is strong enough [131]. When the interaction is near a zero-group velocity point (a band-edge, or otherwise local extrema), the interaction can behave strongly and does not require reflections to produce oscillations. All of these cases of intersection/interaction are of concern for both conventional high-power and sheet-beam amplifier devices.

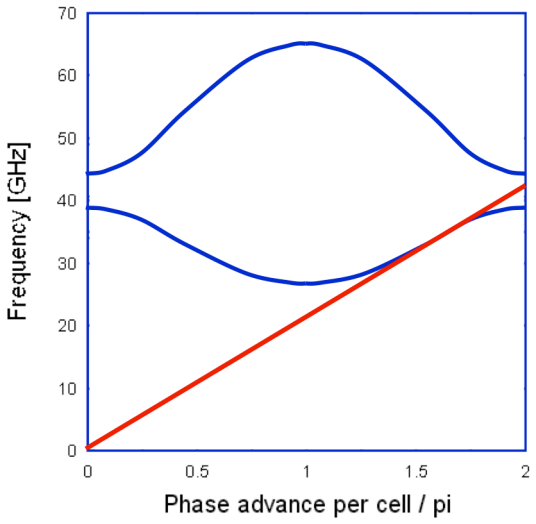

Figure 4.1: Example dispersion curve for a conventional round-beam CCSWS operating in the first harmonic.

As discussed in the section on linear gain, the forward wave interaction is determined, as a function of frequency, predominantly by the following points: 1) the relative strength of interaction for the structure, 2) the beam parameters, and 3) the relative synchronization of the beam and wave velocities. The first two points are often combined into a single (frequency dependent) parameter called the Pierce gain parameter, C_{Pierce}. As C_{Pierce} increases the interaction across the entire range of modes increases, the interaction effect with asynchronous modes increases due to a stronger coupling of the electron beam and the electromagnetic mode, therefore the interaction becomes more broadband, and most asynchronous oscillations increase their likelihood of spontaneously growing. Alternatively, as the SWS bandwidth increases, the coupling between the beam and the fundamental-mode band-edges inherently increases due to a more synchronous phase-velocity across the entire bandwidth of the structure. These are the dominant reasons why high-gain, broadband devices require special methods of suppressing oscillations [120] [4]. Further complications arise if the beam current is increased by increasing the beam cross-section, because undesired modes tend to interact more strongly off-axis – therefore, in most forward-wave traveling-wave amplifiers a smaller ratio must be maintained between the beam height and the beam-tunnel height [2].

High-gain devices are prone to oscillations even within the middle of the fundamental passband under certain conditions. If the gain of the device is larger than the combined effect of round-trip attenuation and reflections at the input and output, then a signal near the synchronous interaction of the beam will form an unstable feedback loop and will oscillate. In practice, the reflections at the input and output can only be controlled to a limit, and in-band attenuation is often undesirable, so the conventional limit from a single-section device is roughly 20 dB [4]. In order to achieve further stable amplification, the standard method is to use a *circuit sever* (a localized, matched circuit termination that separates the circuit into sections) to prevent the high-gain signal from being reflected to the input, yet allowing transmission and further amplification of the RF signal on the beam. The dynamics of the sever are outside the scope of this thesis and have been well documented elsewhere [1] [4] [95]. For an overmoded structure such as a sheet-beam, the sever would need to present a broadband match to all modes supported by the structure – this will be discussed in the section on sheet-beam instabilities, but will be avoided in the final design by limiting the length and gain of the device to a single section. Few high-power tubes have only a single section because that would require a moderately high-power driver tube, but single-section tubes are often used in helix MPM's as

power boosters [132] and have been used in some broadband high-power coupled-cavity power boosters as well [18].

Although the in-band oscillations can be managed by reasonably well-matched couplers and limited gain per section, for high-power, broadband devices the biggest danger comes from band-edge oscillations [4] [119] [120] [122] [133]. This can be simply thought of as a regenerative oscillation that occurs for frequencies near the upper or lower frequency of the structure pass-bands, and therefore with the increased interaction impedance and reflections that are associated with the band-edges. However, the total interaction can be much higher due to the inherent interaction of forward and backward waves that produces an increased feedback and interaction mechanism near the band-edge [121] [134]. For most high-power devices this is a major concern for self-oscillation and drive-induced oscillation at the upper band-edge of the fundamental passband.

All of these instabilities are of concern for both conventional amplifiers and sheet-beam amplifiers. The key characteristics of distributed-beam amplifiers are high-current, high-gain per cavity, and broad bandwidth, all of which increase the likelihood of oscillation.

4b) Driven vs. Non-Driven Instabilities

The two major classifications of instability are driven vs. non-driven. A driven instability (or drive-induced oscillation) is some oscillation behavior that occurs only for some (usually large) drive signal, but does not generally occur when the drive signal is small or nonexistent, and is generally a nonlinear, multi-frequency phenomenon. A non-driven instability (also called a self-oscillation) is an oscillation that occurs with no drive signal present, and arises as a regenerative amplification or absolute instability of the thermal noise in the system. Almost any of the separately classified oscillations can be due to either driven or non-driven causes, and therefore this distinction is made separately.

Self-oscillation generally arises from a regenerative amplifier or absolute instability type oscillation. Regenerative amplifier refers to a situation where a fraction of the amplified signal (thermal noise to begin with) is partially coupled back to the input through some feedback mechanism, and the gain is strong enough to overcome attenuation and coupling losses. This type of amplification occurs for frequencies with strong interaction, and such that the phase of the reflected wave allows constructive wave interference. An absolute instability is a point of

particularly strong beam-wave interaction with zero group velocity (*e.g.* a band edge frequency), such that the growth is not through a convective amplification but uncontrolled growth of the undesired frequency at each point along the beam. The distinctions between the different kinds of self-oscillation are usually mostly of degree, and it is undesired for any degree to be present, so they all must be accounted for.

Drive-induced oscillations occur for certain types of instability more than others – most commonly 2π band-edge oscillations and backward-wave oscillations. There have been several reasons proposed for why a strong drive-signal would induce instabilities or lower the threshold for oscillations. First, the energy spread of the electron beam increases for strong signals, allowing undesired interaction of the beam with band-edges and regions of otherwise strong interaction. Second, beam-expansion generally increases with drive signal as the beam-bunches create stronger electric repulsion forces, allowing increased interaction of the beam with undesired (off-axis) modes. Third, coupling of the undesired mode to the strongly driven mode can occur through a mode-coupling mechanism mediated by the electron beam. All three of these reasons likely contribute to the appearance of an oscillation, and the oscillating mechanism is generally similar to the self-oscillation cases described above, but generally with a reduced oscillation threshold. However, there are instances where a strong drive signal will improve the stability of a structure, and a spurious self-oscillation will be overcome by a powerful drive signal. This is a complicated nonlinear process that demands careful investigation in all circumstances.

A special-case of this distinction between drive-induced and self-oscillation is a power-hole occurring at a frequency of some self-oscillation. A power hole is only defined in cases of a drive signal with some finite power and some reasonable frequency bandwidth, but the power-hole may appear for large or quite small drive signal, and not quite the same manner as a large drive-power induced oscillation. A power-hole occurs due to direct coupling of the drive-frequency to some resonant oscillation, often due to resonances in the beam or transport, but possibly a coupling to other modes supported by the structure. Generally the frequency of the driven mode and the coupled mode would need to be commensurate, but could conceivably be a coupling of a drive harmonic to a strongly interacting mode at a frequency the multiple of the drive signal, but coupling harmonics would require a strong drive signal. The dynamics of this

behavior are represented by a direct coupling of power from the fundamental mode into the undesired, coupled mode where the power is dissipated or causes beam break-up.

4c) Sheet-Beam Amplifier Instabilities

A sheet beam amplifier has numerous complications that increase the likelihood of oscillation due to a number of different instabilities. The sheet-beam slow-wave structure is inherently overmoded with an increased mode-density, due to the expanded transverse dimensions of the beam-tunnel and rectangular cavity. Also, the decreased beam impedance of the sheet-beam creates a stronger interaction with all modes supported by the slow-wave structure. The various instabilities of concern will be presented and discussed with examples.

A representative dispersion diagram for the 3-slot sheet-beam CCSWS is illustrated in Figure 4.2. Several of the complications of this dispersion diagram were discussed in Chapter 2, where both the symmetric and antisymmetric modes, and the intrinsic band-gap at 1.75π were investigated. The illustrative complications in this example sheet-beam SWS are characteristic of the possible sheet-beam amplifier instabilities that cause concern.

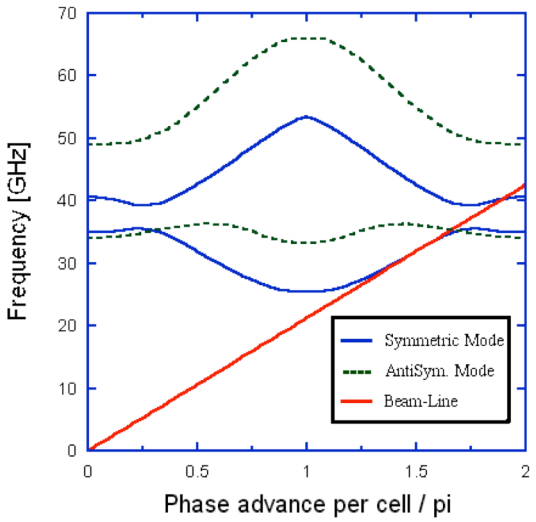

Figure 4.2: Example dispersion curve for the 3-slot sheet-beam CCSWS operating in the first harmonic.

The transverse modes (the green, dashed lines in the figure) are at a frequency comparable to a half-wavelength supported by the beam-tunnel length [23]. These modes can cause oscillation through either a backward-wave oscillation or a band-edge oscillation when the modes are coupled through beam-tunnel offsets. We investigate the interaction of transverse modes using 3D particle simulations (results found in Section 4g) because the 1D theory is designed for longitudinal interaction with the fundamental mode only. We have found that these oscillations do not arise in non-driven conditions, and only appear as power holes near the frequency of the backward-wave intersection or band-edge. The transverse nature of the oscillation was identified through particle and momenta plots along the length of the interaction, and by the appearance only

under beam-tunnel offset – never did a transverse oscillation occur for a perfectly aligned structure. It may be the case that for longer structures with insufficient severs, that a self-excitation of these oscillations would exist (*i.e.* oscillation without a drive signal).

The transverse mode is not strongly coupled by design, but can be unintentionally excited by alignment errors in several locations. Without the electron beam, the transverse mode is not excited if the beam-tunnel is perfectly aligned within the short dimension of the rectangular cavity because the couplers are oriented such that the electric field is symmetrically excited within the cavities. However, as the offset of the beam-tunnel increases, so too does the unintentional excitation of the transverse mode. This offset can occur as any asymmetry in the input cavity, or any cavity within the structure, although the most important parameters are those affecting the symmetry/asymmetry of the electric field near the beam-tunnel (*i.e.* beam-tunnel offset, or uneven capacitor post height). With the electron beam present the coupling to the transverse mode increases if the beam is offset in the short dimension because the transverse mode only has longitudinal fields off-axis (there are zero longitudinal fields on-axis in the aligned geometry, and the transverse fields are relatively uniform in the short dimension). These off-axis longitudinal fields will interact strongly with the bunched electron beam and support oscillations. It is the combination of these affects that leads to the excitation of the transverse mode oscillations through unintentional misalignments.

The band gap in the symmetric mode is indicative of the rectangular cavity, which reduces the frequency of the second cavity resonance. In our effort to maintain the broad bandwidth of the SWS, the second cavity mode (the conventional "slot-mode") crosses with the fundamental mode (the conventional "cavity-mode"), however, according to [135] the dispersions of similar modes cannot cross in a trivial way without having a specific higher symmetry, which is not the case for this particular crossing). This complicated dispersion is typical of the increased mode density of a sheet-beam SWS – not only are there more modes within the general frequency range of interest, but these modes will have additional band-edges and otherwise reduced group-velocity regions unless carefully controlled. Another complication of the increased mode density, is that this makes frequency selective attenuation techniques more difficult (if not impossible), because the undesired, oscillatory frequency may exist closer to (or within) the desired frequency range such that the attenuation may affect the operating mode.

A further point that does not appear in the plot of dispersion is that sheet-beam structures generally have complicated fields. Within the beam-tunnel region the fields are relatively smooth and will be studied in terms of the transverse profiles of the interaction impedance. In a SWS with only conductive losses, the complication of the fields in the exterior of the beam-tunnel is not of overly general concern because the fields and dispersion can be obtained through numerical simulation, and the only interaction outside the beam-tunnel region is between the electromagnetic wave and the conductive surfaces. However, it is sometimes harder to apply a mode-selective attenuation in such a place that will attenuate higher modes and not affect the desired mode – the increase in difficulty is partially related to the increased mode density discussed above. It is generally more difficult to selectively attenuate a higher mode without affecting the lowest mode than to selectively attenuate the fundamental in preference to a higher mode because the lowest mode generally has no extra field nulls in which to place lossy absorbers. Nevertheless, the fields can be separated into symmetric and antisymmetric modes which have very different field distributions and current densities. Therefore a scheme could be applied to preferentially attenuate the antisymmetric modes either in a distributed manner or at a discrete sever location.

A final complication that we discuss here is that if multiple sections of gain are used in the amplifier design, a sever must be utilized that will substantially absorb and suppress all modes that are supported by the structure and which may interact with the electron beam. Again, this may be accomplished by dividing the modes into symmetric and antisymmetric classes. The symmetric modes are nominally terminated at the sever in the conventional manner – either internally by removing the coupling slots and applying lossy dielectrics, or externally by coupling the SWS into a matched broadband load. However, the antisymmetric modes exist predominantly within the beam-tunnel region, and would neither be well-coupled to an external load, nor likely to internally loading dielectrics. It may be that a distributed loss that suppresses the antisymmetric mode along the length of the circuit is necessary for longer devices with higher gain.

4d) Backward Wave Analysis

There have been many analyses of backward wave interactions and the thresholds for oscillation in a given structure. The most standard analysis finds a threshold above which the device will oscillate even when no reflections are created by mismatched terminations or severs, but only

by the natural feedback that occurs with the combination of forward and backward waves. The most classic backward wave oscillation analysis by Johnson [131] evaluates the current threshold required for oscillation as a function of length of the structure and provides a Pierce-like 1D transmission-line model for the interaction. Variations on this analysis have been developed using field solutions or otherwise for various kinds of linear beam device [131] [136] (or gyro-device [137]). The model we use is similar to the standard Johnson model with the interaction calculated using beam averaged values for the synchronous electric field components [123].

Specifically, we use the same 1D transmission-line interaction assumptions as in the 1D gain analysis, but in the calculation of forward and backward wave interaction, we average the Pierce impedance using the appropriate synchronous spatial harmonic of the backward wave over the beam cross-sectional area. We find that in comparison to the nearly uniform interaction of the forward-wave with the electron beam, the fundamental backward-wave has a linearly varying interaction with the height of the beam, with zero interaction on-axis. This is only marginally different than the calculation in a cylindrical beam, where the linear variation in backward wave interaction is radial with a single azimuthal variation. However, higher-order modes of the sheet-beam structure have much more complicated field profiles and the beam-averaged interaction impedance values are calculated numerically from simulated field solutions, and these higher modes are at reduced frequency (increased mode-density) causing an increased interaction and increasing the difficulty of selective suppression.

The 1D model used here assumes no reflections and no loss – the oscillation threshold is analytically derived as the necessary conditions for the backward wave to spontaneously grow from zero amplitude at the output of the device to a finite value at the input (which due to the inherent feedback of the backward wave will grow until saturation). Generally this oscillation threshold is presented as the *start oscillation current* for a given device and given beam voltage, however in the design of our device we assume a beam voltage and current, and allow the axial length to change for a given uniform structure, thus providing a threshold length for BWO stability. The simple model for backward wave growth is calculated using the following formulas:

$$Q_{Pierce} = \frac{\omega_{p,eff}^{\ 2}}{4\omega^2 C_{Pierce}^{\ 3}} \tag{4.1}$$

$$\omega_{p,eff}^{\ 2} = \frac{\eta I_0 R_n}{\varepsilon_0 A_{Beam} v_{z0} \gamma^3} \tag{4.2}$$

where $\omega_{p,eff}$ is an effective, angular plasma frequency, R_n is a reduction constant (assumed equal to 0.5 for this simple model), A_{Beam} is the beam area, η is the electron charge-to-mass ratio, v_{z0} is the beam velocity and γ is the relativistic Lorentz factor.

As a preliminary example, for the original structure characterized in Chapter 2, we use a beam-averaged Pierce Impedance appropriate for the backward wave mode (Z_{Pierce} = 0.282 Ω) and beam parameters as previously, producing the result that Q_{Pierce} = 124. Then, using the tables in [131] we find $C_{Pierce}N$ = 0.6 for our value of $Q_{Pierce}C_{Pierce}$. This yields a maximum length of 63 mm, which is twice the length of the short section used in the forward wave analysis of that section.

It has been found that for reasonable ratio of beam height to beam-tunnel height, that the backward wave component (n = -1 spatial harmonic) of the fundamental mode has a small enough interaction to keep the spontaneous excitation below the threshold value. However, the backward wave interaction can couple to a reflected forward-wave, allowing for a self-regenerating oscillation – this is particularly dangerous at the 1.5π-intersection of the forward and backward waves, where the forward and backward waves have the same frequency and wavenumber and are nearly in synchronism with the electron beam. Providing further concern for biperiodic structures is the case of an asymmetry that might couple the modes and create a bandgap at 1.5π, thereby increasing the beam-wave interaction at that point [123] [138] [139]. Further implications of this backward-wave mode have been found (power holes, gain ripple) [123] and investigated in terms of the device simulations.

Of greater importance than the simplistic spontaneous BWO analysis provided here, is the understanding of the backward wave interaction for similar analysis of dangerous band-edge oscillations and higher-order mode interaction. Using a 1D interaction theory, the interaction with the backward wave of the fundamental mode is identical to the backward-wave interaction with higher modes, except the fields are more complicated and the frequency is somewhat higher (meaning the interaction is generally lower). Non-driven band-edge oscillations are of

major concern for a coupled-cavity device with large gain per cavity, and are qualitatively similar to backward-wave oscillations with large reflections and larger interaction. Most intersections of the beam-line with higher-order modes occur at backward wave intersections or near band-edges due to the slope of the beam-line. These various intersections will be investigated in the following for our example sheet-beam structure.

4e) Higher-Order Mode Analysis

The term *higher-order mode* is loosely applied to all modes supported by the SWS other than the fundamental mode. The implication is that these modes exist at some higher frequency range, and in the design of our amplifier device, these are considered undesired modes that may lead to oscillations under some circumstances. The dispersion diagram in Figure 4.3 is a close-up of the eight lowest modes obtained in eigenmode simulations of the 3-slot sheet-beam CCSWS with parameters in Table 3-II. The intersections of the beam-line (the dashed line in the dispersion plot) with the various modes represent possible interactions that will be investigated in the following.

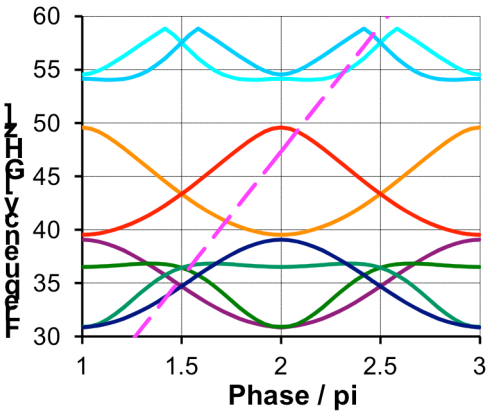

Figure 4.3: Close-up dispersion curves for all modes of the SWS with parameters in Table 3-II.

Higher order modes are a concern for conventional high-power devices, although instability is less common than band-edge oscillations [4] [119] [120]. There are several reasons why the fields in higher-order modes interact less in the case of round-beam devices yet are potentially of concern in a sheet-beam device. First, the fields of the higher mode fall off rapidly from the walls of the beam tunnel, which is conventionally accounted for by limiting the beam radius to beam-tunnel radius ratio; however, for a sheet-beam device, even though the beam height to beam-tunnel height ratio might be small, the beam-width is generally a sizeable fraction of the beam-tunnel width, which could increase interaction with some modes. Second, in conventional structures the frequency and wavenumber at the point of intersection are significantly larger for the higher-order mode than for the fundamental interaction, which conspire to decrease the interaction strength; however, for a sheet-beam SWS, the increased mode density reduces both the frequency and wavenumber of several higher-order mode

intersection points in relation to the fundamental interaction, increasing the relative interaction strength. Third, due to the increased mode density of sheet-beam SWSs, additional band-edges may appear that interact strongly with the electron beam.

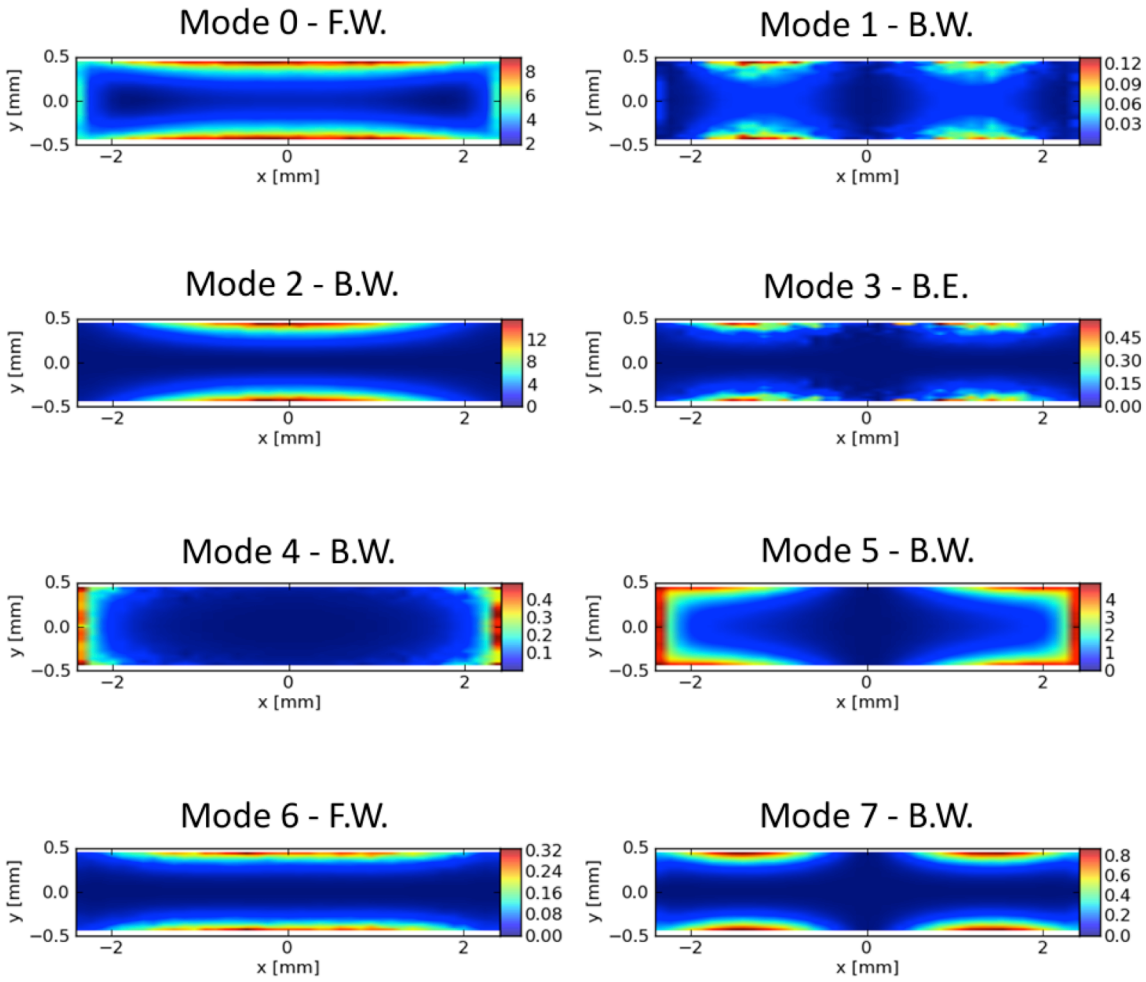

Figure 4.4: Interaction impedance vs. position plotted over the transverse cross-sections of the beam-tunnel, for each mode intersection in Figure 4.3. Designators: **F.W.** – Forward Wave, **B.W.** – Backward Wave, **B.E.** – Band Edge.

In order to investigate the interaction of the electron beam with the fields of the structure, we numerically evaluate the interaction impedance across the transverse cross-section of the beam-tunnel area for each intersection of the beam-line and dispersion curves in Figure 4.3. A set of contour plots representing the transverse positional-dependence of the interaction impedance calculated over the cross-section of the beam-tunnel is shown in Figure 4.4. For reference, the beam height to beam-tunnel height ratio is approximately 50%, and the width

ratio is about 80%. These impedance profiles have the following significance for interaction: Mode 0 is the only mode that has a strong non-zero impedance on-axis and is mostly uniform across the beam cross-section. Mode 1 is a backward wave intersection with zero impedance on-axis and little interaction across the beam. Mode 2 is an antisymmetric mode backward wave intersection, with very little interaction for the aligned beam-tunnel case. Mode 3 is the second antisymmetric mode intersection with even less interaction, but the intersection is close to a band-edge so the interaction will be much stronger. Mode 4 is a symmetric mode backward wave intersection with non-zero impedance on-axis, but very small magnitude across the beam cross-section. Mode 5 is another symmetric mode backward wave intersection with nearly zero impedance on-axis (due to the biperiodicity), but the off-axis impedance ramps up quickly in the wide direction, and is intensified due to the proximity of the upper band-edge, and is therefore of concern. Modes 6 and 7 are antisymmetric modes with weak-to-moderate interaction.

In order to quantify the interactions and compare their relative strengths, we develop a table of the expected linear amplification of the structure (forward wave intersection) and the threshold oscillation length (backward wave and band-edge intersection) for a given beam voltage and current. The interaction impedance is averaged over the beam cross-section and applied to the linear gain or BWO theory already developed. The results are provided in Table 4-I, assuming an axial length of 12 cavities (0.77") for the forward gain calculations (negative gain means that the bunching process has not succeeded in amplifying the signal). This table suggests that the band-edge intersection does not have a strong interaction (which fortunately is true), and that if the circuit were made longer (*e.g.* to produce more gain) that the most susceptible mode to

Mode #	Type	Phase [deg]	Freq [GHz]	Z_{Pierce} [ohms]	Gain [dB]	$L_{threshold}$ [in]
0	FW	1.497	34.686	2.166	10.0	----
1	BW	1.497	34.761	0.018	----	5.90
2	BW	1.563	36.144	0.191	----	2.49
3	BE	1.583	36.875	0.007	----	7.50
4	BW	1.750	40.557	0.022	----	4.69
5	BW	2.125	49.074	0.287	----	1.45
6	FW	2.375	55.570	0.003	-6.2	----
7	BW	2.458	58.464	0.007	----	4.79

Table 4-I: Table of interaction strength (forward gain or BWO threshold length) for each mode intersection in Figure 4.3.

oscillation is the backward wave intersection of Mode 5 (which unfortunately is also true). The stability of this slow-wave structure was confirmed with 3D particle simulations for several lengths of uniform structure (until oscillation occurred). Further information on particle simulations can be found in Section 4g.

4f) CHRISTINE-CC Pi and 2Pi Analysis

CHRISTINE-CC was used in the analysis of small- and large-signal gain for the coupled-cavity structures investigated here. The limitation with CHRISTINE-CC is that, although it is a multi-frequency simulation code, it only responds to the set of frequencies prescribed to the simulation – it does not predict oscillation frequencies in a manner that a time-domain simulation might naturally exhibit an inherent oscillation. However, below the onset of oscillation, the CHRISTINE-CC simulation should well predict the performance of the amplifier, and nearly up to the threshold of oscillation the simulation should predict the gain characteristics. Furthermore, the fast simulation times of the parametric design codes allow many variations and a full search of the possible parameter space. We use several analyses of CHRISTINE-CC to predict instabilities within the fundamental mode and at band-edges.

It was mentioned in the small-signal analysis of the structure, that if the Pierce gain parameter, C_{Pierce}, increases then the gain ripple increases and the gain fluctuates wildly. We explore that further with a fixed structure (SWS parameters, and fixed length), by adjusting the beam voltage and current. By performing a few frequency sweeps with several values of beam current (see Figure 4.5), we see that for large currents the solution again fluctuates wildly and, in this case, the gain increases towards the band edges. The increased interaction created by the increased current alone creates this large ripple, a generally increased interaction across the bandwidth, and an uncontrolled increase in interaction near the band-edges – all of these were suggested in stability considerations and are confirmed here.

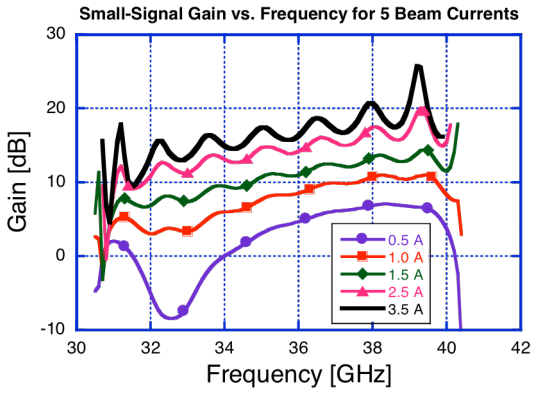

Figure 4.5: Small-signal gain vs. frequency for 5 values of beam current – simulation results from CHRISTINE-CC for a structure very similar to that from Chapter 3.

Furthermore, what we find in the simulation is that for some values of beam current and

frequency, the solution does not converge to a solution in its iterative solution process. This non-convergence does not necessarily imply instability, but we would expect that for regions of physically stable amplification that the simulation would correctly predict the amplifier gain. We can avoid the complications of rationalizing the significance of converged vs. unconverged solutions by noticing that the unconverged solutions generally occur at the peaks of gain ripples near the band-edges, and then suggesting that the amplification at the band-edges should be below some threshold gain to avoid instabilities – therefore, we can pick a reasonable gain threshold below the threshold of unconvergencea and suggest that the gain is required to remain below this value at the band-edges.

To investigate the beam voltage and current stability margins more carefully, we perform a fine-tuned sweep of voltage and current at a single frequency near the π-point, and again at another frequency near the 2π-point. The results of this variation are shown in Figure 4.6 as contour maps of the gain vs. beam voltage (abscissa) and beam current (ordinate). The absolute magnitudes of the gain contours have been omitted – only retaining the general shape of contours and the threshold contour above which the solution does not converge. The threshold contour is the thick line, above which the solution is unconverged. The red dot represents the nominal values of beam voltage and current that we desire to use, which lies far above the threshold curve, which implies that this structure may oscillate when using the desired beam-parameters. Both band-edge oscillations (π and 2π) were observed in 3D particle simulations (*cf.* section 4g), confirming the instability prediction.

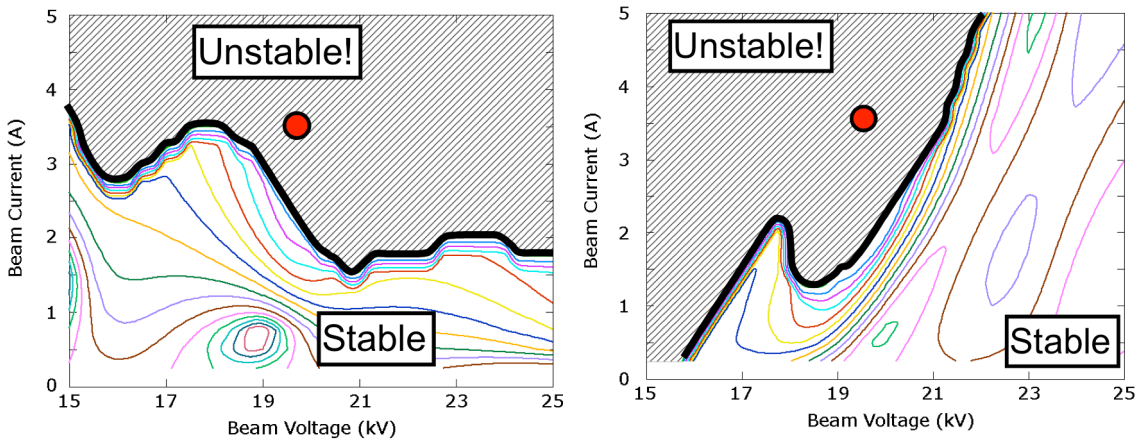

Figure 4.6: Gain contour maps. (a) Near π-point f_0=30.6 GHz. (b) Near 2π-point f_0=40.3 GHz.

4g) MAGIC3D Simulations

In order to address all the complications of the three-dimensional nature of the coupled-cavity structure, beam, and their interaction, we utilize the fully 3D particle-in-cell (PIC) finite-difference electromagnetic solver MAGIC3D to investigate the stability of a design. These simulations exhibit all kinds of oscillation mentioned so far (gain ripple, band-edge, power holes, backward wave, higher-order modes, and transverse interactions), and provide field and particle data suggesting methods to improve interaction and avoid instabilities. A suite of simulations with small offset confirms the insensitivity of the final design to manufacturing tolerances, and also the overall stability of the structure to oscillations of various nature.

PIC simulations are well-suited to looking for oscillations because the simulation does not make any assumptions about single-frequency excitation, stable amplifications, or forward-wave approximations, and have been used in several studies of amplifier stability [140] [141]. The "first-principles" and time-domain nature of the PIC simulations allow the simulations to more faithfully model all the effects and complications of a real device without having prior knowledge of the expected behavior of the system. The result is that oscillations are very apparent even when unexpected, and instabilities were investigated from the beginning due to their innate appearance in particle simulations.

The first example of an oscillation that was most apparent, and also seemingly most dire, was at an intersection with Mode 4 (*c.f.* Figure 4.3), but for a slightly different dispersion curve that included a bandgap near 1.75π. The simulation was started as a test of mid-band gain for a small-signal input with a slow turn-on of both the input signal (35 GHz drive frequency, and 1 mW drive power) and the electron beam. However, under even these unassuming conditions, the signal at the output began to grow exponentially. Figure 4.7 provides a frequency spectrum of the output waveguide voltage obtained by FFT of the voltage output, and also a time-history of the power through the output waveguide. The time-history shows the exponential gain after an initial turn-on transient. The spectral magnitude shows that the oscillation occurs near a frequency of 43 GHz – this frequency is out of the fundamental mode band (approximately 30-40 GHz) and is near both the beam-line intersection and the 1.75π band-edge. For the SWS used in this example, the higher-order mode analysis used previously showed that the threshold stability length was only 0.27" (the shortest length of all mode intersections), while the total circuit length in the MAGIC3D simulation was 0.81". In this case the position of the band-edge

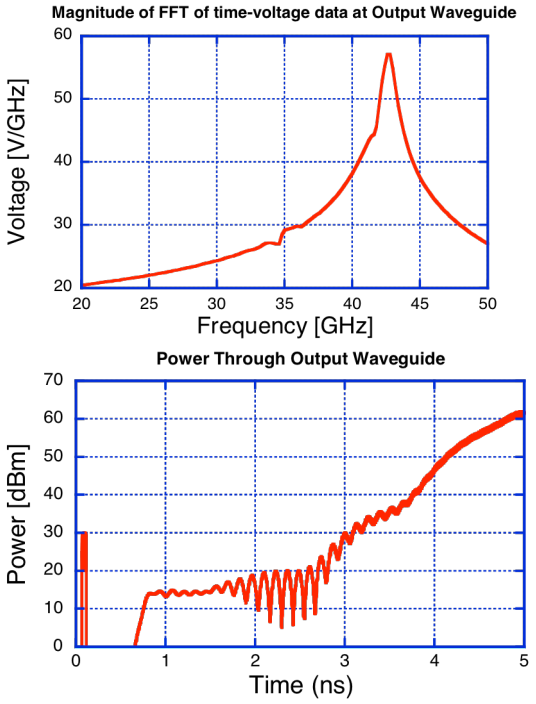

Figure 4.7: (a) FFT spectrum of output waveguide voltage, and (b) output waveguide power time-history, showing a strong oscillation at a frequency of a H.O.M. intersection.

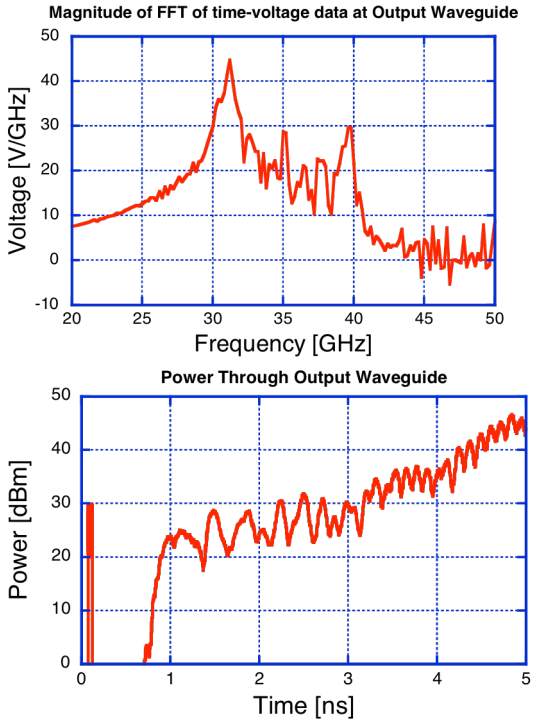

Figure 4.8: (a) FFT spectrum of output waveguide voltage, and (b) output waveguide power time-history, showing oscillations at a both band-edge frequencies (*c.f.* Figure 4.6).

with respect to the beam-line was aggravating the oscillation and decreasing the threshold – this was adjusted by changing the dispersion through geometry adjustments.

The second example of an oscillation that appeared through the innate characteristics of the sheet-beam structure were band-edge oscillations at the opposite ends of the fundamental mode (both π and 2π). The SWS used in this simulation was similar to the above, except that the 1.75π band-gap was minimized. The frequency range of the fundamental mode was maintained approximately between 30-40 GHz. The simulation was again run with a small drive-signal (1 mW) at the center of the fundamental mode (35 GHz) with slow turn-on times. Figure 4.8 exhibits frequency and time data for this example case. The time-history plot of the output power again shows exponential growth in the output power after some turn-on transient. The frequency spectrum clearly shows the predominance of the signals at 30 and 40 GHz (π and 2π). This structure and parameters were studied in the CHRISTINE-CC band-edge analysis previously with representative gain contour plots at the band-edge frequencies in Figure 4.6. It is confirmed in these two complimentary analyses that the increased current afforded by the

sheet-beam geometry creates the larger band-edge interactions. We account for this in later simulations by reducing the cold-bandwidth of the structure to 31-39 GHz.

Not all oscillations arise as quickly as the last two – many oscillations only appear after running quietly for 50 ns, or they might grow exponentially but have such a small growth rate that after ~20 ns would still remain in the small-amplitude drive signal, or possibly the simulation noise. The standard simulation we use to look for general stability is to set the input drive signal to zero amplitude and run the simulation with a slow turn-on time for the electron beam. The simulation then proceeds for 50-100 ns and a time-frequency analysis is performed to study any apparently growing frequency content. Furthermore, in order to assure stability of normal device operation, this analysis is repeated under worst-case scenarios – *e.g.* slight mismatch at the input port and large mismatch (or total reflection) at the output port. Appropriate steps can then be taken to assure stability under even the most arduous circumstances as detailed in the following section. This zero-drive stability test is of primary importance because it very directly shows the inherent stability of the amplifier device under test.

Another oscillation that appears more subtly in particle simulations is a power hole, of which we look here at the sheet-beam's potential coupling to the antisymmetric mode under misalignment. As an example, we use the same SWS parameters as used in the dispersion diagram of Figure 4.3 and obtain a sweep of frequencies across the range of the fundamental mode at a constant drive power of 200 W (strongly driven, but not saturated). Then the entire set of beam-tunnels was uniformly offset in the short transverse dimension to create a coupling of the excited wave with the transverse mode and to increase the longitudinal coupling of the wave with the electron beam. The results of gain vs. frequency are plotted in Figure 4.9 showing the standard parabolic gain variation for the perfectly aligned case, and in the offset beam-tunnel case showing a large ripple, or power-hole, at 36 GHz. We see in the dispersion diagram of Figure 4.3 that the upper band edge of the antisymmetric mode is at ~36 GHz, and that the beam-line crosses the

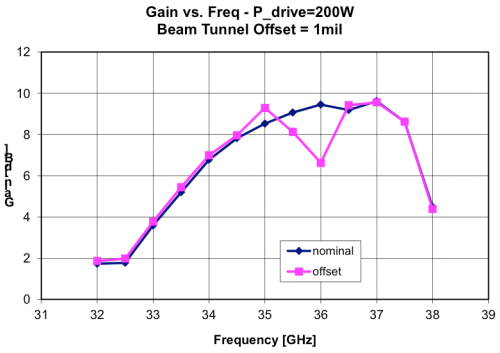

Figure 4.9: Gain vs. frequency across device bandwidth showing the appearance of a power-hole when the beam-tunnel is offset.

dispersion somewhere near this band-edge. This power hole was removed by adjusting the dispersion so that the antisymmetric mode band-edge was not in the middle of the operating band and therefore interacts less strongly with the bunched beam.

4h) Instability Mitigation Techniques

In order to combat the various oscillations that are inherent to this structure, many techniques were considered to reduce or suppress the interaction that leads to oscillations. Some techniques were investigated in terms of the loss provided to selective frequencies within an infinite structure without a beam. Other techniques involved adjusting the dispersion in various ways to avoid bad interactions. A third general technique was to adjust the fields of higher modes to reduce their interaction with the beam. The final technique was to change the structure in some prescribed manner along the axis to limit the undesirable interaction at any one frequency or intersection.

One of the first methods we investigated for selectively attenuating higher frequency modes was the standard method of applying lossy dielectrics in tuned cavities adjacent to the SWS cavities. We used the same eigenmode simulation setup as those in obtaining the dispersion diagrams and compared the calculated axial attenuation for the case of lossy dielectrics vs. only copper conductor losses. We obtained reasonable results with some frequency selectivity and modest attenuation for some of the higher frequency modes. However, these lossy dielectrics did not noticeably affect the antisymmetric modes (even when they were at the tuned frequency of the lossy dielectric). Loss was created in the antisymmetric modes by adding a lossy coating or insert on the side walls of the beam-tunnel where the current density is highest for these modes – this is very selective to the antisymmetric modes because very little current flows in the beam-tunnel for symmetric modes. Neither of these methods were pursued in the design of the proposed experimental device due to their increased complexity. One of the methods that we did use was increased broadband conductive losses, created by surface coating or appropriate choice of conductor material. The benefit of this method is that general stability is maintained for all modes regardless of current distributions. It is noted in many references (*e.g.* [4], [139]) that the forward gain is affected only modestly by the introduction of attenuation, while the backward wave and band-edge oscillations are affected much more by the increased loss. Therefore, we utilize the broadband conductive loss to help stabilize the fundamental mode band-edge oscillations (both π and 2π) that cannot be eliminated by

frequency selection (high and low frequencies) or suppressed by targeting differences in field-shape (they have the same field shape as the desired interaction mode).

In order to observe the field-shapes of the various modes and decide how the geometry could be altered to suppress interaction with modes and otherwise disrupt higher-order modes, we plot the surface currents and volumetric fields within the 3D modeling and graphical visualization tools contained in the electromagnetic software programs. Several salient points regarding the usefulness of these field-plots have been discussed in the above paragraph in terms of targeting the attenuation of only the antisymmetric mode vs. the operating symmetric mode. These field plots were also useful to suggest ways to decrease interaction with a higher symmetric mode with two electric field peaks across the length of the rectangular cavity – for example, extending the beam tunnel in one direction (see Figure 5.1 for an example of this geometry) will adjust the position of these peaks with respect to the beam, and greatly reduce their intensity, as there is no opposing conductor on the wide-sides of the beam-tunnel, only the short-sides have directly opposing conductors (this misshapes the nearly uniform quality of the fundamental mode, but only secondarily to the effects on undesired modes). We adopt this stretched beam-tunnel in the final design for its effects on the higher-order mode, and the dispersion shaping effect on the antisymmetric mode moving the antisymmetric mode almost completely out of the range of interaction with the fundamental mode.

Continuing on the theme of adjusting the geometry, we investigated ways that the geometry could be altered slightly to maintain the desired performance of the operating mode, but minimize instabilities due to bad intersections. In addition to the antisymmetric mode already mentioned, the most critical adjustment was the removal of the band-gap near 1.75π by appropriately shaping the dispersion through geometry adjustments. By changing the cavity resonance slightly and the total slot coupling amount, the symmetric modes are mostly coalesced (although not in the standard sense of coalesced-modes at 2π [142] – illustrated in Figure 4.10). Although concerns arise about manufacturing imperfections causing an unintentional band-gap, it has been determined that this is only a concern when the fractional frequency width of the band-gap is larger than the Pierce gain parameter [123], *i.e.*:

$$\frac{\Delta f}{f} \geq C_{Pierce}$$

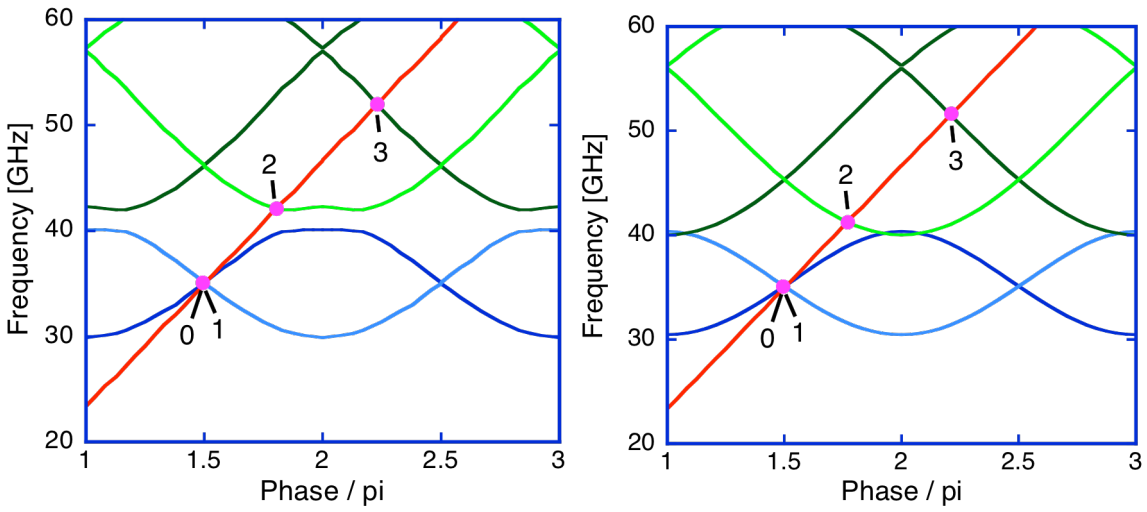

Figure 4.10: Dispersion plots for the symmetric modes showing how a geometry adjustment can decrease the bandgap to negligible size. (a) SWS with bandgap. (b) Adjusted SWS geometry to minimize bandgap.

The expected frequency width of the band-gap due to manufacturing tolerances is within the designed range of the gain parameter. As stated previously, the calculated stability threshold length in the original case was 0.27" (which is probably an underestimate due to the band-edge effects), the threshold in the case of the adjusted geometry is 3.83" (which has the added benefit of removing the band-edge effects) – for reference, the MAGIC3D simulated circuit length was 0.81" (12 cavity periods). It was seen in the particle simulations that the first structure oscillated due to the band-edge instability; in contrast, the adjusted structure does not oscillate at this band-edge frequency (however, the adjusted structure exhibits oscillations at both π and 2π points of the fundamental mode).

In order to avoid the band-edge oscillations of the fundamental mode we performed a combination of steps that also increased the stability of other modes as well. First, we slightly reduced the bandwidth of the fundamental mode – this was accomplished with a few straightforward adjustments to the cavity size and a reduced inter-cavity coupling. This removes the band-edge phase-velocities from the synchronous beam-line velocity and reduces the interaction. Second, we monitored the gain/cell of the structure (related to the Pierce gain parameter), reducing the amount of gain when the interaction was too strong. This reduction was accomplished with a combination of increasing the beam-tunnel height, and adjusting the gap-length (which simultaneously adjusts the gap transit-angle and the effective voltage that the cavity experiences for a given power propagated). Third, was the increase of broadband

conductive loss on the structure. The increased conductor loss is only used at the input end of the structure where the power is low, therefore the exponentially larger signal at the output does not experience loss at an increased rate and the total power lost through finite conductivity attenuation is not increased proportionally with the inverse factor of the decreased conductivity – the proposed design attenuates more total power in the final sections of high conductivity copper than in the entire length of the lower conductivity input section.

The final method investigated in order to mitigate interactions with higher-order modes is changing the period of the interaction structure to adjust the backward wave intersection points. This has been utilized in the proposed concept presented in Chapter 5, and is illustrated in terms of the dispersion characteristics in Figure 5.2 there.

Chapter 5: Final Design and Conclusions

In this chapter we develop the design of a sheet beam traveling-wave tube (TWT) amplifier with high power operation and moderate bandwidth. We utilize a three-slot, doubly periodic, staggered ladder coupled-cavity slow-wave structure developed and characterized at the U.S. Naval Research Laboratory. The design takes into account higher-order mode competition and device stability. A suite of particle-in-cell (PIC) simulations confirm that the device stably produces over 5 kW peak power across a 4 GHz bandwidth, and is reasonably tolerant to achievable mechanical tolerances and misalignments.

5a) Slow-Wave Structure & Dispersion

The structure utilized for the sheet-beam TWTA is a three-slot, doubly periodic, staggered-ladder coupled-cavity slow-wave structure developed and characterized at the U.S. Naval Research Laboratory [74] [75]. The geometry is of the same generic design pictured and described in previous chapters with three additional parameters as illustrated in Figure 5.1. First, the axial cavity gap length is specified, while this value was originally assumed to be equal to the axial length of the septum (one half the axial length of a half-period). Second, the variable slots parallel to the beam tunnel are offset from the wide edge of the cavity to allow easier variation of the dispersion diagram and minimize this structure's bandgap in the fundamental mode. Third, the beam tunnel is extended on one side out to the wide edge of the cavity to allow for adjustment of the transverse modes. There are two values listed for period because there are two sections of uniform SWS with identical frequency vs. phase characteristics, but different period.

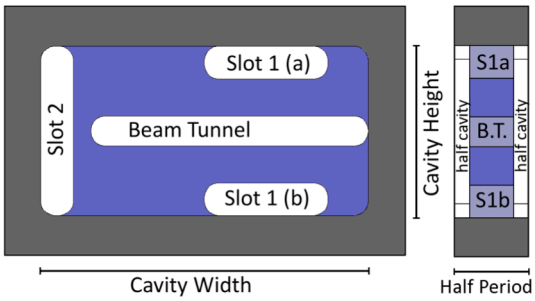

Figure 5.1: Generic design for one cell (half-period) of the three-slot SWS.

The dispersive characteristics of a structure with parameters listed in Table 5-I were computed with commercial 3D finite-element solvers (HFSS [81] and Analyst [82]) are presented in Figure 5.2, where frequency is plotted versus phase advance per cell. The dispersion for both sections of uniform structure are visually indistinguishable on a plot of this nature, but the beam-line is plotted twice to show the changing period. In this dispersion plot we see that the lowest mode

SWS Parameter	[in]	[mm]
input-section period	0.066	1.676
output-section period	0.064	1.626
cavity gap length	0.0262	0.6655
slot 1 & 2 width	0.030	0.762
slot 1 length	0.113	2.870
slot 1 offset	0.037	0.940
cavity width	0.300	7.620
cavity height	0.155	3.937
beam tunnel (offset)		
length	0.254	6.452
width	0.0275	0.700

Table 5-I: Parameters for the final design simulated slow-wave structure.

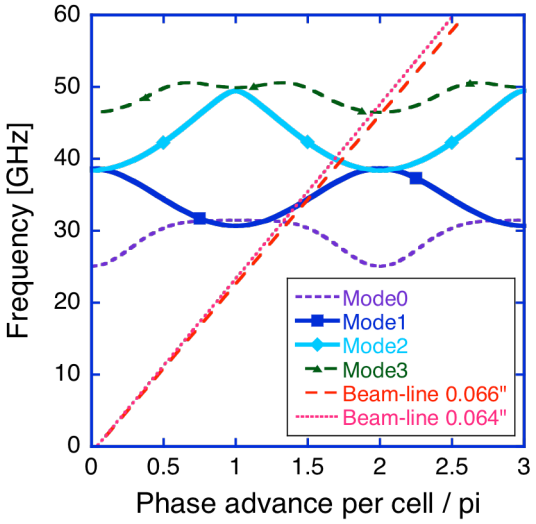

Figure 5.2: Simulated dispersion diagram (frequency vs. phase) with respect to one cavity-period. Beam-lines are included to represent the slow space-charge waves supported by periodic structures of specified period length.

is an antisymmetric mode with fields predominantly transverse to the beam, the interaction of which will be discussed with the fully 3D particle-in-cell simulations. The fundamental longitudinal mode, Mode1 in Figure 5.2, has the shape of a standard CC-SWS. The only major differences of this SWS from the design in Ref. [75] are the reduction in the additional three-slot stop-band and the fundamental mode bandwidth, both for improved stability. Although, Mode1 and Mode2 are close in frequency around 2π and the modes couple in a complicated way, the modes are not coalesced in the normal manner (the group velocity of both modes goes to zero).

The SWS impedance is also calculated via numerical simulation in the usual way [78] [88] [75] with a few analytical assumptions for an infinitely-wide sheet geometry instead of azimuthal symmetry (using hyperbolic functions instead of modified Bessel functions). As a comparison of the similarities between the two sections of uniform SWS, the coupling impedances for the fundamental modes of both

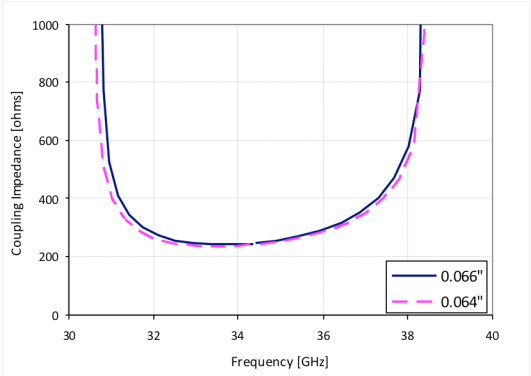

Figure 5.3: Simulated coupling impedance plotted vs. frequency for both sections of uniform periodic SWS.

sections are plotted in Figure 5.3 across the entire frequency band.

5b) Device Layout and Couplers

The initial design for a proof-of-principal sheet-beam amplifier experiment has been envisioned as a single-stage (no sever), low-gain, high-power amplifier. This decision was made in part to reuse the gun, collector, and transport systems from the W-band sheet-beam klystron, which has a short axial extent. The single-stage design also reduces any complications of matching a sever over a broad bandwidth as well as multiple modes – although a few sever designs were investigated with some success. Further, we have access to broadband, medium power drivers (~200 W across the band of interest), which will achieve our goals of obtaining more than 5 kW output power from a single stage device.

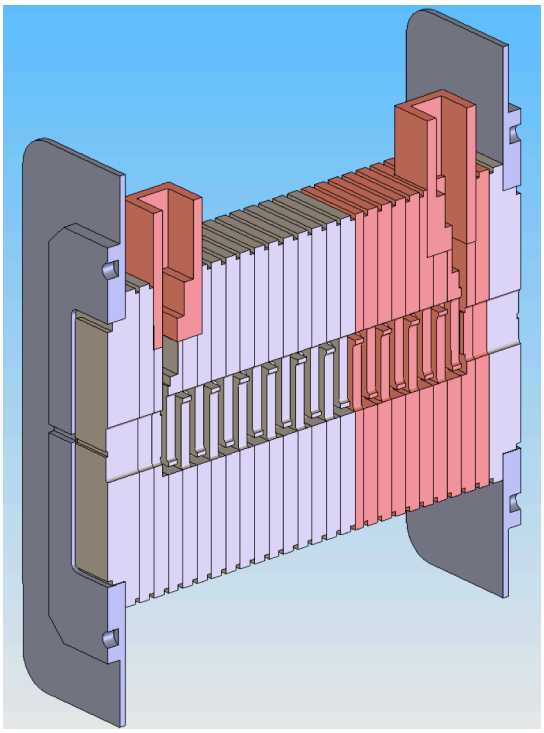

Figure 5.4: Solid-model (cut-away view) of coupled-cavity circuit.

A cutaway view of a solid-model for the coupled-cavity circuit section of the amplifier is pictured in Figure 5.4. There are 22 cavities, including the input/output cavities, with the first 14 made of CuNi 90/10 (σ = 5.24e6 S/m) with period 0.066", and the last 8 made of OFHC Cu (σ = 6.0e7 S/m) with period 0.064". The rectangular beam-tunnel slot extends through the middle of the structure, perpendicular to the waveguide couplers. This design consists of a set of identically machined plates that are stacked together in an alignment fixture and brazed together into one piece, with the waveguides attached subsequently. The weld-flanges on either side of the device are borrowed from the sheet-beam klystron design, and therefore mates with the gun and collector assemblies.

The waveguides into and out of the SWS are standard WR-28 size with identically step-tapered couplers into the first and last cavities. The coupler was developed to achieve a very good match across the entire frequency band of the structure, and has been discussed previously

[90]. Results of HFSS simulations of the RF response are presented in Figure 5.5, indicating a return loss better than 20 dB from 32-38 GHz, and a transmission loss of 2.0 dB. Furthermore, the coupler allows for this match without requiring transition cavities beyond the input/output cavity and the first/last set of coupling slots.

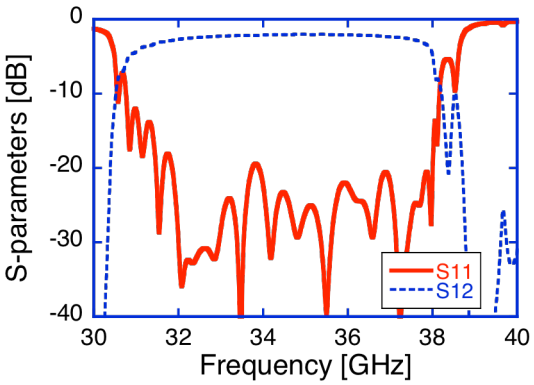

Figure 5.5: Simulated RF response of matched couplers attached to the SWS as illustrated in Figure 5.4.

5c) MAGIC3D Simulations and Stability

In order to address the 3-dimensional nature of the coupled-cavity structure, beam, and their interaction, we utilize the fully 3D particle-in-cell (PIC) finite-difference electromagnetic solver MAGIC3D [109] to simulate the amplifier characteristics under a variety of circumstances. These simulations confirm 1D gain estimates, exhibit oscillations when present, and provide field and particle data suggesting methods to improve interaction and avoid instabilities. Finally, a suite of simulations with small offset confirms the insensitivity of the structure to manufacturing tolerances, and also the overall stability of the structure to oscillations of various nature.

The simulation set up is of nearly identical geometry as the solid model in Figure 5.4, with the electromagnetically important regions being the vacuum interior with appropriately conducting boundaries. The geometry was altered only slightly to convert all the curved corners of the rectangular cavities and slots into squared corners, appropriate for the stair-step geometry of the Cartesian simulation grid and represent only a minor change for the sheet geometry. The simulation setup is similar to a single section of the structure simulated in Ref. [115]. The electromagnetic response of the structure across the operating band confirms that the couplers provide a good match even with the minor geometry changes (which is an additional data point on the robust design of the couplers).

Particle simulations were conducted with a variety of beams to probe the structure response to varying electron beam. The initial device simulations used the uniform current-density beam model within MAGIC3D, with a beam voltage of 19.5 kV, beam current of 3.5 A, beam height of 0.3 mm, and beam width of 4.0 mm. For these initial simulations, the magnetic field was

defined as a uniform axial field with magnitude 8.5 kG, which is close to the peak field obtained in the sheet-beam gun beam-stick experiment [93]. Also used was a thermal beam created via MICHELLE [118] simulation of the electron gun using simulated magnetic fields from Maxwell software [81]. Finally, all these simulated data were combined to perform PIC simulations in MAGIC3D with a realistic thermal beam from MICHELLE and focusing magnetic fields derived from geometry through Maxwell simulations. These various simulations have increased our confidence and understanding of the simulation, the beam-wave interaction, and tolerances of the electron beam on the device gain. The following results will represent data from the realistic thermal beam model with the simulated magnetic field.

The various simulation data have predicted stable amplifier operation with output powers up to 8-9 kW. For the simulated bandwidth curves presented in Figure 5.6, the drive power is maintained at a constant 200 W, which represents the attainable source power in experiment, and a simulated thermal beam is used. The data indicates that at constant drive the 3 dB bandwidth is ~4 GHz, and a saturated bandwidth would be greater if saturation were achievable in the axial length. Even with reasonable reflections due to unintended mismatches at the input and output, the experimental amplifier should be able to achieve greater than 5 kW output power across a modest bandwidth.

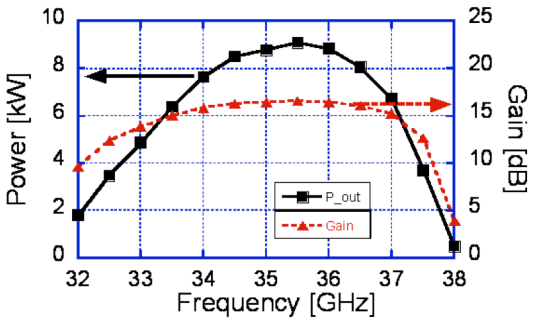

Figure 5.6: Output RF power and gain vs. frequency at constant drive power (P_{drive} = 200 W).

Further simulation data is presented as a drive curve for three frequencies across the operating band in Figure 5.7. The 200 W drive power limit we expect in experiment is marked as a solid black line for reference – hence, the structure has not reached saturation. Also, one can see that although the amplifier gain is only 16 dB at the 200 W drive level, there is 18-20 dB gain at small-signal drive powers. The peak power

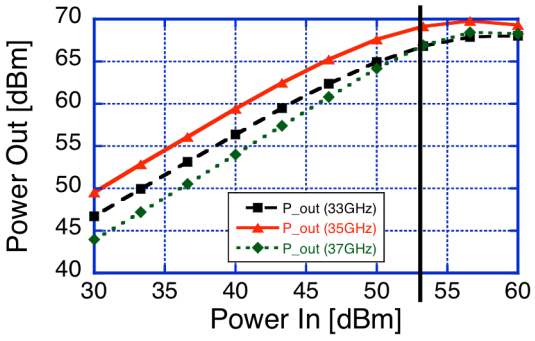

Figure 5.7: Output RF power vs. input drive power at three drive frequencies. The experimental maximum drive power, P_{drive} = 200 W, is marked with a solid black line.

simulated (~10 kW) represents a 14% electronic efficiency, which is similar to round-beam devices of this type, and this value could be optimized somewhat. We expect that the total device gain could increase proportional to total length if a two-section device were designed with an appropriate sever, thus allowing saturation to be reached by a solid-state driver.

Throughout the course of the development of this amplifier three main causes of instability and oscillation have been of concern – 1) band-edge oscillations, 2) higher-order-mode oscillation, 3) transverse mode oscillation. The band-edge oscillation was eliminated from concern by moderately reducing the bandwidth of the fundamental mode pass-band, and introducing reasonable loss in the SWS. Higher-order-mode instabilities were mitigated by minimizing the 3-slot band-gap inherent in the structure, introducing moderate loss in the input section, and by changing the period of the latter section to spoil the interaction. Transverse modes were studied extensively by offsetting the rectangular beam tunnel so as to excite the transverse mode, which did not generally lead to oscillation, but caused a power hole at the upper band-edge of the transverse mode, which was avoided by shifting the transverse mode lower in frequency, below the fundamental mode. Numerous zero-drive, and fully-driven simulations confirm that the device does not oscillate under realistic beam conditions.

5d) Conclusions

Based on numerous design analyses and simulations, we conclude that the design of a sheet-beam couple-cavity traveling-wave tube amplifier looks promising for stable 5kW amplifier operation across a moderate bandwidth. The sheet-beam is obtained from an experimentally demonstrated source, and is manufactured with conventional technologies. This represents a 5-10x increase in peak output power at this frequency range, while maintaining bandwidth.

The next steps planned for this device are to construct a device utilizing vacuum-grade materials for cold-test on a network analyzer. Then a subsequent hot-test experiment will be conducted in pulsed mode using the NRL pulse modulator (capable of pulse durations of 2-25 μs and repetition rates up to 20 Hz). The hot-test measurements will produce drive-curves, bandwidth curves, and body-current measurements, and will experimentally confirm the stability of the structure.

Appendix I: Sheet-Beam Small-Signal Gain

A sheet-beam centered within the beam-tunnel region has some transverse width and height, and therefore each part of the beam experiences a slightly different field as it streams axially through the structure. However, the longitudinal electric field is generally shaped to provide minimal variation across the width (long-extent) of the electron beam, and for thin beams the field variation with height is minimal, as the field in the fundamental mode does not vary greatly near the symmetry plane. Therefore, to first order, the interaction can be described as if the beam interacts uniformly with the longitudinal electric field on-axis, or, alternatively, uniformly with an averaged representation of the fields over the beam transverse cross-section – this is the principle idea of a 1D analysis that we will develop and utilize in the following sections.

1-Dimensional Coupled-Cavity Field Analysis

Coupled-cavity slow-wave structures (CC-SWS's) fall somewhere between the continuous field interaction of a helix structure and the axially discrete interaction of a klystron cavity, and so different approaches can be made to analyze the fields. The generally periodic nature of the cavities will be utilized to fill in the analysis and provide comparisons, which allows for the transfer of quantitative data from 1D continuous interaction analyses to discrete cavity models. The field within the beam-tunnel is smoothly varying and is expanded in analytical forms using standard analytical techniques for cavity and periodic structures.

We start by looking at a hypothetical infinite chain of uniform coupled-cavity structures. The electromagnetic field within the cavity chain is represented by a traveling wave with some specified phase advance (modulo 2π) from period N to period N+1 (the phase advance is determined by the frequency as a result of the dispersion relation of the structure). Therefore, the time-harmonic phasor representation of the electric fields is complex, with complex phase varying through space (in contrast to a resonant klystron cavity, which would resonate with all fields oscillating in phase). However, for small gap and small beam tunnel we make the assumption that the field is quasi-static within the beam tunnel, and go as far as calculating the voltage across the gap at the beam-tunnel edge

$$V_{gap} = \left| \int_{z=-gap/2}^{z=gap/2} E_z|_{B.T.} dz \right| \qquad \text{(I.1)}$$

where $E_z|_{B.T.}$ is the complex electric field long a line across the cavity gap at the beam tunnel edge, the integral is a complex integral, and the result is the quasi-static magnitude of the voltage across the gap. This is the standard assumption in conventional CC-SWS, and is useful for applying the field analysis and expansion derived subsequently to a circuit model for the transmission of the electromagnetic wave along the structure.

As we are looking for a 1-dimensional representation of the fields at the beam-tunnel axis, and we are given the gap voltage, we must first find some analytical models for the electric fields on-axis in terms of the gap voltages. The subsequent step is to Fourier analyze the field because this will be used in the next section to find the appropriate beam-wave interaction. First, we expand the complex axial electric field as a sum of complex-weighted, shifted field shape functions.

$$E_z(z) = \sum_n V_n f_{axis}(z - z_n) \tag{I.2}$$

The electric field may maintain the MKS units of [V/m], and the complex weights may have the units of voltage to relate closely to the gap voltage. Therefore the field shape function has units of inverse meters, and maintains a normalization defined as

$$\int_{-\infty}^{\infty} f_{axis}(z)dz = 1 \tag{1.3}$$

Any piece-wise continuous function which can be appropriately normalized could conceivably be used to model the on-axis field. We tend to pick functions that resemble the actual fields and are analytically simple. We will present and compare a few simple example functions with the actual fields produced by simulations of a real structure.

As a schematic, Figure I - 1 illustrates a slice of geometry near the beam-tunnel, indicating a parabolic field shape function with axial electric field magnitude indicating the nature of the complex-weighted sum. The structure is

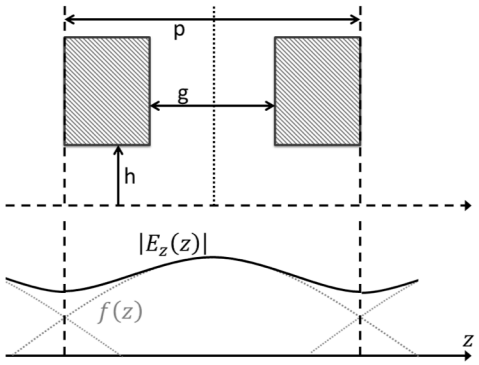

Figure I - 1: Schematic diagram of geometry (top) and fields (bottom) within the beam-tunnel over one period.

periodic with period *p*, beam-tunnel half-height *h*, and gap spacing *g*.

In the analysis presented here, we treat each cavity field separately and represent the total field as the complex sum of all the cavity fields. Of course the fields from one cavity are directly coupled to the cavities on either side through the coupling slots, and the total field is necessary to find the beam-wave interaction. However, this analysis is introduced to compare simulation analyses that utilize this method of field construction. Also, there is a certain understanding to be gained of a beam interaction with a single cavity, and that amplified resonance is coupled to both forward and backward cavities, which can cause gain ripple or oscillations in certain cases. The Fourier transform of this single cavity field is used to relate the expected beam-wave interaction from simulation analyses of this type with a continuous-field interaction used in other analyses.

The Fourier transform of the axial electric field will subsequently be used for analyzing the beam-wave interaction. We include it here to compare examples of analytical field shape functions. The transform of the field shape function is expressed as

$$e(k_z) = \int_{-\infty}^{\infty} e^{-ik_z z'} f_{axis}(z') dz' \qquad \text{(I.4)}$$

The following three field shape functions are presented as models of various complexities and will be subsequently utilized in beam-wave analyses.

Uniform gap:

In klystron cavity theory, the simplest model for field distribution is zero fields within the beam-tunnel, and uniform electric field within the gap. This was a more appropriate model when the beam-tunnel entrances were covered with a conducting grid that would act as a permeable membrane for the electron-beam, but precludes the electric field from the beam-tunnel (modern cavities are not built with grids). The axial electric field shape function and corresponding Fourier transform are represented as follows:

$$f_{axis}(z') = \frac{1}{g} \;\; for \; |z'| < \frac{g}{2} \qquad \text{(I.5)}$$

$$e(k_z) = \frac{\sin(k_z g/2)}{k_z g/2} \qquad \text{(I.6)}$$

Parabolic:

A slightly improved model for the on-axis axial electric field might be a smoothly varying field that decreases to zero some distance into the beam-tunnel. The parabolic model has a maximum at the gap center, and decreases symmetrically from that point, to some effective length L_{eff}, which is a variable parameter. A representation of the parabolic field shape function was presented graphically in Figure I - 1. The axial electric field shape function and corresponding Fourier transform are represented as follows:

$$f_{axis}(z') = \frac{3}{4L_{eff}}\left(1 - \left(\frac{z'}{L_{eff}}\right)^2\right) \quad for\ |z'| < L_{eff} \tag{I.7}$$

$$e(k_z) = \frac{3}{{k_z}^2 {L_{eff}}^2}\left(\frac{\sin(k_z L_{eff})}{k_z L_{eff}} - \cos(k_z L_{eff})\right) \tag{I.8}$$

Kosmahl-Branch (on-axis):

The modern standard for analytical approximation of fields in cavity gap is that developed by Kosmahl and Branch [107]. The following is a form that provides the correct normalization as required, preserving the field shape. The utilization of the Kosmahl-Branch approximation in modern analyses is that it describes the fields at all points within the beam-tunnel, and can therefore accurately describe the change with radius of the fields and interaction – however, we look only at the expression on-axis at this point. This model also has one variable parameter, *m*, that must be fit to expected data or otherwise predetermined. The increased complexity is obvious from the defining equation as this model is represented by an infinite sum. However, this sum converges rapidly for fields on axis, so only a few terms are required to achieve sufficient accuracy. The axial electric field shape function and corresponding Fourier transform are represented as follows:

$$f_{axis}(z') = \sum_{n'=-\infty}^{\infty} \frac{\cos(\omega h/c)}{m^2 + {\beta_{n'}}^2} \frac{m^2 \cos(\beta_{n'} g/2) + \beta_{n'} m \coth(mg/2) \sin(\beta_{n'} g/2)}{\cosh(\gamma_{n'} h)} \cos(\beta_{n'} z')$$

$$for\ |z'| < p \tag{I.9}$$

$$e(k_z) = \frac{\cos(\omega h/c)}{4p} \sum_{n'=-\infty}^{\infty} \frac{m^2 \cos(\beta_{n'} g/2) + \beta_{n'} m \coth(mg/2) \sin(\beta_{n'} g/2)}{\left(m^2 + {\beta_{n'}}^2\right) \cosh(\gamma_{n'} h)} \delta(\beta_{n'} - k_z)$$

(I.10)

1D Beam-Wave Interaction

There are several ways to investigate beam-wave interaction in a periodic structure, of which I will give the highlights of two approaches: a single-particle, ballistic (or Lagrangian) approach; and a sheet-fluid, Eularian approach. The ballistic approach is so ubiquitous as to require only a couple good references and little explanation – we adapt the approach for a sheet-geometry and relate several key parameters. The Eularian approach is adapted as well for an infinite planar sheet electron beam.

We follow the development of Branch for electron beam coupling in interaction gaps of cylindrical symmetry [143], but assume top/bottom symmetry and infinitely-wide uniform gap. We will also simplify the present discussion to a thin, infinite sheet-beam traveling on-axis. The beam-tunnel half-height is x_w, and the gap length is g (the gap extends from z = 0 to g). An axially streaming electron within the beam has kinetic energy eV_0, where e is the electron charge and V_0 is the dc voltage of the electron entering the gap. Harmonically-oscillating fields exist within the CC-SWS, gap, and extending into the beam-tunnel (there is no conducting grid at the beam tunnel opening), with time-variation $e^{-i\omega t}$, and a 1D variation of the gap voltage defined as

$$V_{gap} = \left|\int_{z=-\infty}^{\infty} E_z|_{axis} dz\right| \tag{I.11}$$

where $E_z|_{axis}$ is the electric field caused by the single cavity and integrated along a line of infinite extent on-axis.

Branch shows that, to first order ($V_{gap} << V_o$) , an electron entering the gap at time $t = t_0$ will experience a change in kinetic energy

$$\Delta KE = \frac{1}{2} m({u_1}^2 - {u_0}^2) = e^{-i\omega t_0} \int_{z=z_0}^{z_1} eE_z(b,z)dz \tag{I.12}$$

We define the on-axis electric field in terms of the field shape function and, alternatively, as the Fourier inverse of the transform,

$$\begin{aligned} E_z(z,t) &= V_{gap} f_{axis}(z) e^{-i\omega t} \\ &= V_{gap} e^{-i\omega t} \int_{k_z=-\infty}^{\infty} e(k_z) e^{ik_z z} dk_z \end{aligned} \tag{I.13}$$

Therefore the energy transfer to the single electron by traversing through the entire field of a single cavity with a propagation constant $\beta_e = \omega/u_0$, such that $\beta_e z = \omega t$, can be expressed as

$$\begin{aligned}\Delta KE &= eV_{gap}e^{-i\omega t_0}\int_{z=-\infty}^{\infty}\int_{k_z=-\infty}^{\infty} e(k_z)e^{ik_z z - i\omega t}dk_z\,dz \\ &= eV_{gap}e^{-i\omega t_0}\int_{k_z=-\infty}^{\infty} e(k_z)\int_{z=-\infty}^{\infty} e^{ik_z z - i\beta_e z}dz\,dk_z \\ &= eV_{gap}e^{-i\omega t_0}\int_{k_z=-\infty}^{\infty} e(k_z)\delta(k_z-\beta_e)dk_z \\ &= eV_{gap}e^{-i\omega t_0}\cdot e(\beta_e) \qquad \text{(I.14)}\end{aligned}$$

Therefore, instead of gaining kinetic energy proportional to the gap voltage, there is a factor dependent on the Fourier transform of the field shape and the velocity of the beam. There are obviously two extremes for the field shapes that have very different implications on the kinetic energy – the first is that a field with an impulse at the center of the gap will have a maximally uniform effect on any beam velocity, and the second is that a uniform field will only be effective on a beam exactly synchronous with the wave. The field shape factor is important for Lagrangian theories of small-signal gain and numerical simulations of large-signal operation, where the interaction experienced between the beam and a single cavity is reduced somewhat by this factor.

To adapt the full theory in [143] to a sheet geometry, we make a few changes to the analytical expressions for the field. In an infinitely-wide beam-tunnel, the field-shape within this hypothetical beam-tunnel that satisfies Maxwell's equations is a linear combination of hyperbolic sines and cosines. Specifically, for the fundamental mode that has axial electric field symmetric about the axis, we see that a uniform field has an axial component expressed as

$$E_z = Ae^{i(\omega t-\beta z)}\cosh(\gamma x), \qquad \text{(I.15)}$$

where *x* is the transverse distance from the axis in the short (non-infinite) direction.

The effective voltage experienced by an electron beam on-axis can be written in the following manner:

$$V_{eff} = V_{gap} \times M_{gap} M_{radius} \qquad \text{(I.16)}$$

where M_{gap}, the gap coupling coefficient, is calculated by the magnitude of the Fourier-transform of the field-shape, and M_{radius}, the radial coupling coefficient, is a ratio of the field strengths at the gap to the beam-tunnel wall. The combination of these two coefficients represents the interaction of the beam particles with the field with a given voltage between the opposing faces of the cavity.

The complete analysis above suggests that a total interaction impedance should take into account the factors of the field shape and the distance of the beam-tunnel wall to the beam.

3D Impedance Calculations and Comparisons

We calculate and compare 2 different impedances that are used for different simulation codes. These impedances are evaluated directly from HFSS (or Analyst) field solutions. There is an equivalence between the two impedances that can be readily evaluated for the coupled-cavity case, where the gap is easily defined and the fields are "analytically known". We term the two different impedances the Kino Impedance (Gap Voltage Impedance), and the Pierce Impedance (also called the Coupling, or Interaction Impedance). They are evaluated as follows in accordance with convention to coupled-cavity structures (*e.g.* see [78]).

$$K_{Pierce} = \frac{E_n^{\,2}}{2k_n^{\,2}P_{RF}} \tag{I.17}$$

$$Z = \frac{V^2}{2P_{RF}} \tag{I.18}$$

Where E_n is the nth spatial harmonic of the on-axis axial electric field (defined explicitly below), k_n is the axial phase constant for that same harmonic, P_{RF} is the RF power flow, and V is the gap voltage. For a cavity gap, Kosmahl and Branch [107] relate the V and E_n terms as follows.

$$V = \left| \int_{z=0}^{z=L} E_z\left(r = r_w, z\right) dz \right| \tag{I.19}$$

$$E_n = \frac{1}{L} \int_{z=0}^{z=L} E_z\left(r = 0, z\right) e^{ik_n z} dz \tag{I.20}$$

$$V = LM_{gap}(k_n g)M_{radius}(\gamma_n r_w)E_n \tag{I.21}$$

Where r_w is the beam-tunnel wall radius, L is the axial length of one period, g is the axial length of the gap, M_{gap} is an axial coupling coefficient (transit-time factor) that depends on the field shape, and M_{radial} is a radial coupling coefficient that depends on the radius of the beam-tunnel wall, and $\gamma_n^2 = k_n^2 - \left(\frac{\omega}{c}\right)^2$. These terms aren't truly independent in the sense that increasing the beam-tunnel radius will increase leakage into the beam-tunnel, which will affect M_{gap} in addition to M_{radius}. In standard coupled-cavity tubes with a defined beam-tunnel gap, both the coupling coefficients have analytical approximations that are standard (borrowed from Klystron gap theory):

$$M_{gap}(k_n g) = \frac{\sin(k_n g/2)}{k_n g/2} \tag{I.22}$$

$$M_{radius}(\gamma_n r_w) = \frac{1}{I_0(\gamma_n r_w)} \tag{I.23}$$

Where I_0 is the modified Bessel function of the first kind. With all the relationship between V and E_n and the definitions of impedance above, we can form a relationship between K_{Pierce} and Z.

$$Z = K_{Pierce}\left(\frac{k_n L}{M_{gap}M_{radius}}\right)^2 \tag{I.24}$$

Therefore, the Pierce Impedance integration with the transit-factor included in the integral is equivalent to finding the integrated complex voltage and including the transit-time coupling coefficient. Also, the Pierce impedance is a function of position over the beam area (strongest near the conducting walls), so multiple evaluations over the area will produce a correctly averaged impedance. Furthermore, there are some structures that do not have standard gaps and no analytical approximations for either coupling coefficient – these structures require the coupling impedance to be evaluated using the exact field shape provided by modern 3D simulation tools, and accounting for transit-time directly in the integration.

Figure I - 2 illustrates a comparison of the Kosmahl-Branch analysis of $M_{gap}M_{radius}$ (blue curve), the HFSS results expressed as a ratio of the evaluated impedances (pink curve), and the klystron-theory approximations (yellow curve) for the 3-Slot sheet-beam coupled-cavity SWS under investigation at NRL. They agree well, with the Kosmahl-Branch analysis having a slightly smaller error (in the mean-squared-error sense) than the klystron-theory approximation. Note that for a sheet-beam structure modified Bessel functions have been replaced with hyperbolic functions and the analysis still holds (reasonably well).

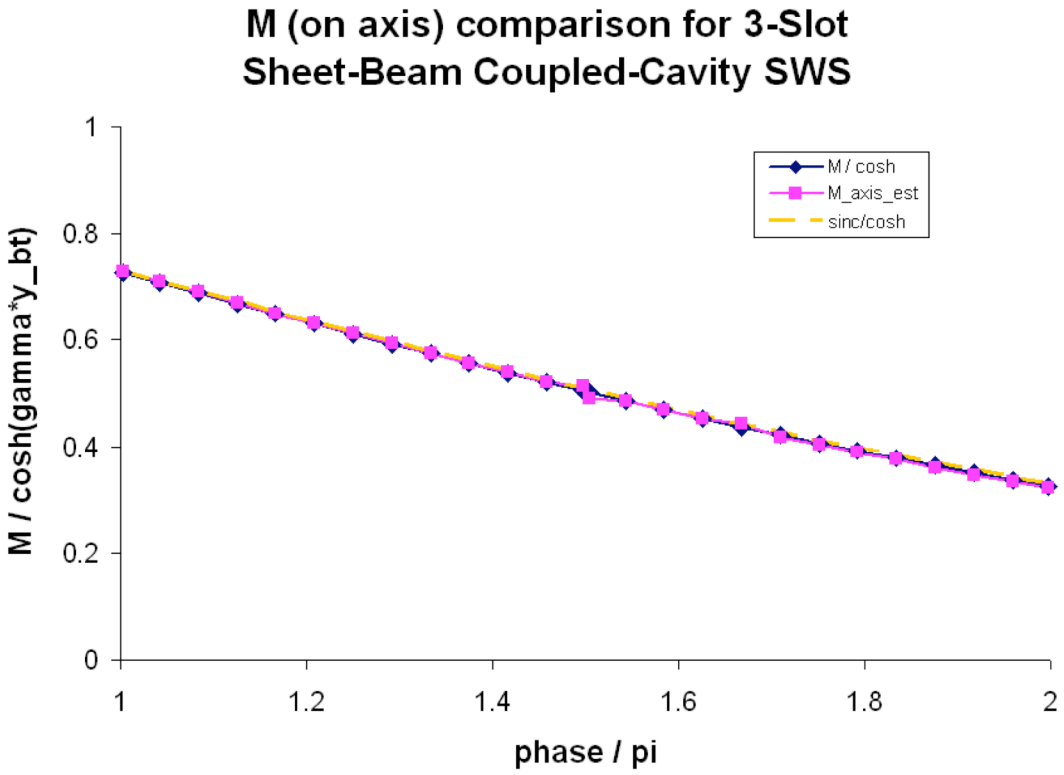

Figure I - 2: Comparison of theoretical coupling coefficients with the computed values from HFSS.

This is particularly important for determining the Pierce gain parameter, C_{Pierce}, used for small-signal gain analysis in a traveling-wave tube.

$$C_{Pierce}^{\ 3} = \frac{K_n I_{Beam}}{4V_{Beam}} = \frac{ZI_{Beam}}{4V_{Beam}}\left(\frac{M_{gap}M_{radius}}{k_n L}\right)^2 \qquad \text{(I.25)}$$

Infinite Planar Beam Space Charge Waves

In order to account for the self-field effects of the planar beam we develop an Eulerian approach for the sheet-beam system. The following are based on the cylindrical beam, confined flow model of [144] (with reference to [145] and [146]). We start with a model of the planar field configuration and develop a dispersion relation for the space-charge waves that has the same form as a cylindrical beam.

We consider an infinitely wide (in the *y*-dimension) planar geometry with a beam of finite size in the *x*-dimension which propagates in the *z*-direction. Assuming a nonrelativistic beam in which the Lorentz force can be neglected, we write the fluid equations of motion using *z* as an independent variable,

$$Nm\frac{d\mathbf{v}}{dt} = \rho\mathbf{E} + \mathbf{v}\times\mathbf{B}_0 \qquad \text{(I.26a)}$$

$$\nabla\cdot\mathbf{J} = -j\omega\rho. \qquad \text{(I.26c)}$$

Here $\mathbf{B}_0$ is a strong focusing field that limits the motion of the particles to the axial direction.

We assume that the AC fields vary sinusoidally with frequency ω with traveling wave form $\exp(j\omega t - j\beta z)$.

The equilibrium electron beam has a uniform density profile in x and y for |x|< a with the form,

$$N_0(x) = \begin{pmatrix} \frac{K_0}{2av_{z0}e} & |x| < a \\ 0 & otherwise \end{pmatrix}, \qquad \text{(I.27)}$$

where K_0 is the effective surface current density of the beam.

Starting from equations (I.26), we can find first order relations for the current density and the axial electric field, which can be used in Maxwell's equations to find a self-consistent set of Helmholtz equations (Collin's equations (9.16)):

$$\nabla_t{}^2 A_z + p^2 A_z = 0 \qquad 0 \le |\mathrm{x}| \le \mathrm{a} \qquad \text{(I.28a)}$$

$$\nabla_t{}^2 A_z - h^2 A_z = 0 \qquad \mathrm{a} \le |\mathrm{x}| \le \mathrm{b} \qquad \text{(I.28b)}$$

where we use wavenumbers defined by

$$p^2 = -\beta^2 + {k_0}^2 + \left(\frac{\omega_p}{\omega}\right)^2 {\beta_0}^2 \frac{\beta^2 - {k_0}^2}{(\beta_0 - \beta)^2}$$

$$= -\left(\beta^2 - {k_0}^2\right)\left[1 - \left(\frac{\omega_p}{\omega}\right)^2 \left(\frac{\beta_0}{\beta_0 - \beta}\right)^2\right] \quad \text{(I.29a)}$$

$$h^2 = \beta^2 - {k_0}^2 \quad \text{(I.29b)}$$

Applying equations (I.28) to the planar geometry with no *y* variation reduces to

$$\frac{d^2}{dx^2}\psi + \begin{Bmatrix} p^2 \\ -h^2 \end{Bmatrix}\psi = 0 \quad \text{(I.30)}$$

where $A_z = \psi(x)e^{-j\beta z}$. Because the space-charge waves are slow-waves, with $\beta \approx \beta_0 \gg k_0$, p and h are real valued, and the solutions of ψ are trigonometric and hyperbolic functions. Matching the fields at the beam edge, and setting the axial electric field to zero at the beam-tunnel wall leads to the relation:

$$p\tan(pa) = h\frac{\tanh(ha) + \coth(hb)}{1 - \tanh(ha)\coth(hb)} \quad \text{(I.31)}$$

which along with equations I.29 determine the propagation constant β. The solution to these equations can be cast in a form

$$\beta = \beta_0\left(1 \pm \frac{R\omega_p}{\omega}\right) \quad \text{(I.29b)}$$

where ${\omega_p}^2 = \rho_0 e/m\epsilon_0$ is the electron plasma frequency, and *R* is a reduction factor determined by the solution. This can be compared to the analysis and results of [144] and [145]. A dispersion relation for the interaction of the space-charge waves and the slow-wave structure fields can be constructed similarly and has been implemented in the CHRISTINE-1D and CHRISTINE-CC sheet-beam models.

Appendix II: Biperiodic SWS Eigenmode Simulations

General SWS Eigenmode Simulations

In order to determine the dispersive characteristics of a periodic slow-wave structure, the standard simulation technique is to perform an eigenmode simulation on one axial period of the structure with matching boundaries on opposite axial faces. For a given phase-advance between the matching boundaries, the solution data obtained from the simulation include the eigenfrequency (dispersion) and fully 3-dimensional field data within the solution domain for a specified number of modes. For a sweep of matching boundary phase-advances, we obtain a full dispersion curve and set of data with which to obtain field quantities of interest.

Generally, the solution domain is bounded in the transverse dimensions by conducting walls and the matching boundaries are planes perpendicular to the axial direction. The conducting walls may be lossy (finite conductivity), and there may be lossy elements within the solution domain as well (dielectric or conducting elements). The matching boundaries (called individually master and slave boundaries), may be placed at any axial position along the period (remaining exactly one period apart) so long as the geometry on the master surface is exactly identical to the geometry on the slave surface, which generally precludes locations of a step in the geometry.

The fields within the structure exhibit a periodic nature similar to the structure due to Floquet's theorem [147], [83], [144]. The general field solution within the structure can be expressed as:

$$\hat{E}(\vec{x},z)=\left\{\sum_{n=-\infty}^{+\infty}E_n(\vec{x})e^{j\beta_n z}\right\}e^{-j\omega t},\quad \beta_n=\beta_0+\frac{2\pi}{L}n, \tag{II.1}$$

where *L* is the period of the structure, and $E_n(\vec{x})$ is some function of the transverse coordinates. Here the *z*-dependence is expressed as the Fourier transform of a periodic function times a slowly varying phase determined by the matching-boundary phase-advance, $\beta_0=\phi/L$. At this point, the field solution is a general expression that is fixed by the requirements of Maxwell's equations and the given boundary conditions, and the Fourier components only come about as the consequence of the periodicity of the fields. There is no single phase-velocity, as there is no single β. However, there are unique values for group velocity and attenuation for a given mode, representing that as the mode propagates along the SWS the power positively

transmits energy along the SWS at a specified rate, and the transmitted power deposits energy into the lossy elements at another specified rate.

The concept of a periodic dispersion diagram (or Brillouin diagram), is allowed by the nature of the 2π periodic range of the matching-boundary phase-advance ($\phi \in [0, 2\pi]$), and the set of Fourier transform components that this directly implies. The utility in defining a frequency-phase relationship across multiple, periodic phase ranges is that a separate phase advance can be defined for each harmonic and the beam to wave velocity mismatch ($u_0 - v_{p,n}$) is used to calculate the gain across the band. Further, because the beam is designed to match the phase-velocity of one spatial harmonic, and all the other spatial harmonics have rapidly oscillating components that cancel out as the beam traverses a period, the only harmonic that interacts strongly with the beam is the one that lies along the beam-line of the dispersion curve. The 3D simulation software is tasked with solving the relevant partial differential equations with the appropriate boundary conditions, yielding frequency and total field information – the task of extracting the spatial harmonic information is achieved by computing the Fourier spectrum of the simulation results.

There is one last note of importance for the periodic dispersion diagram of reciprocal structures (here *reciprocal* refers to properties of the microwave media of the solution domain in the sense of the usual Lorentz-Reciprocity theorem for microwaves). For a steady-state excitation at angular frequency *ω*, the structure supports wavenumbers $\pm \beta_0(\omega)$, where one wavenumber corresponds to a forward-traveling wave (with respect to the *z*-axis), and the other wavenumber corresponding to a backward-traveling wave (for a lossless structure, $\beta_0(\omega)$ is real within the SWS pass-bands and imaginary within the SWS stop-bands). The importance of this reciprocity result is that after repeating both the forward and backward wavenumbers across multiple periods of phase advance the dispersion displays a mirror-symmetry, not only around $\beta_0 = \phi / L = 0$, but also around all phase multiples of π (i.e. $\beta_0 = \phi / L = n\pi / L$). Therefore, the entire dispersion-curve information for reciprocal structures is contained within a π phase range ($\phi \in [0, \pi]$ - this is generally termed the "first Brillouin zone"), and all data from π to 2π is obtained by "reflecting" the dispersion data from 0 to π across phase value of π.

The dispersion diagram can be complicated for structures with closely spaced modes, or even a plurality of modes occupying the same frequency range (overmoded). Sometimes modes can intersect on the dispersion diagram, and other times there is a small gap that must be resolved. Because the diagram obtained from simulation possesses a discrete set of phases, the distinction between modes can be difficult by inspection of the diagram alone. In order to identify connected modes in the dispersion diagram, we can compare field quantities, such as attenuation, voltage, and interaction impedance for neighboring points. If further clarification is required, more phase-points can be evaluated to increase the phase-resolution. Once this is accomplished, lines can connect the points to trace out distinct, contiguous modes.

Symmetric-Biperiodic SWS Eigenmode Simulations

A biperiodic structure is a general term for a SWS composed of two geometries on alternating periods. A symmetric-biperiodic SWS is specifically a SWS with geometric period containing two translationally identical sections that occupy half the axial period, and are rotated (skew-symmetry), mirrored (reflection- or glide-symmetry), or both. There are generally two axial regions of electron interaction (two gaps) for each geometric period. Examples of symmetric-biperiodic structures include staggered-ladder coupled-cavity SWS's, and ring-bar circuits with symmetrically placed support rods.

By the analysis of Crepeau and McIsaac [135], it is evident that structures exhibiting skew- or reflection-symmetry support "fields with the symmetry of the structure", meaning that the structure's geometric symmetry influences the symmetric shape of the electromagnetic field. Therefore, in addition to the periodic nature of the fields over the full geometric period (with some slowly-varying complex phase multiplier), the fields are periodic in a rotated, or mirrored sense across the half-period of a biperiodic structure (with some related slowly-varying complex phase multiplier). In terms of periodic field-solution, this analysis precisely states what we sometimes take advantage of in symmetric-biperiodic structures, that the phase-advance across half a structure-period is half the phase-advance across the whole geometric-period, and the fields in each half-section are identical, modulo the complex half-phase-advance multiplier, and a rotation or reflection. There are a few complexities that arise due to the mapping of the geometric-period phase advance $\phi_{whole-period} \in [0, 2\pi]$ to the half-period phase advance

$\phi_{half-period} \in [0, \pi]$ that will be discussed in some detail in order to understand how the fields behave and the electron beam will interact.

We present an example of a biperiodic coupled-cavity structure with both skew and reflection symmetry. The geometry presented in Figure II - 1 (a) is biperiodic with both symmetries, and the geometry in (b) illustrates the half-period geometry of this SWS. The master and slave boundaries for each simulation geometry have a coordinate system to define the orientation of the periodicity and to match the geometry and finite-element mesh appropriately. In the case of the full geometric period, the coordinate systems are in-line with each-other and are axially shifted versions of the *x*-*y* coordinate systems pictured. In the case of the half-period simulation, there are two options for coordinate system orientation owing to the two, different symmetries of the structure – these are illustrated in Figure II - 2 (a) and (b). The concept of applying a rotated or mirrored matching boundary, although conceptually simple, is only rigorously defined through the analysis of Crepeau and McIsaac. However, once the matching surface is applied and the fields are matched by definition, further implications can be

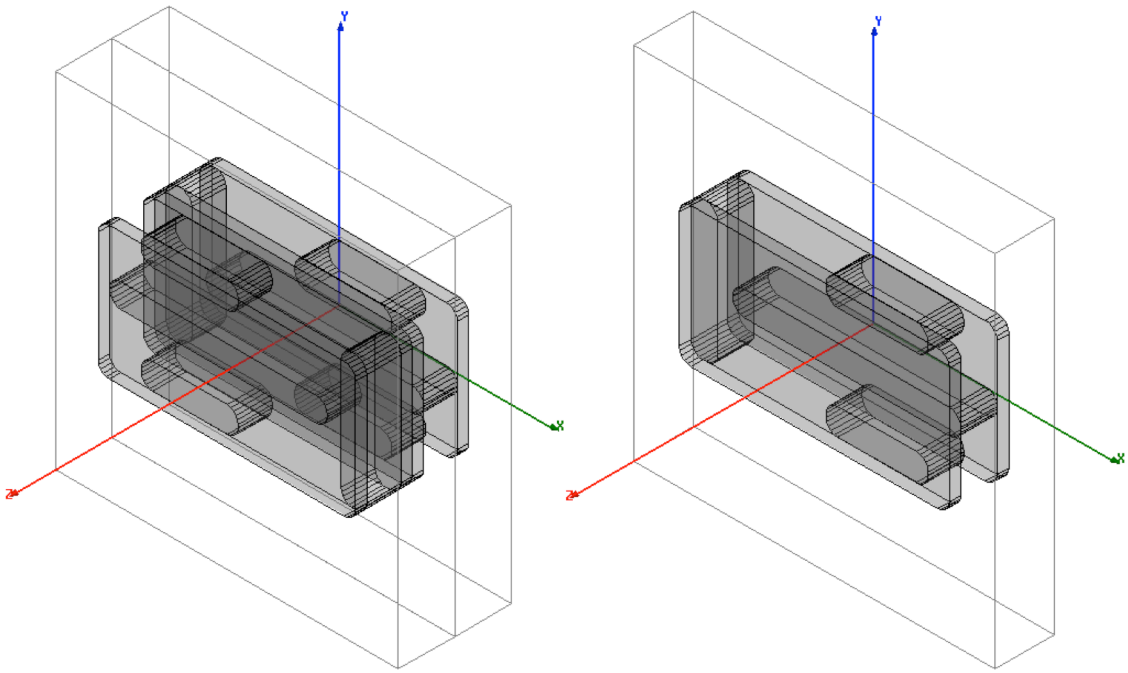

Figure II - 1: Symmetric-Biperiodic SWS geometry presented as the full-period **(a)** and half-period **(b)** for use in eigenmode simulations. The outer, bounding box is assigned the material of copper with finite, copper conductivity, and the simulation domain lies within the vacuum objects, which define the interior of the SWS. The *z*-axis is the periodic axial direction; with the two square faces perpendicular to it assigned matching boundaries.

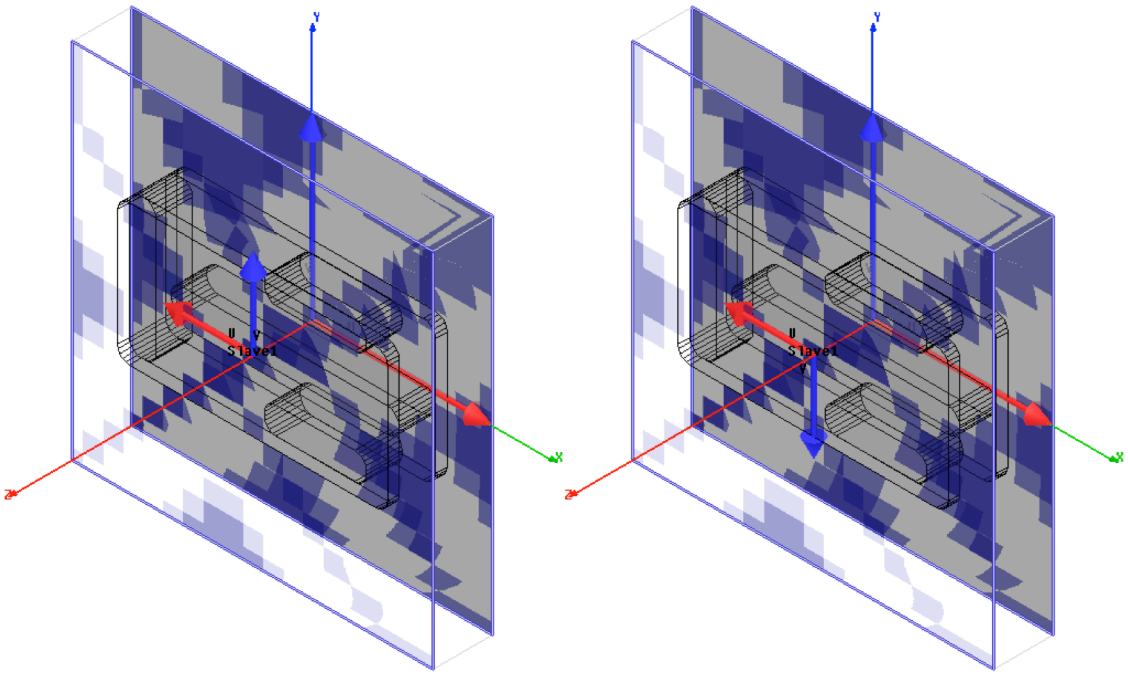

Figure II - 2: Half-period simulations of a symmetric-biperiodic SWS, showing two different, correct orientations of matching coordinate systems on opposing faces – **(a)** reflection-symmetry, **(b)** rotation-symmetry. Some symmetric-biperiodic structures would only allow one symmetry or the other.

investigated, as follows.

Although both [135] and [148] suggest that only a fraction of this multiplicity need to be retained in the final dispersion diagrams, this is not entirely true for our applications. The predominant reason that both sets of authors reduce the number of solutions is to observe where modes cross and where the crossing is avoided due to the symmetries (which is of minimal concern for us because this is explicitly calculated within the eigenmode simulations). Crepeau and McIsaac [135] make a point of stating that only certain spatial harmonics are non-zero on-axis due to the symmetries, but we are concerned about off-axis interaction with higher modes, which have finite off-axis interaction for all spatial-harmonics (and can be numerically evaluated within the field solutions of the simulation software).

However, the important point for our application is to characterize the structure within the standard framework of a coupled-cavity circuit. The conventional method of referring to the interaction fields in a coupled-cavity circuit is by dividing the unit cell into one interaction gap – both in the fields, and in a circuit representation of the structure. Therefore to create a

dispersion diagram and interaction impedance appropriate for one interaction gap, we must investigate the properties of a two-period structure and ascertain how to proceed.

The essential calculation for determining interaction of an arbitrary electron beam with a given mode of the SWS is the calculation of the appropriate spatial harmonic of the axial electric field (i.e. finding the Fourier components of equation A.1). For a single-period this calculation is conventionally written as

$$E_{zn} = \left| \frac{1}{L} \int_{z=0}^{z=L} E_z(z) e^{i\beta_n z} dz \right| \qquad \text{(II.2)}$$

where *L* is the period, $\beta_n = \beta_0 + \frac{2\pi n}{L}$ is the nth axial wavenumber for the corresponding spatial harmonic. However, with two periods and two phases, the correspondence between the *n*th spatial harmonic of a single and double period comes into question. Accordingly, for a single cavity period we use variables L_1 and φ_1, such that $\varphi_1 = \beta L_1$. Then for a doubly-periodic structure such that $L_2 = 2L_1$, implies the earlier suggested relation for phase that $\varphi_2 = \beta L_2 = 2\beta L_1 = 2\varphi_1$. Here we assume the physical notion that no matter how we divide the structure into periods, for a given frequency the wavenumber will be a constant. However, in the expansion of the dispersion diagram above we allowed the phase values from $\phi \in [\pi, 2\pi]$ to be obtained from a mirror-reflection of those values in $\phi \in [0, \pi]$, and some care must be taken.

In Figure II - 3 are representative dispersion diagrams for a single-period and a double-period structure. In the single-period structure, the dispersion is represented by the solid line, with a dashed-line representing a π-shifted version of the same dispersion, which is not necessarily physical. In the double-period structure, the dispersion stretches the π-point out to 2π, and folds the data back onto the range from zero to 2π – both of the visible modes are physical in a biperiodic structure and constitute the multiplicity of modes that was mentioned earlier. The symmetry of a biperiodic structure may imply that some of these modes interact less with an electron beam, and can therefore be represented by the dispersion diagram on the left with the less-important modes removed.

From these two diagrams, it can be seen that to construct the single-period diagram from the double-period diagram with values in the first Brillouin zone ($\phi_2 \in [0, \pi]$) we must use the first two modes to create the data in $\phi_1 \in [0, \pi]$. Furthermore, although the data in the second

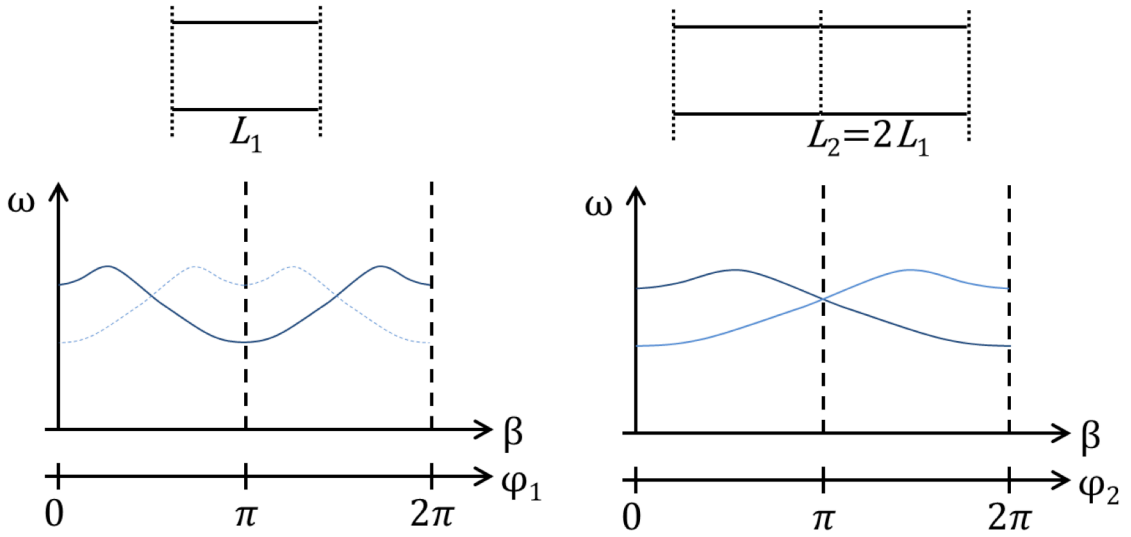

Figure II - 3: Dispersion comparison for a single period and a double period of a generic slow-wave structure. (a) Single-period dispersion – solid line is dispersion, dashed line is for reference. (b) Double-period dispersion – both lines are the dispersion.

mode map linearly from $\phi_2 \in [0,\pi]$ to $\phi_1 \in [0,\pi/2]$, the data in the first mode require a reversed linear transformation to map from $\phi_2 \in [0,\pi]$ to $\phi_1 \in [\pi/2,\pi]$.

The wavenumber for a single cavity period for the *n*th spatial harmonic is expressed as:

$$\beta_{n_1} = \beta_{1,0} + \frac{2\pi n_1}{L_1}$$

$$= \frac{\varphi_{1,0}}{L_1} + \frac{2\pi n_1}{L_1} \qquad \text{(II.3)}$$

where n_1 is the *n*th spatial harmonic according to the single-cavity period, and $\varphi_{1,0}$ is the phase seen in the first Brillouin zone. Similar expressions can be developed for the double-cavity period geometry, and equating β_{n_1} with β_{n_2} and $\beta_{1,0} = \beta_{2,0}$ (which is true for half the values in the first Brillouin zone that are not reversed in orientation) would imply

$$\frac{n_1}{L_1} = \frac{n_2}{L_2} \qquad \text{(II.4)}$$

$$n_1 = \frac{n_2}{2} \qquad \text{(II.5)}$$

Therefore, of the half of all doubly-periodic modes in the first Brillouin zone that map linearly, only those that have n_2 even will have a strong interaction with the electron beam. Similarly, for

the other half of values in the first Brillouin zone, we equate β_{n_1} with $\left(\beta_{n_2}+\frac{\pi}{L_2}\right)$ and $\beta_{1,0}=\frac{\pi}{L_1}-\beta_{2,0}$, which leads to the relations

$$\frac{n_1}{L_1}=\frac{n_2-1}{L_2} \tag{II.6}$$

$$n_1=\frac{n_2-1}{2} \tag{II.7}$$

This implies that for the half of all doubly-periodic modes that are mapped in a reverse linear fashion, only those that have n_2 odd will have a strong interaction with the electron beam. The determination of whether n_2 even or odd is retained in the single-cavity characterization is dependent on the shape of the fields [135], and we will see in examples how this is handled.

The one last general point about biperiodic structures, is that once this correlation has been made of the harmonics in a doubly-periodic structure and a singly-periodic structure, that the calculated electric field Fourier components are identical.

$$E_{zn_1}=\left|\frac{1}{L_1}\int_{z=0}^{z=L_1}E_z(z)e^{i\beta_{n_1}z}dz\right| \tag{II.8}$$

$$E_{zn_2}=\left|\frac{1}{L_2}\int_{z=0}^{z=L_2}E_z(z)e^{i\beta_{n_2}z}dz\right| \tag{II.9}$$

Taking note of the fact that the quantity $E_z(z)e^{i\beta_{n_2}z}$ is periodic with period L_1 by the symmetry of the structure, produces the result that the double-period integral is twice the value of the single-period integral. Dividing by the appropriate length yields equal Fourier components.

Implications of Reflection Symmetry

Reflection symmetry requires that the fields on the master (z=0) and slave (z=L_1) surfaces match modulo a complex phase constant, $e^{j\phi_1}=e^{j\beta L_1}$, and the field profile and orientation are mirrored across the *y*-*z* plane. The first, obvious implication is that the fields at the next half-period (z=2L_1) will match the fields on the master face modulo $e^{j2\phi_1}=e^{j2\beta L_1}$, and the field profile and orientation are identical to that on the master face. This implies the correct periodicity of the full geometry, but the fact that the field shape "matches" (under mirror-symmetry) at this half-period surface is only proven through the referenced analysis.

Due to the boundary conditions we can make several statements about the fields within the full-period geometry. If the full-period is divided into two half-periods, the fields in the second half-period are a mirrored, axially shifted (by length L_1), time-delayed (by electrical phase ϕ_1) replica of the fields in the first half-period. Therefore, the time-averaged field interaction that a beam experiences as it traverses a full-period is symmetric across the reflection plane even if the structure is not symmetric across this plane. Also, following the same analysis as in [144], [83], we find that, in a lossless structure, for a given power transmitted across a terminal plane, the stored energy in a single half-period is equally split between electrical and magnetic stored energy, and is equal to the stored energy in an adjacent half-period. Therefore, the group velocity can be calculated identically to a full-period structure:

$$\begin{aligned} v_g &= \frac{d\omega}{d\beta} = \frac{P}{\left(W_{m1} + W_{e1}\right)/L_1} \\ &= \frac{P}{\left(2W_{m1} + 2W_{e1}\right)/2L_1} \\ &= \frac{P}{\left(W_{m2} + W_{e2}\right)/L_2} \end{aligned} \qquad \text{(II.10)}$$

Further, a multiplicity of the dispersion characteristics is suggested by the phase conditions enforced on the matching boundaries. That is, for example, the π phase advance for a half-period will appear like a 2π (or zero) phase advance for the whole-period geometry – which means that both the points for zero and π phase advance for a half-period will map to the point for zero phase advance for the whole-period geometry. This is explained in detail in [135], [148], for which we find that the relevant interaction modes are determined by the even or odd character of the field-profile. This will be best understood through an example in the following sections.

Implications of Skew Symmetry

Skew or rotation-translation symmetry requires that the fields on the master (z=0) and slave (z=L_1) surfaces match modulo a complex phase constant, $e^{j\phi_1} = e^{j\beta L_1}$, and the field profile and orientation are rotated 180° around the z-axis. The first, obvious implication is that the fields at the next half-period (z=2L_1) will match the fields on the master face modulo $e^{j2\phi_1} = e^{j2\beta L_1}$, and the field profile and orientation are identical to that on the master face. This implies the correct

periodicity of the full geometry, but the fact that the field shape "matches" (under rotation-symmetry) at this half-period surface is only proven through the referenced analysis.

Due to the boundary conditions we can make several statements about the fields within the full-period geometry. If the full-period is divided into two half-periods, the fields in the second half-period are a rotated, axially shifted (by length L_1), time-delayed (by electrical phase ϕ_1) replica of the fields in the first half-period. Therefore, the time-averaged field interaction that a beam experiences as it traverses a full-period is identical 180° around the rotation axis. Also, following the same analysis as in [144], [83], we find that, in a lossless structure, for a given power transmitted across a terminal plane, the stored energy in a single half-period is equally split between electrical and magnetic stored energy, and is equal to the stored energy in an adjacent half-period. Therefore, the group velocity can be calculated in an identical manner.

Example of Matching Boundary Eigenmode Simulation for a Symmetric-Biperiodic SWS

As an example, we look at the 3-slot sheet-beam coupled-cavity slow-wave structure investigated throughout this thesis. An image of the simulation geometry (the vacuum interior) is presented in Figure II - 4 for a full geometric period with one of the matching boundary faces represented in purple. The eigenmode solution is calculated for values of phase advance φ[deg] = {1, 15, 30, 45, 60, 75, 90, 105, 120, 135, 150, 165, 179} predominantly evenly spaced between 0 and pi, but avoiding the "singularities" that occur at each of those points (those points are not traveling wave solutions, but standing waves). The raw data obtained for the first eight eigenmodes of each phase advance is presented Figure II - 5 (a). The individual points are connected with lines for all points at corresponding frequency ordering (*i.e.* all eigenmodes at the fifth lowest frequency are connected so that no two lines intersect). In order to identify the various modes across all phases we look at physical quantities relevant to each mode, such as attenuation, group velocity,

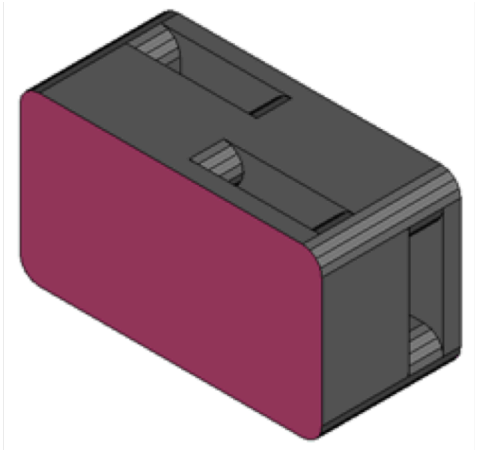

Figure II - 4: Simulated geometry for the example eigenmode simulations.

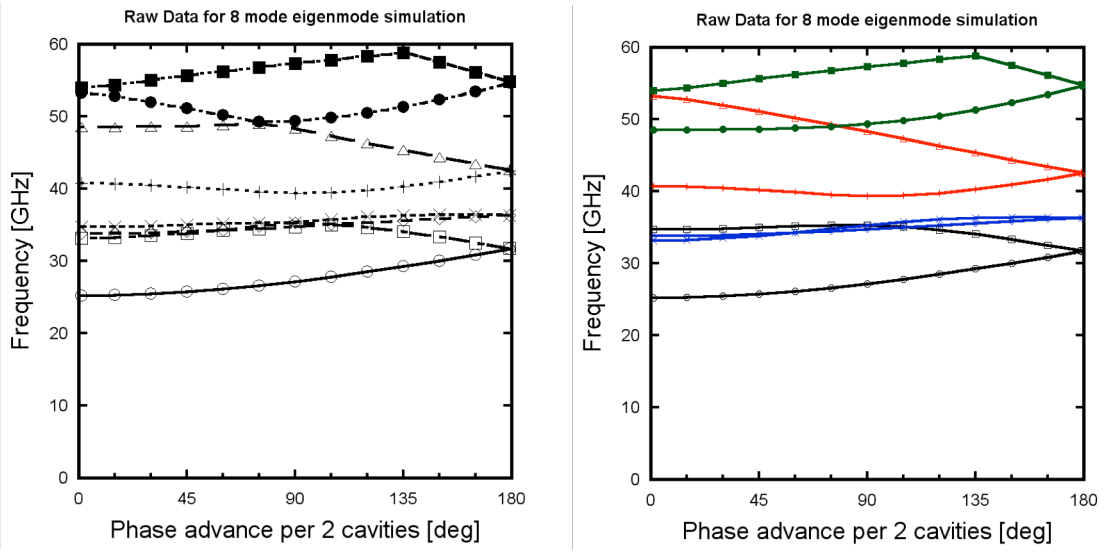

Figure II - 5: Dispersion data represented as frequency vs. phase advance specified between two planes of the two-cavity structure pictured in Figure II - 4. (a) Raw data. (b) Mode-identified data.

field components, and field derived quantities. The appropriately connected points are illustrated in Figure II - 5 (b). The result is a series of curves that appears smoothly connected with various crossings (the curves that cross are one symmetric and one antisymmetric curve – two symmetric curves never cross on this diagram, but have avoided crossings).

In order to find a full dispersion diagram that is within the conventional coupled-cavity interaction framework, we mirror the data from $\phi \in [0, \pi]$ to $\phi \in [\pi, 2\pi]$ and then duplicate the data with translational period $\phi_{translate} = 2\pi$. Finally, the data is converted to the phase that would be effected by a single cavity-period (a half geometry-period), with the data presented in Figure II - 6 in an expanded Brillouin Diagram including a dashed line representing the beam velocity for a 13.3kV electron beam. This plot represents all the modes supported by the structure that may interact with the electron beam. However, many of the modes have no interaction on-axis and, accordingly, do not have a strong interaction under most circumstances.

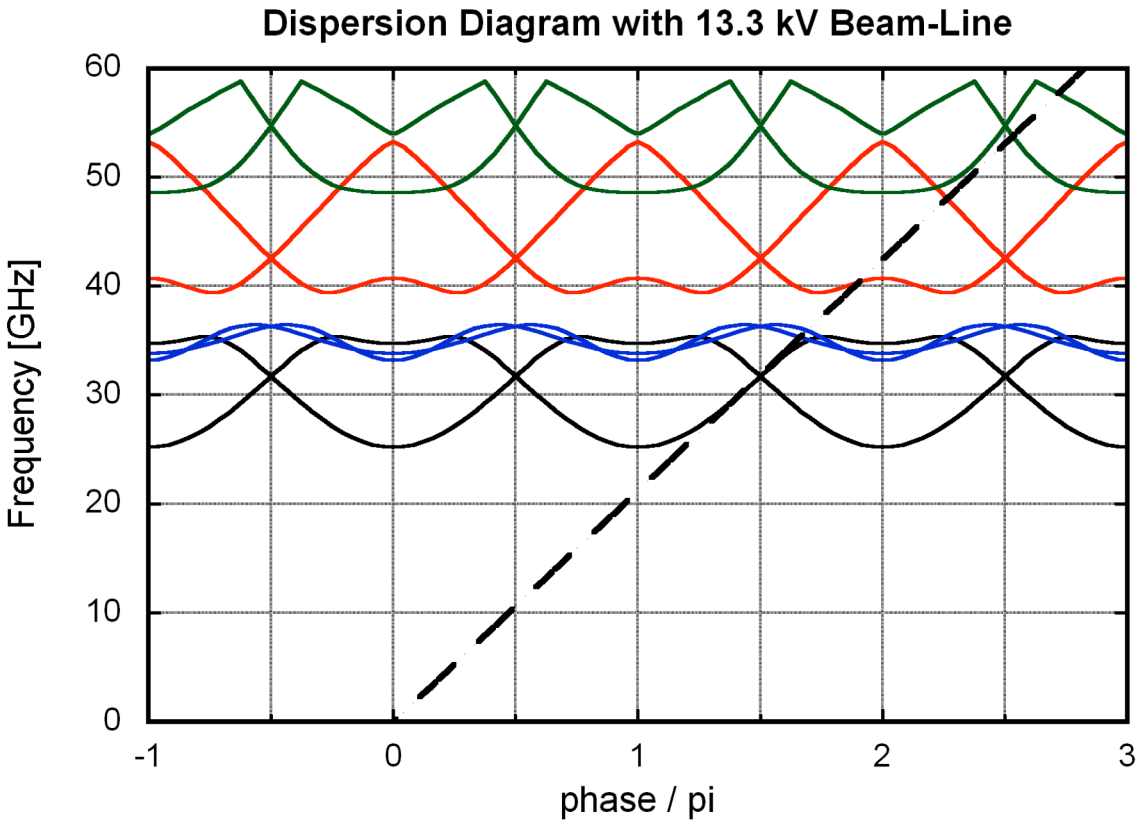

Figure II - 6: Expanded dispersion diagram.

We calculate the Fourier components of each mode on-axis, and display characteristic results of the fundamental mode in Figure II - 7. The values between $\phi \in [0, \pi/2]$ were calculated from the lowest double-period mode, while the values between $\phi \in [\pi/2, \pi]$ were calculated from the second mode. It was found that between $\phi \in [0, \pi/2]$ all the even values of spatial harmonic were zero (numerically small), and for the range $\phi \in [\pi/2, \pi]$ all the odd values of spatial harmonic were zero. Further, the values that match up from one side of 0.5π to the other confirm the previous analysis.

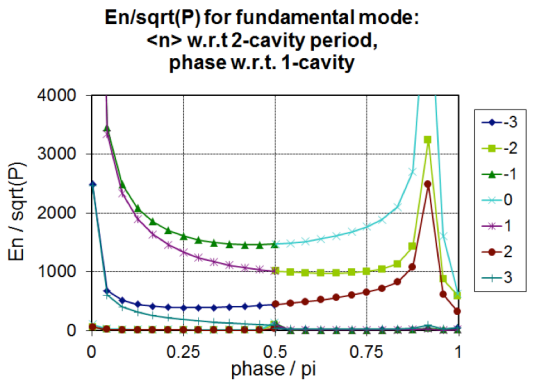

Figure II - 7: Spatial harmonics for the fundamental mode.

Finally, we develop a numbering scheme that works with the Fourier component calculation and apply it to the dispersion diagram for consistency (illustrated in Figure II - 8). Then all

the beam-line intersections can be assessed for the interaction strength. The dashed lines in the plot have zero interaction on-axis, and are of secondary importance in some regards. They are included for the full calculation of interactions, but not in the large-signal simulations of the forward wave interaction.

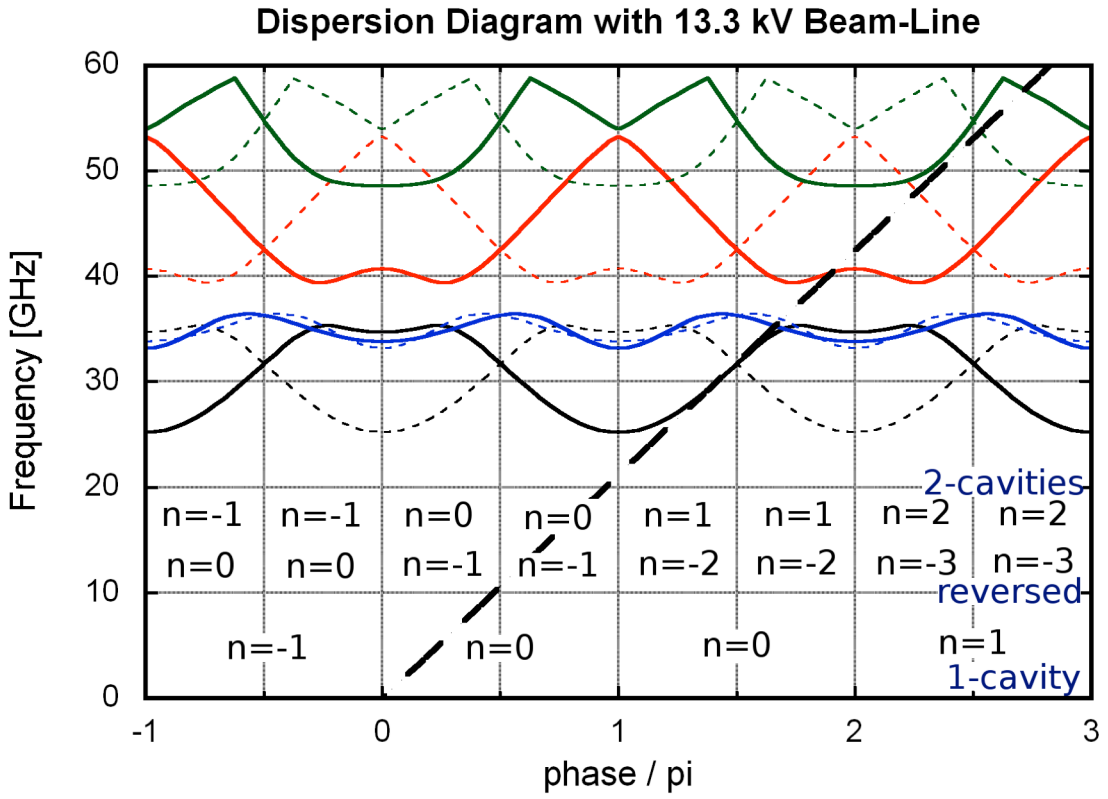

Figure II - 8: A spatial-harmonic labeled dispersion diagram for the structure of interest.

Appendix III: Intense Sheet Electron Beam Transport in a Periodically Cusped Magnetic Field

INTRODUCTION

Electron beams with large transverse aspect ratios (sheet-beams) are of interest for use in RF sources, accelerators, and free-electron laser applications. Focusing an intense, relatively low voltage (i.e. > 300 A/cm^2, ≤ 20 kV) sheet electron beam is difficult, and only solenoidal focusing over distances of several cm has been successfully used to date [27], [25], [93], [149]. If periodic permanent magnets could be used instead of a permanent magnet solenoid, the overall size and weight of the magnetic structure would be substantially reduced and transport over longer distances might become practical [24].

The electron beam that we wish to transport has the following parameters: beam current = 3.5 A, voltage = 19.5 kV, beam height = 0.3 mm, beam width = 4.0 mm. These are the same parameters achieved by Nguyen and Pasour et al. [27], [25] with strong permanent magnet solenoid focusing (8.5 kG), and this is a realizable gun at the voltages desired, and has been demonstrated [93]. This is a very strong magnetic field, as compared with the sheet-beam Brillioun Field calculated to be 1.5 kG.

The goal of this study is to find what measure of focusing is realizable for an intense sheet-beam with PCM focusing. To this end, we assume a beam tunnel within a slow-wave structure with outer dimension 7 mm (Figure III - 1 (a)). This provides a lower limit on the magnet spacing (Figure III - 1 (b)), and therefore a limit on the magnetic field intensity. The magnet period is similarly limited by materials and machining technology, and also affects the available field intensity within the beam tunnel. Here, we set the period at 12 mm and analyze the magnetic field using a finite-element magnetic field solver, Maxwell [81]. By adjusting the magnet height, we can easily produce the 1.5 kG Brillioun field within the beam tunnel region and go 20-30% beyond without saturating the

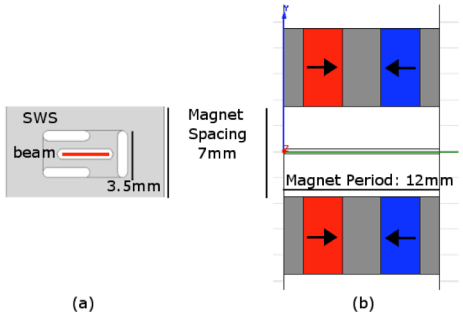

Figure III - 1: a) Generic Ka-Band sheet-beam slow-wave structure geometry (end view). b) 2D Magnet configuration with realistic dimensions (magnet period, magnet spacing) – arrows represent direction of magnet polarization (side view).

pole-pieces. However, the magnet period is dangerously large when considering PPM instability [24].

1-Dimension Analytical Focusing

An analytical, laminar sheet-beam that is infinite in the wide-dimension has a force equation [150],

$$y'' = K_y - k_{c0}{}^2 \left(b(z)\right)^2 y, \tag{III.1}$$

where K_y is a measure of the defocusing charge,

$$K_y = \frac{qJ}{2m\varepsilon_0 v_z}, \tag{III.2}$$

J is the current per unit width, k_{c0} is the cyclotron wavenumber,

$$k_{c0} = \frac{qB_{rms}}{mv_z}, \tag{III.3}$$

and $b(z)$ is the magnetic field shape with rms value of one.

The force equation can be solved numerically using a simple leap-frog integration and assuming an initial beam height. The results of a set of simulations with increasing magnetic field are included in Figure III - 2. Also marked are the analytical value for the Brillioun Magnetic-Field and the area of observed PPM instability.

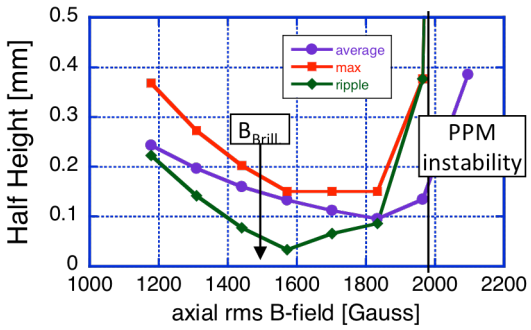

Figure III - 2: Results of 1D Numerical PPM Transport

2-D MICHELLE Simulations

A set of 2D beam-optics simulations were performed using the finite-element code MICHELLE [118]. The 2D magnetic field was produced using realistic magnetic materials in the finite-element magnetic field solver Maxwell [81], exported to a table, and scaled linearly in magnitude within MICHELLE. The electron beam used in these initial simulations is an artificial beam created from a non-convergent gun with nearly constant beam-height (both laminar and

"thermal" emission models were tested). The beam is transported through a straight 4 cm-long section of a flat beam-tunnel of nominal Ka-band size (specifically 0.9 mm tall). Note that this propagation distance is only 3.3 periods long, so a steady-state solution is not achieved. However, this distance is sufficient for the Ka-band circuit we envision.

The 2D results presented in Figure III - 3 are very similar to the predicted 1D results in terms of the shape near the Brillioun-field value, and also in the appearance of a PPM instability at approximately the same magnetic field value. The particle trajectories (not pictured here) also indicate the PPM instability for larger magnetic fields, as they exhibit a growing beam scallop with a period close to the magnetic field period.

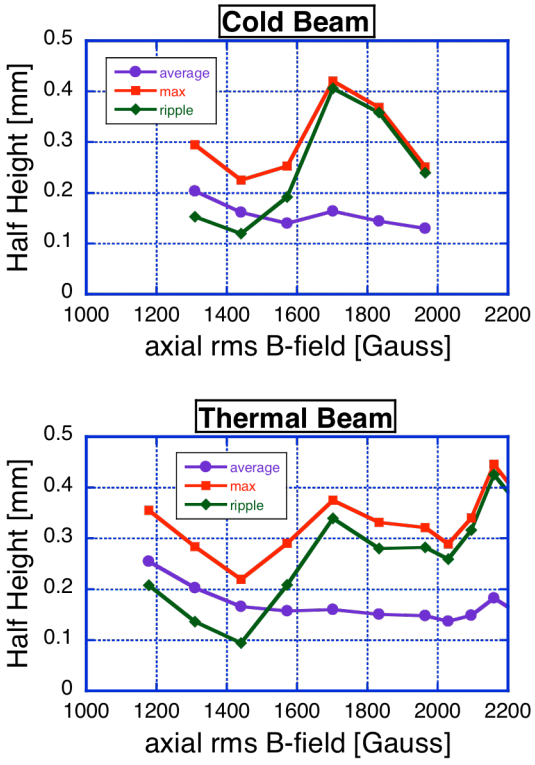

Figure III - 3: Results of MICHELLE 2D PPM transport simulations with scaled 2D magnetic fields – infinite sheet beam approximation. a) Cold (laminar) Beam. b) Thermally-emitted Beam.

3-D MICHELLE Simulations – Laminar Beam

A series of 3D beam-optics simulations were performed with MICHELLE – the simplest using a laminar, elliptical beam, created numerically to fully account for the space charge depression of the beam. The beam is propagated through a straight rectangular beam-tunnel of dimension 0.9 mm x 5.0 mm. The 3D magnetic field is created with the 3D capabilities of the Maxwell field solver – both periodic boundaries and a realistic, finite stack of periodic magnets were used with agreement between methods.

The initial 3D simulations were accomplished with minimal side-focusing (or none – as the extrusion of the 2D magnetic field solution) with currents measured vs. rms magnetic field strength plotted in Figure III - 4. The currents represent a measure of how well the beam is transported and whether the fractions of the beam lost is collected on the top and bottom (wide surfaces), or the left and right sides (short surfaces). For small magnetic field, the beam quickly expands into the top/bottom due to space-charge. As the magnetic field increases the beam is better confined in the short-dimension (as predicted by 1D and 2D analyses), but shears

quickly into the side-walls. It can be seen that the optimum field is near the predicted Brillioun field, but is somewhat smaller.

Focusing in the wide-dimension is accomplished by alternately offsetting the pole-pieces as suggested by Booske et al. [24]. Simulations with an "infinite" periodic stack were accomplished with magnetic symmetry boundaries, and injecting a laminar (shielded) beam into the periodic field.

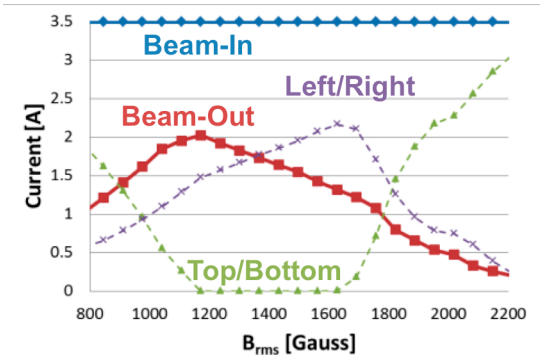

Figure III - 4: Beam-Interception results of MICHELLE PPM transport simulations with scaled 2D magnetic fields extruded from 2D field solution – no side-focusing fields.

Creating a uniformly periodic magnetic field with finite length and magnetically shielded gun-region required some adjustments to the magnet strengths (*e.g.,* by adjusting the heights of individual magnets) and monitoring the magnetic field components on axis and at the beam edges and corners. These full 3D magnetic simulations were evaluated with both linear and nonlinear materials to assess the realities of saturation within the pole-pieces. We found that realistically a 12 mm period PCM would produce the required Brillioun field on axis without saturating, but that a 10 mm period PCM would saturate before producing the required magnetic field for the given magnet-spacing (refer to Figure III - 1 for geometry). This determined the lower-limit on magnet period for this study.

The results from a series of 3D beam-optics simulations with varying rms axial magnetic field strength are illustrated in Figure III - 5. The key result of this plot is the depiction of a range of magnetic field strengths over which the entire beam is transported successfully, indicating that the side-focusing is successful. Unfortunately, the side-focusing (the y-component of the magnetic field) is linearly scaled along with the dominant focusing of the beam (the x-component of the magnetic field), so for increasing values of magnetic field, the beam becomes over-focused in the wide-dimension and becomes less sheet-like. The other

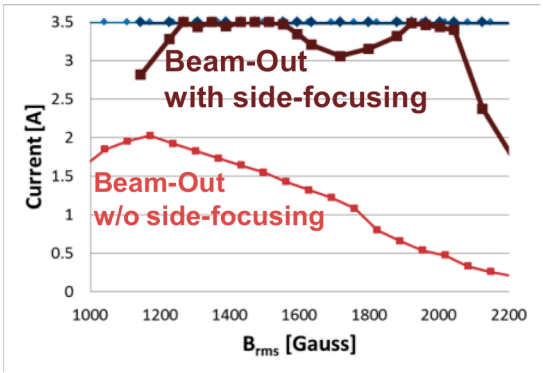

Figure III - 5: Results of MICHELLE PPM transport simulations with scaled 3D magnetic fields, both with and without side-focusing fields.

point to observe from this plot is that, similar to the 2D-field/3D-beam case above, the optimal solution occurs somewhat below the Brillioun-field value. This is likely the result of the distortion of the sheet-beam during transport.

3-D MICHELLE Simulations – Available Gun

As a case with a slightly more realistic thermal sheet-electron beam, we used the electron gun designed by Nguyen [25] for the electron source. The original design for this gun intended for very strong solenoidal focusing, which worked very well at capturing the thermal beam (98% transport demonstrated [93]). However, as we see from simulations, the thermal emittance is quite large due in part to the large beam convergence. For realistic magnetic fields optimized to this beam, the best PCM transport achieved thus far was 83% for the 4 cm transport section.

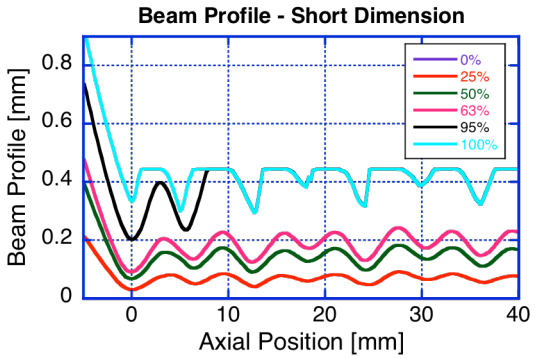

Figure III - 6: Beam-height profiles vs. axial position for the thermal gun of Nguyen with PPM focusing fields.

Bibliography

[1] Robert J Barker, John H Booske, Neville C Luhman, and Gregory S Nusinovich, *Modern Microwave and Millimeter-Wave Power Electronics*. Piscatway, NJ: Wiley-Interscience, 2005.

[2] A. S. Gilmour, *Principles of Traveling Wave Tubes*. Print on Demand: Artech House, 1994.

[3] B. Levush et al., "Vacuum electronics: status and trends," *IEEE Radar Conference 2007*, pp. 971-976, 2007.

[4] J.F. Gittins, *Power travelling-wave tubes*. New York: Elsevier, 1965.

[5] J.R. Pierce, *Traveling-Wave Tubes*. New York, NY: D. Van Nostrand Co., Inc., 1950.

[6] J.R. Legarra, J. Cusick, R. Begum, P. Kolda, and M. Cascone, "A 500-W coupled-cavity TWT for Ka-band communication," *IEEE Trans. on Electron Devices, Vol. 52, No. 5*, pp. 665-668, 2005.

[7] L-3 Communications ETI. (2008) 8909H TWT Datasheet. [Online]. http://www.l-3com.com/eti/downloads/8909H.pdf

[8] L-3 Communications. (2011) Millimeter Wave Power Module Data sheet. [Online]. http://www.l-3com.com/edd/pdfs/13000509.pdf

[9] A. Laurent, P. Nugues, T. Beck, and D. Henry, "Wideband high efficiency compact TWTs," in *IEEE Intl. Vacuum Electronic Conference*, Monterey, CA, 2002, pp. 178-179.

[10] L-3 Communications ETI. (2008, April) 8928H datasheet. [Online]. http://www.l-3com.com/eti/downloads/military/8928H.pdf

[11] L-3 Communications ETI. (2008, March) 8929H datasheet. [Online]. http://www.l-3com.com/eti/downloads/military/8929H.pdf

[12] R.L. Ives, L.R. Falce, G. Miram, and G. Collins, "Controlled-Porosity Cathodes for High-Current-Density Applications," *IEEE Transactions on Plasma Science*, vol. 38, no. 6, pp. 1345-1353, June 2010.

[13] G. S. Nusinovich, B. Levush, and D. K. Abe, "A Review of the Development of Multiple-Beam Klystrons and TWTs," US Naval Research Laboratory, Washington, DC, Memorandum Report NRL/MR/6840--03-8673, 2003.

[14] E. A. Gelvich et al., "The new generation of high-power multiple-beam klystrons," *IEEE-MTT*, vol. 41, no. 1, pp. 15-19, January 1993.

[15] C. Bearzatto, A. Beunas, and G. Faillon, "Long pulse and large bandwidth multibeam klystron," in *AIP Conf. Proc. 474*, Pajaro Dunes, CA, 1998, pp. 107-116.

[16] D. Yaogen, "Recent progress on L-band broadband MBK," in *3rd IEEE Intl. Vacuum Electronics Conference*, Monterey, CA, 2002, pp. 296-297.

[17] D. K. Abe et al., "Demonstration of an S-band, 600-kW fundamental-mode multiple-beam

klystron," *IEEE Electron Device Letters*, vol. 26, no. 8, pp. 590-592, Aug 2005.

[18] A. A. Borisov et al., "The development of vacuum microwave devices in Istok," in *IEEE Intl. Vacuum Electronics Conference*, Bangalore, IND, 2011, pp. 437-438.

[19] M. Basten et al., "A multiple electron beam array for a 220 GHz amplifier," in *IEEE Intl. Vacuum Electronic Conference*, Rome, IT, 2009, p. 110.

[20] K. Nguyen et al., "1.4: Design of a high-gain wideband high-power 220-GHz multiple-beam serpentine TWT," in *IEEE Intl. Vacuum Electronics Conference*, Monterey, CA, 2010, pp. 23-24.

[21] P. Ferguson, "Development of a 10 MW hollow beam klystron," in *IEEE Intl. Conference on Plasma Science*, Karlsruhe, GER, 2008, p. 1.

[22] W. Beaver, G. Caryotakis, G. Huffman, and N. Taylor, "An experimental wide-band klystron, employing a high perveance hollow beam," in *Intl. Electron Devices Meeting*, Washington, DC, 1959, p. 72.

[23] A.V. Galdetskiy, "8.2: On the opportunity of self-oscillation in sheet beam devices," in *IEEE Intl. Vacuum Electronics Conference*, Monterey, CA, 2010, pp. 95-96.

[24] J. H. Booske, B. D. McVey, and T. M. Antonsen, "Stability and confinement of nonrelativistic sheet electron beams with periodic cusped magnetic focusing," *Journal of Applied Physics*, vol. 73, no. 9, pp. 4140-4155, May 1993.

[25] K.T. Nguyen, J. Pasour, E.L. Wright, J. Petillo, and B. Levush, "High-perveance W-band sheet-beam electron gun design," *IEEE International Vacuum Electronics Conference*, pp. 179 - 180, 2008.

[26] J. Pasour et al., "Sheet beam stick for low-voltage W-band extended interaction klystron (EIK)," *IEEE International Vacuum Electronics Conference (IVEC)*, pp. 43 - 44, 2010.

[27] K. T. Nguyen, J. A. Pasour, T. M. Antonsen Jr., and P. B. Larsen, "Intense Sheet Electron Beam Transport in a Uniform Solenoidal Magnetic Field," *IEEE Transactions on Electron Devices*, vol. 56, no. 5, pp. 744-752, May 2009.

[28] B. E. Carlsten, "Modal analysis and gain calculations for a sheet electron beam in a ridged waveguide slow-wave structure," *Physics of Plasmas*, vol. 9, no. 12, p. 5088, August 2002.

[29] S. J. Papadakis et al., "A micro-fabricated sheet-beam Orotron THz source," in *Proc. SPIE Micro- and Nanotechnology Sensors, Systems and Applications III*, Orlando, FL, 2011, p. 8031.

[30] G. Scheitrum, "Design and Construction of a W-band Sheet Beam Klystron," in *AIP Conference Proceedings Vol. 807*, 2006, pp. 120-125.

[31] D. Sprehn et al., "Development of a 10 MW Sheet Beam Klystron for the ILC," in *Particle Accelerator Conference*, Vancouver, BC, CAN, 2009.

[32] G. Scheitrum et al., "W-band Sheet Beam Klystron Research at SLAC," in *IEEE Intl. Vacuum Electronics Conference*, Monterey, CA, 2006, pp. 481-482.

[33] G. Scheitrum et al., "W-band sheet beam klystron design," in *Intl. Infrared and Millimeter Waves Conference*, Karlsruhe, GER, 2004, pp. 525-526.

[34] G. Scheitrum et al., "Fabrication and Testing of a W-band Sheet Beam Klystron," in *IEEE Intl. Vacuum Electronics Conference*, Kitakyushu, JAP, 2007, pp. 1-2.

[35] M. Cusick et al., "X-Band Sheet Beam Klystron (XSBK)," in *IEEE Intl. Vacuum Electronics Conference*, Rome, ITA, 2009, pp. 296-297.

[36] B.E. Carlsten et al., "Technology development for a mm-wave sheet-beam traveling-wave tube," *IEEE Transactions on Plasma Science*, vol. 33, no. 1, pp. 85-93, February 2005.

[37] S. Humphries, S. Russell, B. Carlsten, and L. Earley, "Focusing of high-perveance planar electron beams in a miniature wiggler magnet array," *IEEE Transactions on Plasma Science*, vol. 33, no. 2, pp. 882-891, April 2005.

[38] Steven J. Russell, Zhi-Fu Wang, W. Brian Haynes, Bruce E. Carlsten, and Lawrence M. Earley, "Optical beam profile diagnostic for low energy, long pulse, moderate current electron beams," *Review of Scientific Instruments*, vol. 77, no. 3, pp. 033302-033302-7, March 2006.

[39] L.M. Earley et al., "Simulation and Measurement of the Los Alamos 94GHz TWT RF Structure," in *IEEE Intl. Vacuum Electronics Conference*, Monterey, CA, 2006, pp. 449-450.

[40] B.E. Carlsten et al., "MM-wave sheet-beam traveling-wave tube development at Los Alamos," in *IEEE Intl. Conference on Plasma Science*, Baltimore, MD, 2004, p. 422.

[41] B.E. Carlsten et al., "MM-wave source development at Los Alamos," in *IEEE Intl. Vacuum Electronics Conference*, Monterey, CA, 2004, pp. 24-25.

[42] G.M. Borsuk and B. Levush, "PL-2: Vacuum electronics research perspective at the naval research laboratory," in *IEEE Intl. Vacuum Electronics Conference*, Monterey, CA, 2010, pp. 3-4.

[43] K.T. Nguyen et al., "Sheet-Beam 90 GHz and 220 GHz Extend-Interaction-Klystron Designs," in *IEEE Intl. Vacuum Electronics Conference*, Kitakyushu, JAP, 2007, pp. 1-2.

[44] J. Pasour, K. Nguyen, E. Wright, A. Balkcum, and B. Levush, "W-band sheet beam Extended Interaction Klystron (EIK)," in *IEEE Intl. Vacuum Electronics Conference*, Bangalore, IND, 2011, pp. 87-88.

[45] K.T. Nguyen, D.E. Pershing, D.K. Abe, G. Miram, and B. Levush, "Eighteen-beam gun design for high power, high repetition rate, broadband multiple-beam klystrons," *IEEE Transactions on Plasma Science*, vol. 33, no. 2, pp. 685-695, April 2005.

[46] K.T. Nguyen, D.E. Pershing, D.K. Abe, and B. Levush, "Bandwidth extension of an S-band, fundamental-mode eight-beam klystron," *IEEE Transactions on Plasma Science*, vol. 34, no. 3, pp. 576-583, June 2006.

[47] D.K. Abe et al., "Experimental Study and Analysis of an S-Band Multiple-Beam Klystron With 6% Bandwidth," *IEEE Transactions on Electron Devices*, vol. 56, no. 5, pp. 846-854, May 2009.

[48] D.K. Abe et al., "Experimental demonstration of MBK2, an eight-beam, five-cavity multiple-beam klystron," in *IEEE Intl. Vacuum Electronics Conference*, Monterey, CA, 2008, pp. 423-424.

[49] K.T. Nguyen et al., "High-average power broadband 18-beam klystron circuit and collector designs," in *IEEE Intl. Vacuum Electronics Conference*, Monterey, CA, 2008, pp. 425-426.

[50] K.T. Nguyen et al., "Broadband High-Power 18-Beam S-Band Klystron Amplifier Design," *IEEE Transactions on Electron Devices*, vol. 56, no. 5, pp. 883-890, May 2009.

[51] T.M. Antonsen, S.J. Cooke, B. Levush, and Y.N. Pchelnikov, "Axial vs Transverse Bunching in Sheet Beam TWTs," in *IEEE Intl. Vacuum Electronics Conference*, Monterey, CA, 2006, pp. 483-484.

[52] D. Chernin et al., "Linearity of the Transverse Field Interaction in a Traveling Wave Tube," in *IEEE Intl. Vacuum Electronics Conference*, Monterey, CA, 2006, pp. 27-28.

[53] D. Chernin, T.M. Antonsen, B. Levush, S.J. Cooke, and W. Manheimer, "A Comparison of Linearity and Efficiency in Conventional and Transverse TWT Amplifiers," *IEEE Transactions on Electron Devices*, vol. 54, no. 2, pp. 194-201, February 2007.

[54] S.J. Cooke, B. Levush, and T.M. Antonsen, "8.1: Nonlinear characteristics of transverse interaction in sheet beam amplifiers," in *IEEE Intl. Vacuum Electronics Conference*, Monterey, CA, 2010, pp. 93-94.

[55] Young-Min Shin, A. Baig, D. Gamzina, and N.C. Luhmann, "9.4: MEMS fabrication of 0.22 THz sheet beam TWT circuit," in *IEEE Intl. Vacuum Electronics Conference*, Monterey, CA, 2010, pp. 185-186.

[56] A. Baig et al., "Experimental characterization of LIGA fabricated 0.22 THz TWT circuits," in *IEEE Intl. Vacuum Electronics Conference*, Bangalore, IND, 2011, pp. 275-276.

[57] Young-Min Shin et al., "Micro-fabricable terahertz sheet beam amplifier integrated with broadband metamaterial circuit," in *Intl. Conference on Communications and Electronics*, 2010, pp. 373-378.

[58] Young-Min Shin, L.R. Barnett, A. Baig, Wen-Ching Tsai, and N.C. Luhmann, "0.22 THz sheet beam TWT amplifier: System design and analysis," in *IEEE Intl. Vacuum Electronics Conference*, Bangalore, IND, 2011, pp. 61-62.

[59] Young-Min Shin, L.R. Barnett, and N.C. Luhmann, "Phase-Shifted Traveling-Wave-Tube Circuit for Ultrawideband High-Power Submillimeter-Wave Generation," *IEEE Transactions on Electron Devices*, vol. 56, no. 5, pp. 706-712, May 2009.

[60] Young-Min Shin and Larry R. Barnett, "Intense wideband terahertz amplification using phase shifted periodic electron-plasmon coupling," *Applied Physics Letters*, vol. 92, no. 9, pp. 091501-091501-3, March 2008.

[61] Chiping Chen, R. Bhatt, A. Radovinsky, and Jing Zhou, "Three-Dimensional Design of a Non-Axisymmetric Periodic Permanent Magnet Focusing System," in *Proceedings of the Particle Accelerator Conference*, Knoxville, TN, 2005, pp. 1964-1966.

[62] R. Bhatt, T. Bemis, and C. Chen, "Three-dimensional theory and simulation of nonrelativistic elliptic electron and ion beam generation," *IEEE Transactions on Plasma Science*, vol. 34, no. 2, pp. 187-193, April 2006.

[63] R. C. Davidson, P. Stoltz, and C. Chen, "Intense non-neutral beam propagation in a periodic solenoidal field using a macroscopic fluid model with zero thermal emittance," *Physics of Plasmas*, vol. 4, no. 10, p. 3710, July 1997.

[64] R. Bhatt, J. Zhou, and C. Chen, "Three Dimensional Simulation of Large-Aspect-Ratio Ellipse-Shaped Charged-Particle Beam Propagation," in *Proceedings of the Particle Accelerator Conference*, Knoxville, TN, 2005, pp. 823-825.

[65] C. Chen and J. Zhou, "Equilibrium theory of an intense elliptic beam for high-power ribbon-beam klystron applications," in *IEEE Particle Accelerator Conference*, Albuquerque, NM, 2007, pp. 2316-2318.

[66] Young-Min Shin, L.R. Barnett, and N.C. Luhmann, "Numerical and experimental design study of quasi-optical multi-gap output cavity for W-band sheet beam klystron (WSBK)," in *IEEE Intl. Vacuum Electronics Conference*, Rome, ITA, 2009, pp. 530-532.

[67] Young-Min Shin, Jian-Xun Wang, L.R. Barnett, and N.C. Luhmann, "Particle-In-Cell Simulation Analysis of a Multicavity W-Band Sheet Beam Klystron," *IEEE Transactions on Electron Devices*, vol. 58, no. 1, pp. 251-258, January 2011.

[68] Xiaofeng Zhang et al., "X-Band sheet beam klystron design," in *IEEE Intl. Vacuum Electronics Conference*, Bangalore, IND, 2011, pp. 245-246.

[69] Cunjun Ruan, Shuzhong Wang, Ding Zhao, and Qinsheng Li, "Thermodynamics analysis of electron gun for sheet beam klystron," in *IEEE Intl. Vacuum Electronics Conference*, Rome, ITA, 2009, pp. 439-440.

[70] Wang Ruan et al., "P1–3: Cavity design for an X-band sheet beam klystron," in *IEEE Intl. Vacuum Electronics Conference*, Monterey, CA, 2010, pp. 105-106.

[71] Wang Ruan et al., "Interaction simulation of an X-band sheet beam klystron," in *IEEE Intl. Vacuum Electronics Conference*, Rome, ITA, 2009, pp. 304-305.

[72] Ding Zhao, Cunjun Ruan, Yong Wang, and Wang Ruan, "8.5: Numerical simulation and experimental test of a sheet beam electron gun," in *IEEE Intl. Vacuum Electronics Conference*, Monterey, CA, 2010, pp. 101-102.

[73] J. Tucek, M. Basten, D. Gallagher, and K. Kreischer, "1.2: Sub-millimeter and THz power amplifier development at northrop grumman," in *IEEE Intl. Vacuum Electronics Conference*, Monterey, CA, 2010, pp. 19-20.

[74] S.J. Cooke, B. Levush, and T.M., Jr. Antonsen, "A coupled-cavity slow-wave structure for sheet-beam devices," *IEEE Int. Vac. Elec. Conf.*, pp. 487-488, 2006.

[75] P.B. Larsen, D.K. Abe, S.J. Cooke, and B. Levush, "Characterization of a Ka-band sheet-beam coupled-cavity slow-wave structure," *IEEE Trans. on Plasma Sci.*, pp. 1244-1254, 2010.

[76] C.L. Kory, "Validation of an Accurate Three-Dimensional Helical Slow-Wave Circuit," NASA Contractor Report, 4766, 1997.

[77] C.L. Kory and J.A. Dayton, "Accurate Cold-Test Model of Helical TWT Slow-Wave Circuits," *IEEE Transactions on Electron Devices*, vol. 45, no. 4, pp. 966-971, April 1998.

[78] J.D. Wilson and C.L. Kory, "Simulation of cold test parameters and RF output power for a coupled-cavity traveling-wave tube," *IEEE Transactions on Electron Devices*, vol. 42, no. 11, pp. 2015-2020, November 1995.

[79] F. Kantrowitz and I. Tammaru, "Three-Dimensional Simulations of Frequency-Phase Measurements of Arbitrary Coupled-Cavity RF Circuits," *IEEE Transactions on Electron Devices*, vol. 35, no. 11, pp. 2018-2026, 1988.

[80] W.Q. Lei and Z.H. Yang, "Software Cold Test Simulation of Coupled Cavity Slow-Wave Structure in Millimieter Wave TWT," *Intl. Journal of Infrared and Millimeter Waves*, vol. 24, no. 1, pp. 71-77, January 2003.

[81] Ansoft Corporation, a subsidiary of Ansys Inc., , Pittsburgh, PA.

[82] STAAR Inc., a subsidiary of AWR, , El Segundo, CA.

[83] D. A. Watkins, *Topics in Electromagnetic Theory*. New York, U.S.: John Wiley & Sons, 1958.

[84] H. J. Curnow, "A general equivalent circuit for coupled-cavity structures," *IEEE Transactions on Microwave Theory and Techniques*, vol. 13, no. 5, pp. 671-676, 1965.

[85] R. G. Carter and L. Shunkang, "A method for calculating the properties of coupled-cavity slow-wave structures from their dimensions," *IEE Proceedings Pt. H*, vol. 133, no. 5, pp. 330-334, 1986.

[86] V. L. Christie, L. Kumar, and Balakrishnan N., "Improved equivalent circuit model of practical coupled-cavity slow-wave structures for TWTs," *Microwave and Optical Technology Letters*, vol. 35, no. 4, pp. 322-326, 2002.

[87] D. J. Connolly, "Determination of the interaction impedance of coupled cavity slow wave structures," *IEEE Transactions on Electron Devices*, vol. 23, no. 5, pp. 491-493, 1976.

[88] J. R. M. Vaughan, "Calculation of coupled-cavity TWT performance," *IEEE Transacations on Electron Devices*, vol. ED-22, no. 10, pp. 880-890, October 1975.

[89] A. W. Horsley and A. Pearson, "Measurement of dispersion and interaction impedance characteristics of slow-wave structures by resonance methods," *IEEE Transactions on Electron Devices*, vol. 13, no. 12, pp. 962-969, 1966.

[90] P. B. Larsen, D. K. Abe, B. Levush, and T. M. Antonsen, "Coupling a waveguide input into a sheet-beam coupled-cavity slow-wave structure," in *IEEE Intl. Vacuum Electronics Conference*, Bangalore, IND, 2011, pp. 209-210.

[91] Calabazas Creek Research, Inc., San Mateo, CA,.

[92] J. Legarra, Personal Communications, 2010.

[93] J. Pasour et al., "Demonstration of a 100-kW Solenoidally Focused Sheet Electron Beam for Millimeter Wave Amplifiers," *IEEE Transactions on Electron Devices*, vol. 57, no. 12, April 2011.

[94] Thomas M., Jr. Antonsen and Baruch Levush, "CHRISTINE: A Multifrequency Parametric Simulation Code for Traveling Wave Tube Amplifiers," US Naval Research Laboratory, Washington, DC, NRL/FR/6840--70-9845, 1997.

[95] B. N. Basu, *Electromagnetic theory and applications in beam-wave electronics*.: World Scientific, 1996.

[96] D.K. Abe, M.T. Ngo, B. Levush, T.M., Jr. Antonsen, and D. Chernin, "Experimental validation of CHRISTINE, a 1-D, multi-frequency helix TWT code: drive curves, phase, distortion products, and intermodulation," in *IEEE Intl. Conference on Plasma Science*, 1999, p. 136.

[97] D.K. Abe, B. Levush, T.M., Jr. Antonsen, D.R. Whaley, and B.G. Danly, "Design of a linear C-band helix TWT for digital communications experiments using the CHRISTINE suite of large-signal codes," *IEEE Transactions on Plasma Science*, vol. 30, no. 3, pp. 1053-1062, June 2002.

[98] T.A. Hargreaves et al., "Ku-band MPM booster helix TWT design and validation," in *IEEE Intl. Vacuum Electronics Conference*, Monterey, CA, 2004, pp. 293-294.

[99] J.H. Booske et al., "Accurate parametric modeling of folded waveguide circuits for millimeter-wave traveling wave tubes," *IEEE Transactions on Electron Devices*, vol. 52, no. 5, pp. 685-694, May 2005.

[100] S. Bhattacharjee et al., "Investigations of folded waveguide TWT oscillators for THz radiation," in *IEEE Intl. Conference on Vacuum Electronics*, Seoul, KOR, 2003, pp. 317-318.

[101] D. Chernin et al., "Large-Signal Multifrequency Simulation of Coupled-Cavity TWTs," *IEEE Transactions on Electron Devices*, vol. 58, no. 4, pp. 1229-1240, April 2011.

[102] D. Chernin et al., "Validation Studies for CHRISTINE-CC Using a Ka-Band Coupled-Cavity TWT," in *IEEE Intl. Vacuum Electronics Conference*, 2006, pp. 399-400.

[103] D. Dialetis et al., "Comparative analysis of the Curnow and Malykhin-Konnov-Komarov (MKK) circuits as representations of coupled-cavity slow-wave structures," *IEEE Transactions on Electron Devices*, vol. 52, no. 5, pp. 774-782, May 2005.

[104] S.O. Wallander, "Reflexions and Gain Ripple in TWT's," *IEEE Transactions on Electron Devices*, vol. ED-19, no. 5, pp. 655-660, 1972.

[105] H.C. Limburg, J.A. Davis, I. Tammaru, J.P. Vaszari, and J. Wilson, "Reducing the Gain and Phase Variation in High Power MMW TWTs," in *Intl. Electron Devices Meeting*, 1988, pp. 381-384.

[106] J.R.M. Vaughan, "A Model for the Klystron Cavity Gap," *IEEE Transactions on Electron Devices*, vol. 32, no. 11, pp. 2482-2484, 1985.

[107] H.G. Kosmahl and G.M. Jr. Branch, "Generalized Representation of Electric Fields in Interaction Gaps of Klystrons and Traveling-Wave Tubes," *IEEE Transactions on Electron*

Devices, vol. 20, no. 7, pp. 621-629, 1973.

[108] ATK Mission Research Corp., "Magic User's Manual," 2005.

[109] B. Goplen, L. Ludeking, D. Smith, and G. Warren, "User-configurable MAGIC for electromagnetic PIC calculations," *Computer-Physics Communications*, vol. 87, no. 1, pp. 54-86, May 1995.

[110] T.M., Jr. Antonsen, A.A. Mondelli, B. Levush, J.P. Verboncoeur, and C.K. Birdsall, "Advances in modeling and simulation of vacuum electronic devices," *Proceedings of the IEEE*, vol. 87, no. 5, pp. 804-839, May 1999.

[111] L. D. Ludeking et al., "Computational Modeling," in *Modern Microwave and Millimeter-Wave Power Electronics*. Piscataway, NJ, 2005, ch. 10, pp. 507-586.

[112] D.M. & Choi, J.J. Park, "Three-Dimensional Simulations of an X-Band Coupled-Cavity Traveling-Wave-Tube Amplifier," *Journal of the Korean Physical Society*, vol. 43, no. 6, pp. 1105-1111, December 2003.

[113] H.J. Kim, J.J. Choi, B.J. Lee, J.Y. Kim, and J.C. Lee, "MAGIC3D simulation of an ultra-compact, highly efficient, and high-power reltron tube," *IEEE Transactions on Dielectrics and Electrical Insulation*, vol. 16, no. 4, pp. 961-966, August 2009.

[114] S. G. Jeon, Y. S. Jin, J. I. Kim, G. J. Kim, and C. H. Shon, "Three-dimensional particle-in-cell simulations of 300 GHz reflex klystrons," *Journal of Applied Physics*, vol. 101, no. 5, p. 054519, March 2006.

[115] H. J. Kim, H. J. Kim, and J. J. Choi, "MAGIC3D Simulations of a 500-W Ka-Band Coupled-Cavity Traveling-Wave Tube," *IEEE Transactions on Electron Devices*, vol. 56, no. 1, pp. 149-155, January 2009.

[116] S. Reddy, V.B. Naidu, S.K. Datta, P.K. Jain, and L. Kumar, "14.5: PIC simulation of a gyrotron-traveling-wave tube amplifier," in *IEEE Intl. Vacuum Electronics Conference*, Monterey, CA, 2010, pp. 319-320.

[117] F. Friedlander, A. Karp, B.D. Gaiser, J.S. Gaiser, and B. Goplen, "Transient analysis of beam interaction with the antisymmetric mode in a truncated periodic structure using the three-dimensional computer code "SOS"," *IEEE Transactions on Electron Devices*, vol. 33, no. 11, pp. 1896-1901, November 1986.

[118] J. Petillo et al., "The MICHELLE three-dimensional electron gun and collector modeling tool: theory and design," *IEEE Transactions on Plasma Science*, vol. 30, no. 3, pp. 1238-1264, June 2002.

[119] A. Karp and G.T. Hunter, "Higher order modes and instabilities in coupled-cavity TWT's," *IEEE Trans. on Elec. Dev., vol. ED-33, no. 11*, pp. 1890-1895, 1986.

[120] I. Tammaru, "Instabilities and spurious noise in coupled-cavity traveling-wave tubes," *Physica Scripta*, vol. 71, no. 1, pp. 50-59, 1997.

[121] A. P. Kuznetsov, S. P. Kuznetsov, A. G. Rozhnev, E. V. Blokhina, and L. V. Bulgakova, "Wave Theory of a Traveling-Wave Tube Operated Near the Cutoff," *Radiophysics and Quantum*

Electronics, vol. 47, no. 5, pp. 356-373, May 2004.

[122] VP. Taranenko and A. A. Mikhin, "Study of Methods to Suppress Self-Excitation in O-type Traveling Wave Tubes (TWT)," *Radioelektronika*, vol. 17, pp. 5-17, November 1974.

[123] T. M., Jr. Antonsen, P. Safier, D. P. Chernin, and B. Levush, "Stability of traveling-wave amplifiers with reflections," *IEEE Transactions on Plasma Science*, vol. 30, no. 3, pp. 1089-1107, 2002.

[124] L. K. Ang and Y. Y. Lau, "Absolute instability in a traveling wave tube model," *Physics of Plasmas*, vol. 5, no. 12, pp. 4408-4410, July 1998.

[125] Y.D. Joo, A.K. Sinha, B.N. Basu, and G.S. Park, "Analysis of pi-point instability in an asymmetric helical slow-wave structure in helix traveling wave tubes," in *IEEE Intl. Vacuum Electronics Conference*, Monterey, CA, 2004, pp. 120-121.

[126] D. L. Webster, "The Theory of Klystron Oscillations," *Journal of Applied Physics*, vol. 10, no. 12, pp. 864-872, June 1939.

[127] L. R. Barnett et al., "Absolute instability competition and suppression in a millimeter-wave gyrotron traveling-wave tube," *Physical Review. Letters*, vol. 63, no. 10, pp. 1062-1065, September 1989.

[128] C.H. Du and P.K. Liu, "Beam-Wave Coupling Strength Analysis in a Gyrotron Traveling-Wave Amplifier," *Journal of Infrared, Millimeter and Terahertz Waves*, vol. 31, no. 6, pp. 714-723, February 2010.

[129] Y. Y. Lau, K. R. Chu, L. R. Barnett, and V. L. Granatstein, "Gyrotron travelling wave amplifier: I. Analysis of oscillations," *Intl. Journal of Infrared and Millimeter Waves*, vol. 2, no. 3, pp. 373-393, May 1981.

[130] K.R. Chu and A.T. Lin, "Gain and bandwidth of the gyro-TWT and CARM amplifiers," *IEEE Transactions on Plasma Science*, vol. 16, no. 2, pp. 90-104, April 1988.

[131] H. R. Johnson, "Backward-wave oscillators," *Proceedings of the IRE*, vol. 43, no. 6, pp. 684-697, 1955.

[132] C.R. Smith, C.M. Armstrong, and J. Duthie, "The microwave power module: a versatile RF building block for high-power transmitters," *Proceedings of the IEEE*, vol. 87, no. 5, pp. 717-737, May 1999.

[133] A.J Bahr, "A coupled-monotron analysis of band-edge oscillations in high-power traveling-wave tubes," *IEEE Transactions on Electron Devices*, vol. 12, no. 10, pp. 547-556, October 1965.

[134] G. S. Nusinovich, O. V. Sinitsyn, and T. M. Antonsen, "Excitation of parasitic waves near cutoff in forward-wave amplifiers," *Physical Review Letters E*, vol. 82, no. 4, p. 046404, October 2010.

[135] P.J. Crepeau and P.R. McIsaac, "Consequences of symmetry in periodic structures," *Proceedings of the IEEE*, vol. 52, no. 1, pp. 33-43, January 1964.

[136] B. Levush et al., "Relativistic backward wave oscillators: Theory and experiment," in *IEDM Intl. Electron Devices Meeting*, 1991, pp. 775-778.

[137] S. Y. Park, V. L. Granatstein, and R. K. Parker, "A Linear Theory and Design Study for a Gyrotron Backward-Wave Oscillator," *Intl. Journal of Electronics*, vol. 57, no. 6, pp. 1109-1123, December 1984.

[138] E.L. Lien, "Stopbands Produced by Asymmetrical Support Rod System in Helix Structures," *Intl. Electron Devices Meeting*, vol. 25, pp. 412-415, 1979.

[139] A. Karp, "Biperiodicity as Liability and as Asset in Non-Helix Linear-Beam TWT Interaction Structures," *Intl. Electron Devices Meeting*, vol. 29, pp. 440-443, 1983.

[140] Young-Min Shin et al., "Numerical modeling analysis of 0.22 THz sheet beam TWT circuit," in *IEEE Intl. Vacuum Electronics Conference*, Bangalore, IND, 2011, pp. 139-140.

[141] J. Pasour, K. Nguyen, E. Wright, and B. Levush, "3.5: Sheet beam EIK sensitivity to multimoding and circuit imperfections," in *IEEE Intl. Vacuum Electronics Conference*, Monterey, CA, 2010, pp. 45-46.

[142] J.R. Frey and I. Tammaru, "A coupled-cavity TWT operating in the inverted slot mode," *Intl. Electron Devices Meeting*, vol. 27, pp. 504- 506, 1981.

[143] G.M., Jr. Branch, "Electron beam coupling in interaction gaps of cylindrical symmetry," *IRE Transactions on Electron Devices*, vol. 8, no. 3, pp. 193-207, May 1961.

[144] R. E. Collin, *Foundations for microwave engineering*, 2nd ed. New York: IEEE Press, 2001.

[145] G. M. Branch and T. G. Mihran, "Plasma Frequency Reduction Factors in Electron Beams," *IRE Transactions*, vol. ED-2, pp. 3-11, 1955.

[146] S. Ramo, "Space-Charge and Field Waves in an Electron Beam," *Phys. Rev.*, vol. 56, no. 3, pp. 276-283, August 1939.

[147] R. M. Bevensee, *Electromagnetic Slow Wave Systems*. New York: Wiley, 1964.

[148] A. Hessel, Ming Hui Chen, R.C.M. Li, and A.A. Oliner, "Propagation in periodically loaded waveguides with higher symmetries," *Proceedings of the IEEE*, vol. 61, no. 2, pp. 183-195, February 1973.

[149] J.E. Atkinson et al., "8.3: A high aspect ratio, high current density sheet beam electron gun," in *IEEE Intl. Vacuum Electronics Conference*, Monterey, CA, 2010, pp. 97-98.

[150] S. Humphries, *Charged Particle Beams.*: John Wiley and Sons, 1990.

[151] T.M., Jr. Antonsen, Note on Linear Theory of Slow Wave Interactions with Planar Beams, 2005.